Chair of Applied Geophysics

Master's Thesis

Optimisation of the induced polarisation method (IP effect) for applications in landfill mining

Valentina Leonie Strasser, BSc

September 2022

MONTANUNIVERSITÄT LEOBEN
www.unileoben.ac.at

EIDESSTATTLICHE ERKLÄRUNG

Ich erkläre an Eides statt, dass ich diese Arbeit selbständig verfasst, andere als die angegebenen Quellen und Hilfsmittel nicht benutzt, und mich auch sonst keiner unerlaubten Hilfsmittel bedient habe.

Ich erkläre, dass ich die Richtlinien des Senats der Montanuniversität Leoben zu "Gute wissenschaftliche Praxis" gelesen, verstanden und befolgt habe.

Weiters erkläre ich, dass die elektronische und gedruckte Version der eingereichten wissenschaftlichen Abschlussarbeit formal und inhaltlich identisch sind.

Datum 18.09.2022

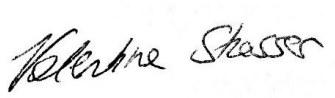

Unterschrift Verfasser/in
Valentina Leonie Strasser

Kurzfassung (deutsches Abstract)

Der Grundgedanke dieser Arbeit ist das Auffinden von metallischen Objekten in Deponien, die sich für Recylingprozesse lohnen würden. Durch die nicht invasive Messmethodik der Geoelektrik können große Bereiche von der Oberfläche aus untersucht und dadurch gezielt einzelne Bereiche lokalisiert werden, die einen ausreichenden Metallgehalt aufweisen sollen. Dadurch kann auf großflächige Probegrabungen im Deponiebereich verzichtet werden, da die geeigneten Gebiete bereits vorher lokal eingegrenzt werden können.

Einleitend finden sich die theoretischen Hintergründe von Geoelektrischen Messungen, mit besonderem Fokus auf der Methodik der induzierten Polarisation. Die klassische elektrische Widerstandstomographie wurde parallel für jede durchgeführte Messungen mit aufgenommen und wird zur Interpretation der IP-Ergebnisse herangezogen. Abgesehen davon werden diese Daten nicht weiter behandelt, da der Fokus klar auf den Ergebnissen der induzierten Polarisation liegt. Anschließend werden Literaturbeispiele sowie die Eckpunkte des Interreg North-West Europe RAWFILL Projekt kurz aufgezeigt. Der Hauptteil der Arbeit beschäftigt sich mit den durchgeführten Feldmessungen. Als Messort wurde die Deponie in Allerheiligen im Mürztal ausgewählt, auf der mechanisch-biologischer Restmüll, sogenanntes MBA Material, deponiert wird. Die Messungen wurden bewusst im ältesten Teil der Deponie durchgeführt, wo seit 1996 keine neuen Abfälle mehr deponiert worden sind. Vorausgegangene Untersuchungen zeigten jedoch einen relativ geringen Metallgehalt im Deponiebereich, wodurch ein metallischer Gasdom als Messziel herangezogen worden ist. Dieser steht stellvertretend für größere metallische Objekte im Deponieuntergrund. Es wurden im Mai 2021 und im November 2021 zwei getrennte Messdurchläufe an zwei unterschiedlichen Gasdomen durchgeführt. Dadurch soll ein breiteres Bild über den Einfluss des Deponiekörpers auf die Messung erhalten werden, da Aspekte wie Bodenfeuchte oder Zusammensetzung des deponierten Mülls nicht zu vernachlässigende Auswirkungen auf die IP-Daten entlang der gezogenen Profillinien haben können. Zusätzlich wurde mit zwei unterschiedlichen Messgeräten sowohl im Zeitdomain als auch im Frequenzdomain gemessen. Weiters wurde mit Wenner und Dipol-Dipol Konfigurationen sowie mit klassischen Stahlelektroden und nicht polarisierbaren Elektroden gemessen, um sämtliche Aspekte der Einflussnahme bestimmter Faktoren auf die Messergebnisse zu untersuchen. Der Großteil der Arbeit befasst sich mit der Auswertung der 100 durchgeführten Feldmessungen, die einen quantitativen Abschnitt über die statistischen Auswertungen der Rohdaten umfasst sowie einem stärker qualitativen geprägten Teil, der sich mit der Interpretation der Strukturen in den erzeugten Inversionsmodellen beschäftigt. Zusätzlich dazu wird Stellungnahme zum abgebrochenen Laborversuch bezogen. Abschließend erfolgt eine Interpretation

der Messungen und eine Darstellung der erhaltenen Informationen sowie die Limitationen dieser Messmethodik und einen Ausblick hinsichtlich Verbesserungsvorschläge für zukünftige Messversuche.

Bei der Auswertung der Phasenwinkel, die als maßgeblicher Indikator für den IP-Effekt herangezogen worden sind, zeigt sich eine beständige Verteilung zwischen durchschnittlich 10 bis 50mrad für alle Messungen, die mit dem *Lippmann 4 point light 10W* im Frequenzbereich durchgeführt worden sind. Jene Messungen mit Wenner Konfiguration weisen eine konstantere Werteverteilung und eine geringere Streuung verglichen mit Messungen mit Dipol-Dipol Konfiguration auf. Die ebenfalls analysierten *dU90* Werte ermöglichen Rückschlüsse auf die allgemeine Messqualität und ergeben im Vergleich der beiden Messkonfigurationen ebenfalls günstigere Werte für die Wenner Konfiguration. Im Gegensatz dazu wurde für die Messungen im Zeitbereich, die mit dem *Mangusta System 24/144E* gemessen worden sind, keine statistischen Analysen durchgeführt, da die Rohdaten eine geringe Dichte an Messinformationen enthalten. Allerdings mussten die Rohdaten im Zuge der Inversionsauswertung modifiziert werden, da sich im ersten Durchlauf sehr hohe Iterationsfehler zeigten. Daher wurden sämtliche Chargeability Werte über 100ms gelöscht, da diese als Fehlmessungen angesehen werden und dadurch konnte der Iterationsfehler in einen annehmbaren Bereich verschoben werden.
Verglichen mit den Auswertungen aus Literaturbeispielen zeigen sich Übereinstimmungen in den Daten. Daher ist deren Verteilung als valide und zutreffend für Deponien mit einem ähnlichen Aufbau wie der in Allerheiligen im Mürztal einzustufen.
Durch die differenzierte Betrachtung der Messungen hinsichtlich der verwendeten Messeinstellungen und Elektrodentypen kann anhand der Ergebnisse eine Empfehlung für IP-Messungen unter Verwendung der Wenner Konfiguration und der nicht polarisierbaren Elektroden für Messungen mit ähnlichen Umgebungsparametern ausgesprochen werden.

Abstract (Englisch)

The basic idea behind this work is to find metallic objects in landfills that would be worthwhile for possible recycling processes. Using the non-invasive measurement methodology of geoelectric, large areas can be investigated from the surface and thus targeted individual areas can be located that are supposed to have a sufficiently high metal content. This means that large-scale test excavations in the landfill area can be dispensed with, as the areas of interest can already be locally delimited beforehand. In the introduction, the theoretical background of geoelectrical measurements is given, with a special focus on the methodology of induced polarisation. Classical electrical resistivity tomography was included in parallel for each measurement carried out and is used to interpret the IP results. Apart from that, this data will not be discussed further as the focus is clearly on the induced polarisation results. Afterwards, literature examples and the key points of the Interreg North-West Europe RAWFILL project are briefly presented.

The main part of the paper deals with the field measurements carried out. The landfill in Allerheiligen in the Mürz valley, where mechanical-biological residual waste, so-called MBT material, is deposited, was chosen as the measurement site. The measurements were deliberately taken in the oldest part of the landfill, where since 1996 no new waste has been deposited. However, previous investigations showed a relatively low metal content in the landfill area, which is why a metallic gas dome was used as a measurement target. This is representative of larger metallic objects in the landfill subsoil. Two separate measurement runs were carried out on two different gas domes in May 2021 and November 2021. This should provide a broader picture of the influence of the landfill body on the measurement, as aspects such as soil moisture or the composition of the landfilled waste can have non-negligible effects on the IP data along the profile lines drawn. In addition, two different measuring devices were used to measure in the time-domain as well as in the frequency-domain. Furthermore, measurements were made with Wenner and Dipole-Dipole configurations as well as with classical steel electrodes and non-polarisable electrodes in order to investigate all aspects of the influence of certain factors on the measurement results. The main part of the thesis deals with the evaluation of the 100 field measurements carried out, which includes a quantitative part dealing with the statistical evaluation of the raw data and a more qualitative part dealing with the interpretation of the structures in the inversion models generated. In addition, comments are made on the aborted laboratory test.

Finally, an interpretation of the measurements and a presentation of the information obtained as well as the limitations of this measurement methodology and an outlook with regard to suggestions for improvement for future measurement experiments are given.

The evaluation of the phase angles, which have been used as a significant indicator for the IP effect, shows a consistent distribution between 10 and 50mrad on average for all measurements performed with the *Lippmann 4 point light 10W* in the frequency-domain. Those measurements with Wenner configuration show a more constant value distribution and a lower scatter compared to measurements with dipole-dipole configuration. The dU90 values, which were also analysed, allow conclusions to be drawn about the general measurement quality and also yield more favourable values for the Wenner configuration in a comparison of the two measurement configurations. In contrast, no statistical analyses were performed for the measurements in the time-domain that were measured with the *Mangusta System 24/144E*, since the raw data contain a low density of measurement information. However, the raw data had to be modified in the course of the inversion analysis because very high iteration errors were revealed in the first run. Therefore, all chargeability values above 100ms were deleted, as these are considered to be erroneous measurements, and thus the iteration error could be shifted into an acceptable range.

Compared with the evaluations from literature examples, there are similarities in the data. Therefore, their distribution can be classified as valid and applicable for landfills with a similar structure as the one in Allerheiligen in the Mürz valley.

By differentiating the measurements with respect to the measurement settings and electrode types used, the results can be used to make a recommendation for IP measurements using the Wenner configuration and the non-polarisable electrodes for measurements with similar environmental parameters.

Danksagung

An dieser Stelle möchte ich mich für jede Unterstützung, die mich bis zu diesen Punkt in meinem Studium gebracht hat, bedanken.

In erster Linie gebührt mein Dank meinem Betreuer Herrn Professor Robert Scholger, der mich während meiner Feldmessungen sowie diversen Zwischenabschnitten des Auswertungsprozesses bis zur fertigen Arbeit betreut, begleitet und schlussendlich auch beurteilt hat.

Des Weiteren möchte ich auch Herrn DI Helmut Neumann von der Firma geo engineering GmbH meinen Dank für die Bereitstellung des zusätzlichen Messgerätes aussprechen.

Bei meinen Eltern bedanke ich mich für die Möglichkeit, ein Studium an der Montanuniversität absolvieren zu dürfen und für die Unterstützung in jeglicher Phase des Studiums.

Table of Content

1. Introduction

The aim of this work is the detection of metal in landfill bodies using the induced polarisation method and to validate the use of induced polarisation for landfill mining on the example of the landfill in Allerheiligen in the Mürz valley.

Two different measuring devices were used to cover both the frequency-domain and the time-domain. The landfill site Allerheiligen in the Mürz valley was chosen as the study area. In addition, laboratory measurements were carried out in which an artificial landfill subsoil was simulated in a tank and the measurements could be carried out on a smaller scale with a known subsoil structure and water saturation. The measuring instruments used were the *4 point light 10W* from *Lippmann* for the frequency-domain and *the Mangusta System MC 24/144E* from *Ambrogeo Instruments* for the time-domain.

The thesis is divided into three main parts, starting with a theory input to convey the basic principles. The theory part, for its part, is divided into a physical/electrotechnical part and the following literature examples, which qualify the use of this method for landfill mining accordingly and provide comparative results. This is followed by a presentation of the field work measurements and the laboratory measurements. In this context, the measuring instruments used and their mode of operation are also described in more detail. In total, 100 measurements were carried out in different frequencies as well as some repeat measurements. The use of two different measuring devices enables a more comprehensive recording of a wide range of measured values due to the different measuring methods.

The final part includes the evaluation, presentation and interpretation of the measurement results, which are compared with the literature examples mentioned initially to support their significance. The measurement results were first analysed statistically and cross plots were created for the graphical representation in order to be able to recognise trends between individual measurement values. Subsequently, the individual measurements were compared with each other, whereby special attention was paid to the comparison of the time-domain and frequency-domain measurements.

2. Basic Principles / Theory input

An input of the theoretical background is given to enable an equal comprehension of the covered topic as well as to ease the traceability of the evaluation and result interpretation. For this purpose, a general explanation of the method of induced polarisation is given as well as information from some practical examples and studies to bring together this knowledge with the settings of field measurements and the laboratory experiments.

As claimed by Revil et al. (2012) geoelectrical survey methods such as resistivity tomography and induced polarisation enable the identification of the spatial distribution of capacity and low-frequency resistivity of the soil.

2.1. Geoelectrical Methods and historical development

2.1.1. Coulomb's Law

All geoelectrical measurement methods are based on the electrical charge and the behaviour of all the associated properties (Lowrie, 2007). According to Everett (2014), these techniques are on the upgrade since the 1990s. However, the theoretical background has its origin way back in the eighteenth century as electricity was first defined as a flow between bodies which are electrically charged. If a certain distance between those bodies is undershot or they are brought in contact on another way, an electrical flow manifests itself in between which is termed as electrical current (Lowrie, 2007).

An important coherence for understanding electrical forces is described with Coulomb's Law:

(1)

$$F = K\frac{Q_1 Q_2}{r^2} \quad \rightarrow \quad F = \frac{1}{4\pi\varepsilon_0} \times \frac{Q_1 Q_2}{r^2}$$

Q_1: electric charge [As]
Q_2: electric charge [As]
r: the distance between Q_1 and Q_2 [m]
K: Coulomb constant [Vm/As]
ε_0: permittivity constant, ~$8{,}854187 * 10^{-12}$ [$C^2N^{-1}m^{-2}$]

Q_1 and Q_2 are two electric charges which are separated by the distance *r* and multiplied with the Coulomb constant *K*. This formular explains the force of attraction or repulsion between the two electric charges Q_1 and Q_2. On the right-hand side Coloumb's law is written with the SI unit for *K*. (Lowrie, 2007).

In 1897 Joseph J. Thomson first described the electron as the fundamental unit for electric charge which is clearly recognizable in metals, where some of the electrons are only in weak bondings with the atoms. Due to this fact, these electrons are easily transposed through the material. Such a behaviour classifies metals as conductors because they enable an electric current. As opposed to this, materials which show strong bonds between the electrons and the atoms are called insulators because they are strongly reducing the current flow, in some cases even hindering the movement of the electrons completely (Lowrie 2007).

Another important parameter is the electric field *E* of the charge *Q*. It is described as the force that one electric charge applies onto another one. Taking *Equation (1)* and setting Q_1=*Q* and assume that Q_2 is 1, then the following relationship, shown as *Equation (2)*, for the electrical field can be obtained (Lowrie, 2007):

(2)

$$E = \frac{Q}{4\pi\varepsilon_0 r^2}$$

E: electrical field [NC^{-1}]

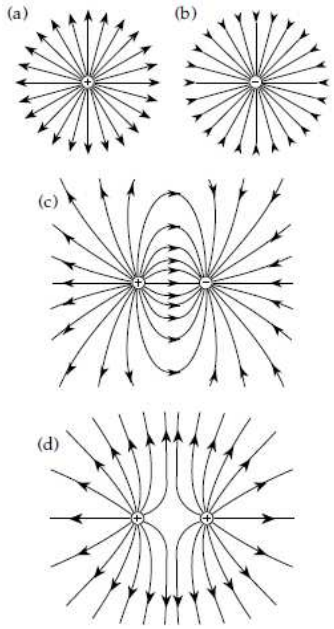

Figure 1: Showing different planar cross-sections with schematic electric field lines around positive and negative point charges. (a) singular positive charge (b) singular negative charge (c) a positive and negative charges (d) two similar positive charges (Lowrie 2007).

Michael Faraday established a more graphical representation of the expression field. *Figure 1* shows how the electrical lines behave in the nearfield of an electrical charge. Generally, the field lines show concentric geometry if only one charge is present, but in an opposite direction. If two contrary charged sources are next to each other the electric lines diverge from the positive one, extend and converge on the negative one which looks like the point sources are pulled closer together. In contract when two equally charged sources are close together the field lines diverge in the space in-between which seems like thrusting them apart. The tangent in any point of the electric lines implies the direction of the electric field and its strength is represented by the spatial concentration of the lines, which is stronger in the vicinity of the charges and weaker with increasing distance. Therefore, changing the position of charges in the electrical field requires a certain amount of work which is also added to the potential energy of the whole system. *Equation (3)* shows the shifting of a distance *dr* against the electric field *E* and the resulting alteration of the potential *dU* (Lowrie 2007).

(3)

$$E = -\frac{dU}{dr} \quad \rightarrow \quad U = -\int_{\infty}^{r} E dr = -\int_{\infty}^{r} \frac{Q}{4\pi\varepsilon_0 r^2} dr \quad \rightarrow \quad U = \frac{Q}{4\pi\varepsilon_0 r}$$

U: electrical potential at r [J/C]
Q: potential difference [J/C]

Through integration the final formular rightmost is obtained where *Q* as a very important parameter describes the potential difference between two points and also specifies a volt. *Equation (3)* also gives an alternative unit for the electrical field which is Vm^{-1}. The electric current travels from higher potential to an area of lower potential and is therefore contingent on the potential difference *U* (Lowrie, 2007).

2.1.2. Ohm's Law

Georg Simon Ohm first described the correlation between the electric current in a conductive environment and the voltage of the needed electrical source, like a batterie. (Lowrie, 2007). The Ohm's law is fundamental for understanding electrical measurements and thus it is also absolutely necessary for geoelectrical methods:

(4)

$$I = \frac{U}{R} \quad \rightarrow \quad U = R \times I \quad \rightarrow \quad R = \frac{U}{I} \quad \rightarrow \quad [R] = \frac{V}{A} = \Omega \text{ (Ohm)}$$

I: current [A]
U: potential [V]
R: resistance [Ω]

Equation (4) connotes that the higher the potential *V* and the lower the resistance *R*, the greater the current *I* will be. The Ohm's Law in its classical form depicts the situation of conductors with a linear current-voltage characteristic whereby current and potential are direct proportional towards each other and imply a linear function between the current *I* and the potential *U*. Such conductors are called linear resistors. Metal conductors under constant temperature conditions are numbered among these. The conversion of the Ohm's law constitutes that a weak resistor enables a better flow of the current. Therefor the reciprocal of the resistance is also an important parameter and is called the conductance *G* (Lowrie, 2007):

(5)

$$G = \frac{1}{R} \quad \rightarrow \quad [G] = \frac{1}{\Omega} = S \ (Siemens)$$

G: conductance [1/Ω]

Plugged into the Ohm's Law from *Equation (4)* it results in the following *Equation (6)*:

(6)

$$I = G \times U$$

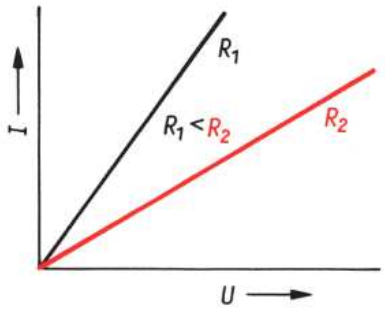

Figure 2: Current-voltage characteristics of two linear resistors (Zeitler, Simon, 2016).

The conductance *G* is described by the slope of the current-voltage characteristic which runs steeper, the larger the conductance, i.e., the smaller the resistance and is depictured in *Figure 2* (Zeitler, Simon, 2016).

Table 1 summarized Lowries explanations about the different behaviour of resistance according to the length and the thickness of the conductor e.g., a cable.

Table 1: Summary of the resistance behaviour to the shape of the conductor.

conductor shape:	**long**	**short**	**thin**	**thick**
resistance [Ω]	higher	lower	higher	lower

Equation (7) can be derived from these correlations:

(7)

$$R = \rho \frac{L}{A}$$

L: length of the conductor
A: cross-sectional area of the conductor
ρ: proportionality constant

The resistivity of the conductor is described by the proportionality constant ρ, it is a physical property for a certain material that hinders the flow of charge. The unit of the resistivity ρ is ohm-meter [Ωm]. The reciprocal value of the resistivity is called conductivity σ with the unit [$\Omega^{-1}m^{-1}$] (Lowrie, 2007).

Equation (7) can be substituted for *R* in *Equation (4)* and after rearranging the following *Equation (8)* is obtained:

(8)

$$\frac{V}{L} = \rho \frac{I}{A}$$

V/L: electric field E to be constant over a length of the conductor
I/A: current per unit cross-sectional area of the conductor, can also be written as J

V/L is the electric field *E* assumed that the potential gradient is constant over the length of the conductor. The term on the right side of *Equation (8)*, which is *I/A*, is the current density and can be denoted with the symbol *J*. Perusing through all the mentioned steps the Ohm's law can now be rewritten in the following form which is the basis for further calculating the needed equations that are fundamental in resistivity methods. (Lowrie, 2007)

(9)

$$E = \rho J$$

J: current density

2.1.3. Electrode arrays

Everett (2014) takes these obtained formulars to explain the behaviour of the current in the case of a geoelectrical survey. The theoretical model is a spherical whole-space of a consistent resistivity *ρ* with one electrode for inserting current set at the origin and a second one in an infinite distance, *Figure 3*.

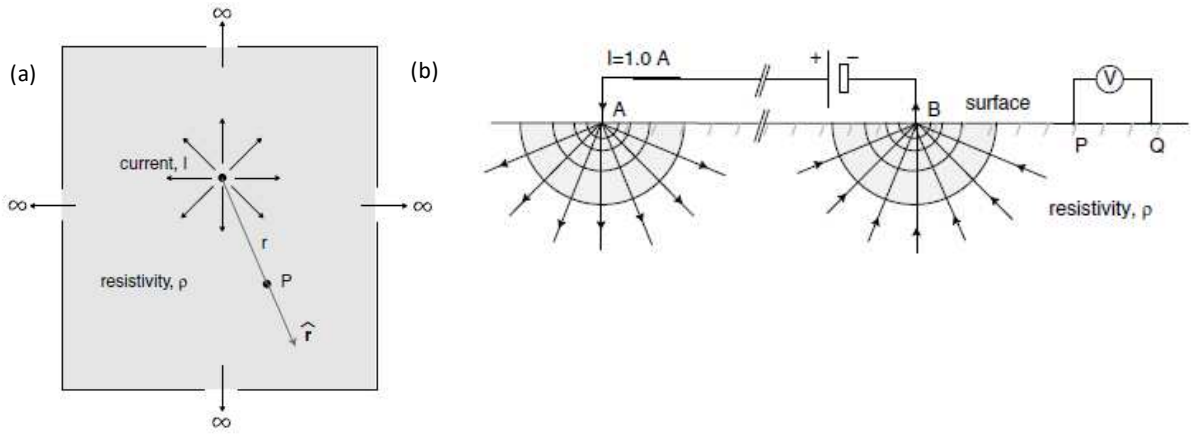

Figure 3: (a) graphical illustration of voltage: a point charge is transferred by the electric field from infinity to the marked point P. Also, the current I is injected into the spherical whole-space with homogenous resistivity. (b) Sketch of a point injection of electric current into the simplified model of a homogenous halfspace at point A, with a point sink B and the voltage measurement between the two points P and Q (Everett, 2014).

Figure 3 (a) shows an arial perspective onto the uniform halfspace with the same resistivity in each point. In addition, the voltage is depictured as the movement from a point source to a certain point *P* by the electrical field. In *Figure 3 (b)* a schematic array of a simple resistivity measurement is shown.

The electric current *I* is inserted at point *A*, with a point sink in *B* and spreads spherically with the radius *r* in the conductive subsurface as well as onto a radial surface area of $2\pi r^2$ but not in the air which can be seen as an insulator. A voltage measurement is proceeds between the two pints *P* and *Q* (Everett, 2014).

A very important parameter for resistiviy measurements is the apparent resistivity ρ_a (Everett, 2014):

(10)

$$\rho_a = \frac{2\pi V_{PQ}}{I}\left[\frac{1}{r_P} - \frac{1}{r_Q}\right]^{-1} = \kappa Z$$

ρ_a: apparent resistivity
V_{PQ}: voltage measured between point P and Q
Z: earth's impedance
κ: geometric factor

Equation (10) shows the apparent resistivity as the result of the multiplication of the earth impedance *Z* and the geometric factor *κ* which depends on the used configuration of the electrodes. The apparent resistivity is seen as the resistivity which would have been obtained in an uniform subsurface. In *Figure 4* the most commonly used electrode configurations are displayed, as well as the associated geometry factors in *Table 2* (Everett, 2014):

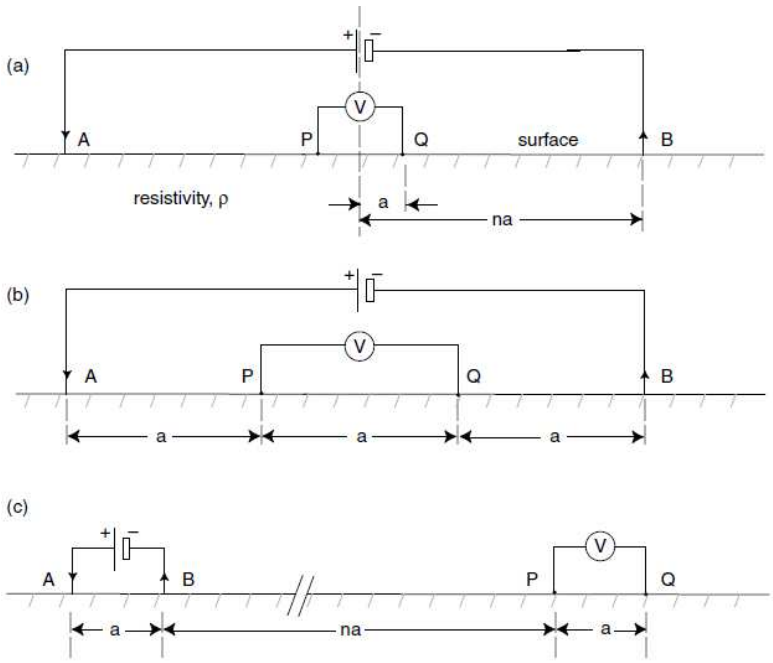

Figure 4: Sketches of the most common traditional four-point configurations: (a) Schlumberger (b) Wenner (c) Dipole-Dipole (Everett, 2014).

Table 2: Associated geometry factors to the listed electrode configurations in Figure 4 (Everett, 2014).

electrode configuration	(a) Schlumberger	(b) Wenner	(c) Dipole - Dipole
geometry factor κ	$\kappa = (n-1)\,(n+1)\,\pi a/2$	$\kappa = 2\pi a$	$\kappa = \pi n\,(n+1)\,(n+2)\,a$

The variable *a* describes the distance between two electrodes and *na* is just a multiple of *a*, which is as well as *a* depending on the real measurement settings.

According to Loke (2000) the resistivity methods find their origin back in the 1920s in research works of the Schlumberger brothers.

Back in those days the four-point-arrays were widely used until they were replaced by modern arrays with up to 100 and more electrodes which are automatically switched on the appropriate electrodes for achieving the right electrode configuration over the whole profile length. The Schlumberger configuration shows its strength in sounding where the resistivity on a depth profile is measured underneath one certain position. In contrast, the Wenner arrangement provides the best result in lateral measurements with a stable penetration depth. The Dipole-Dipole array incorporates the advantages of both, the Schlumberger and the Wenner configuration but with a decrease of the signal-to-noise ratio at large distances between the current electrode pair *A* and *B* and the potential electrode pair *Q* and *P* (Everett, 2014).

3. Induced polarisation

Based on the general theoretical fundamentals of geoelectric measurements depicted in *Chapter 2* the induced polarisation is connected to the phenomenon of chargeability of certain materials in the subsurface (Everett, 2014). The importance and use of induced polarisations methods is on the upswing owing to advances in the equipment and software. This development enables a faster and cheaper use especially when it comes to environmental issues (Carlson et al., 2001). The induced polarisation can mostly be measured with standard resistivity equipment as claimed by Reynolds (2011) which simultaneously provides additional information to the standard resistivity survey.

3.1. Historical background

This method finds its origin back in the early 20th century and was first described by Conrad Schlumberger. The name emerges from the translation of Schlumberger's work but was often discussed due to its possibly misleading sense. Vice the suggestion of some geophysicist adding the term "electrical" to create a clear differentiation towards magnetic polarisation effects, the original denotation naturalised itself (Sumner, 1976). According to Reynolds (2011) another obsolete long-term designation for this effect is the overvoltage effect. The first upsurge was in 1942 due to an USA Navy programme using this method to ferret out mines in the ocean.

In the 1960s the discipline of induced polarisation exploration experienced another rise, especially in the USA several universities started doing researches in the field of metallic mineral mining by using this method which increased the awareness and importance and lead to the result that this method became the third important exploration technique in geophysics (Sumner, 1976).

Nowadays the induced polarisation method is also used in environmental problems mostly for the detection of groundwater contamination as well as the monitoring of landfills (Aristodemou and Thomas-Betts, 1999).

3.2. Theoretical background

The method of induced polarisation is based on the so-called IP effect which is a phenomenon created by an induced current and the resulting reaction concerning the electron transfer which proceeds between the metallic minerals and the electrolyte irons from nearby filled pore spaces. The transmission electrical current creates an over-potential in the electrochemistry of the pore fill right at its interface with the electron-conducting mineral (Sumner, 1976).

The leading fundamental motors which drive the induced polarisation effect are the grain (electrode) polarisation (overvoltage) and the membrane (electrolytic) polarisation both based on electrochemical

properties and processes in the subsurface. Down to the present day there are still principles of this method not fully understood and investigated (Reynolds, 2011).

3.2.1. Grain (electrode) polarisation

The effect of grain or electrode polarisation is driven by the similar process that consequences in self-potentials. This kind of polarisation can occur when metallic electrodes are used. Basically, when a metal object, such as the used electrode, is positioned into an ionic solution the present charges are splitting according to their dissimilar polarities even if no voltage is actively put onto this object. This ionic balance is destroyed at the moment an external voltage is put on because this leads to an electric current which shifts the potential contrast between the ionic solution and the metal electrode. Eliminating the applied voltage again results in a recovery of the ionic balance (Reynolds, 2011).

In real measurement environment the applied electric current is conducted by pore channels and microcracks transporting fluids like groundwater and the containing soluble minerals as ions through rocks (Reynolds, 2011).

According to Lowrie (2007) this overall effect is very similar to the one that takes place in the vicinity of ore minerals wherefore this method is amongst others especially used in detecting ore bodies.

If such an ore grain, which has a certain conductivity, hinders a possible flow channel, charges arrange and then a polarisation of the concerning grain happens and a potential difference is resulting and will be again decreasing to zero as soon as the exerted voltage is turned off. Simultaneously a back diffusion of the ions in the fluid medium occurs, *Figure 5*. Additional to the polarisation of the conductive grain, further large ore areas will also form a net polarisation (Reynolds, 2011).

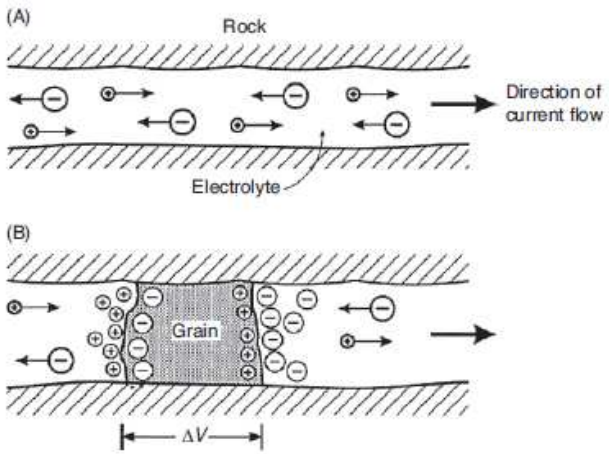

Figure 5: Showing a schematic visualization of the grain (electrode) polarisation where (a) shows an open pore channel enabling the unconditional electrolytic flow and (b) a blocked pore channel and the resulting polarisation of the conductive grain (Reynolds, 2011).

Measuring this time limited specific overvoltage decline can be done in the time-domain system (Reynolds, 2011).

The size of the orebody and the overall metallic concentration are responsible for the magnitude of this effect (Lowrie, 2007). But according to Reynolds, this phenomenon can mostly be beheld as a surface occurrence especially in areas with highly spread ore bodies results in strong IP responses due

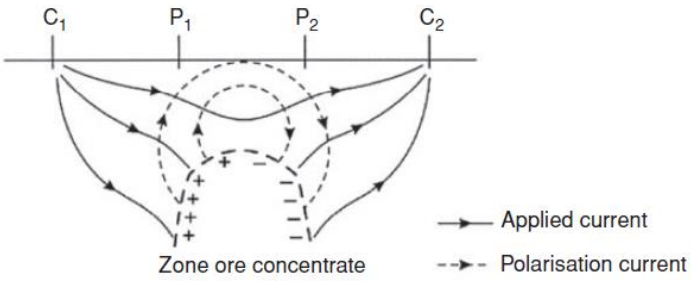

Figure 6: Showing the macroscopic effect of grain polarisation over a spread ore body with a Wenner configuration. The polarisation current appears on top of the ore zone (Reynolds, 2011).

to the larger total surface area. The IP effect can sometimes seem a bit mis shifted to the original location of the ore body, *Figure 6*. Such big ore bodies are taking on a net polarisation which leads to the macroscopic net polarisation current flow in the subsurface. This can then be monitored as the IP return. *Figure 6* shows the procedure for a Wenner configuration: the induced current starts to polarise the ore body in the underground that creates a temporary polarisation current measurable with the used equipment as soon as the current is switched off. According to Reynolds (2011), the current field would be even more complex in a Dipole-Dipole configuration. The degree of reconstruction of the ionic balance is depending onto several factors like the general rock structure and the geometry of the pores as well as the permeability, the overall ionic concentration as well as the electronic conductivity (Reynolds, 2011).

3.2.2. Membrane (electrolytic) polarisation

As claimed by Ulrich and Slater (2004) and Scott (2006) the membrane (electrolytic) polarisation has two main drivers: narrowing parts of pore channels as well as the existence of clayey minerals inside the pore channels like in shaly sandstones. Generally, most rock minerals show a negative charge at the interface between the pore fluids and the minerals itself. As opposed to this, the positively charged ions inside the pore fluid are accumulating as a layer of around 100µm directly on the surface of the rock which leads to a rejection of the negative charges, *Figure 7 (a)*. If the general size of the pore channel is diminished so much that it is undercutting the mightiness of the positively charged layer then the further ion flow will be hindered as soon as voltage is induced. A potential difference is built up as the cluster of positive ions is increasing and the negative charges are repelled and leaving. The ionic balance is restored as soon as the induced voltage is turned to zero. This process is driven by diffusion and creates the measurable IP results (Reynold, 2011).

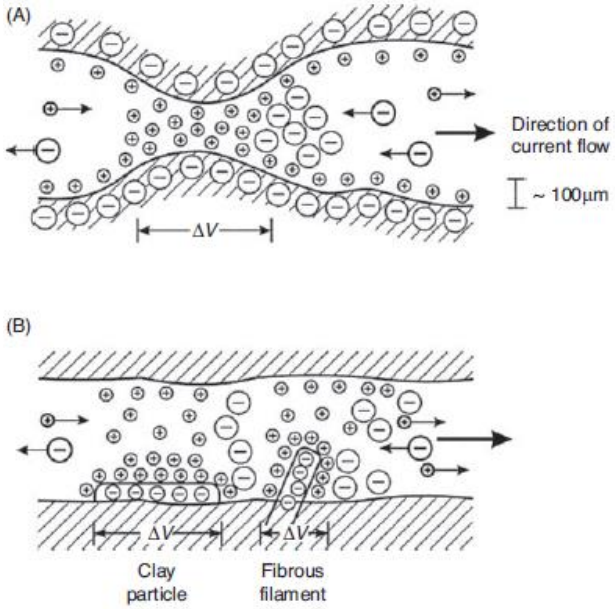

Figure 7: Schematic depiction of the two main drivers of the membrane (electrolytic) polarisation: (a) bottleneck situation inside a pore channel in between rock grains (b) the accumulation of positive charges around negatively charged flat clay minerals and the blockage of negative ions (Reynolds, 2011).

The other reason for this special kind of polarisation is the existence of clay minerals inside the pore channels due to the fact that they are often negatively charged. Again, the positive charges are highly forced to attach onto these particles creating an overall larger positively charged object inside the channel.

If current is induced, the positive ions are able to change position between these accumulations of positive charges and the negative ones are again hindered to flow, *Figure 7 (b)*. This also creates a contrast in the overall concentration of the ions. Once the induced current is switched off, this imbalance of charged ions is again normalized equally caused by diffusion processes and generating the IP response (Reynolds, 2011).

3.2.3. Time-domain measurements

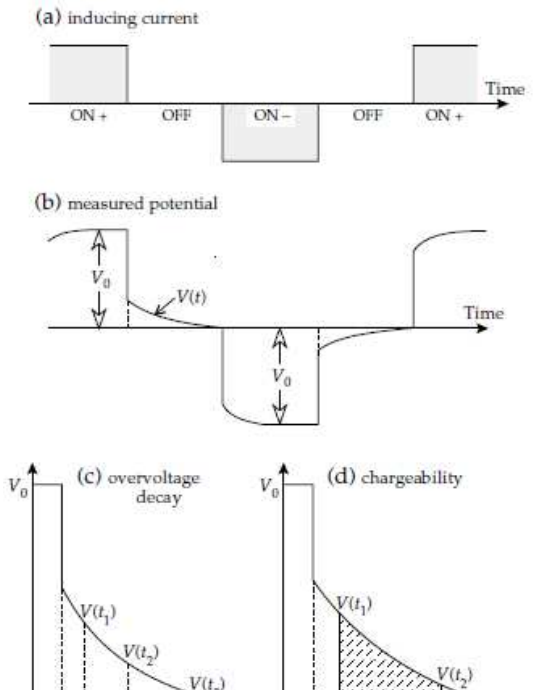

Figure 8: (a) schematic display of the on- and off-sequences of the induced electric current during an IP measurement (b) resulting behaviour of the measured potential (c) zoom-in section to show the overvoltage decay for an off-sequence (d) zoom-in section of the chargeability between t_1 and t_2 (Lowrie, 2007).

Characterising for the induced polarisation are the on- and off- sequences of the induced electric current creating a box-shaped diagram, *Figure 8 (a)*. The sequence below is directly connected to the upper image and depicts the reaction of the potential to the changing electric current. First, the potential decreases after the current is turned off, but it does not drop to zero immediately but after a certain timespan. This decrease is notated as the function *V(t)* according to the time that is needed to reach zero potential. The same procedure is observed when the electric current is turned on again. Admittedly, the potential reaches a certain threshold close to the maximum value first but then needs a certain time to finally reach V_0 again, which is named the steady-state value. Overall, the process behaves similar but rather switched.

In *Figure 8 (c)* the overvoltage decay over time, as a zoom-in from *Figure 8 (b)* is shown. The chargeability between two moments t_1 and t_2 is depictured in *Figure 8 (d)* (Lowrie, 2007). According to Reynolds (2011) the measurement of the observed voltage at the exact time when the currents turned off is very complicated. Therefore, it is monitored after the swich off at a certain timespan, normally after 0.5 seconds. Then, the further measurements are characterized by short acquisition times of around 0.1 seconds every 0.5 seconds. The acquired results are then integrated to obtain the zone under the decay curve. Dividing the integral by V_0 as a maximum value, results in the apparent chargeability given in milliseconds (Reynolds, 2011).

The chargeability and the apparent resistivity can be denoted by the *Equations (11)* and *(12)*:

(11)

$$M = \frac{V_P}{V_0} \left[\frac{mV}{V} \; or \; \%\right]$$

(12)

$$M_a = \frac{1}{V_0} \int_{t_1}^{t_2} V_P(t)dt = \frac{A}{V_0}$$

V_P: overvoltage
V_0: observed voltage with induced current
$V_P(t)$: overvoltage at time t
A: area below the overvoltage curve

This whole process of integration and division is done to improve the signal to noise ratio as the noise from coupling processes of cable and from possible background potentials is minimized. As opposed to this, measuring the true chargeability in real fieldwork is nearly unachievable due to the fact that real ground conditions are identified by heterogeneity which results in changing chargeability as well as true resistivity responses in each layer. Hence, the obtained measured information is a complex function including each absolute chargeability and true resistivity of the whole examined underground. Generally, longer charging periods will result in a higher IP response compared to a short charging period. The time of the potential decay between the two potential electrodes during the off-sequences can vary and depends on the overall measurement configuration and environmental conditions (Reynolds, 2011).

3.2.4. Frequency-domain measurements

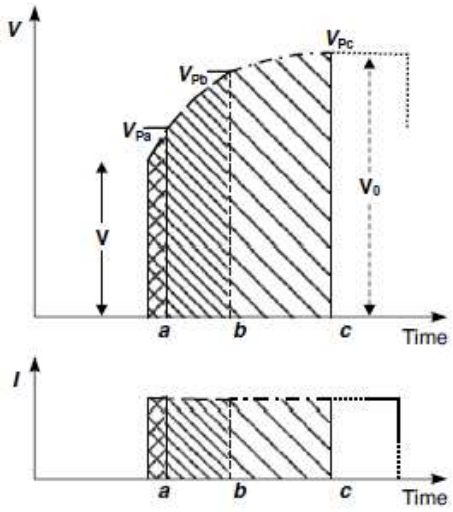

Figure 9: With an increase in the charging time (from a over b to c) results in a drop of the frequency of measurement and in a raise of the overvoltage from V_{Pa} over V_{Pb} to V_{Pc}. Hence, revealing higher apparent resistivity at lower frequencies (e.g., c) compared to lower apparent resistivity at higher frequencies (e.g., a) (Reynolds, 2011).

Frequency-domain measurements are characterised by induced polarisation measurements of variable frequencies. Two frequencies below 10Hz are used for measuring the apparent resistivity which has greater values for low frequencies ρ_{a0} and is conversely lower for higher frequencies ρ_{a1}, *Figure 9*. Defining the span of the decay is not possible due to its shortness in time. Therefore, the total amplitude of voltage with regard to the induced current is measured. Resulting in a certain resistance value *R* that is then multiplied by the belonging geometry factor pursuant to the used configuration. Using an electric current which is switching in polarity (on- and off-sequences) with a certain time delay equal to the length of the charging time, is comparable to the utilization of alternating current at a specific frequency. Usually, a general trend is observable which constitutes that the charging and delay times are shorter when the frequencies are high and therefore the apparent resistivity is larger at low frequencies (Reynolds, 2011).

According to Lowrie (2007), the apparent resistivities at two low frequencies need to be obtained to utilize the frequency reliance of the IP effect. This can be outlined as the frequency effect FE, denoted in *Equation (13)*, multiplied with 100 for eventuating in the percentage frequency effect PFE, *Equation (14)*:

(13)

$$FE = \left(\frac{\rho_{a0} - \rho_{a1}}{\rho_{a1}}\right)$$

(14)

$$PFE = 100\left(\frac{\rho_{a0} - \rho_{a1}}{\rho_{a1}}\right) \leftrightarrow 100\left[\frac{\sigma(\omega_1) - \sigma(\omega_0)}{\sigma(\omega_0)}\right]$$

ρ_{a0}: apparent resistivity at low frequencies
ρ_{a1}: apparent resistivity at high frequencies

Reynolds (2011) constitutes that the equivalence between the frequency-domain and the time-domain is the frequency effect FE and the chargeability where in poorly polarisable environment the frequency effect FE is lower than 1.

Another important parameter for interpretation is the metal factor MF, also called the metal conduction factor, which is a modulation of the frequency effect as claimed by Marshall and Madden (1959), *Equation (15).*

(15)

$$MF = A\left(\frac{\rho_{a0} - \rho_{a1}}{\rho_{a0}\rho_{a1}}\right) \leftrightarrow A(\sigma_{a1} - \sigma_{a0}) \leftrightarrow A \times \frac{FE}{\rho_{a0}} \leftrightarrow A \times FE \times \sigma_{a0}$$

σ_{a0} and σ_{a1}: apparent conductivities($=1/\rho_a$) at low and high frequencies
$\rho_{a0} > \rho_{a1}$ and $\sigma_{a0} < \sigma_{a1}$ and $A = 2\pi * 10^{-5}$
FE: frequency effect

The named parameters are used for further interpretations of the measurement data and therefore a deeper understanding of the theoretical background is inevitable. A profound knowledge of the origin and drivers is required to set the right choices for analysing and figuring out usable data and erroneous data that should not be considered.

4. Landfill Mining

In contrast to the historical assumption that landfills are the solution to the waste problem, Krook et al. (2012) highlight the problems associated with them, such as methane emissions over many years and the local pollution that can be caused by the deposited waste. An innovative approach to solving or at least reducing these problems is landfill mining: this is the process of excavating, processing, treating and recycling the landfilled materials. This can also counteract the omnipresent space problems for landfill expansions as well as for new landfills. According to Hogland et al. (2011), some factors, such as the quantity and quality of the materials contained, as well as the local situation and the current market price, determine the value of the landfilled materials. Landfills that were operated between 1960 and 1995 are therefore best suited for material recovery, because after 1995 many countries in the European Union started to introduce specific separation processes for valuable materials. Hermann et al. (2014) show that there are several factors influencing landfill mining projects that should not be ignored. These include economic and ecological factors, but also technical aspects. In addition, organisational, political and legal issues must be taken into account. Each project requires a very specific consideration of these influencing factors, as there is currently no standardised evaluation system for this. Among other things, a multitude of studies in various directions will be necessary.

4.1. Extracts from literature examples for landfill mining

Abu-Zeid et al. (2003) present in their work the combination of IP measurements with classical resistivity tomography in the area of a municipal solid waste landfill. The aim was to characterise the composition of the leachate by geochemical and geophysical investigations. Such investigations are of special interest for environmental aspects, as they can provide information about possible leaks and the spreading of these pollution plumes. *Figure 10* shows a comparison of the inversion models of the (a) resistance measurement and (b) the IP measurement: one can clearly see the correlation between areas with lower resistances and higher chargeability values. The near-surface layer with higher resistivities is referred to as the top-capping material of the landfill, which generates low chargeability values due to its loose bedding and higher sand content. Those areas with higher chargeability values and low resistivity values are sediments saturated with brackish or saline water. As can be seen in *Figure 10 (a)* and *Figure 10 (b)*, the conductive areas are clearly delineated and do not show any smearing that would indicate leachate penetrating through the landfill liner. The measurements were done with Wenner configuration, the chargeability values for these regions are >10ms and the resistivity values are <50ohmm.

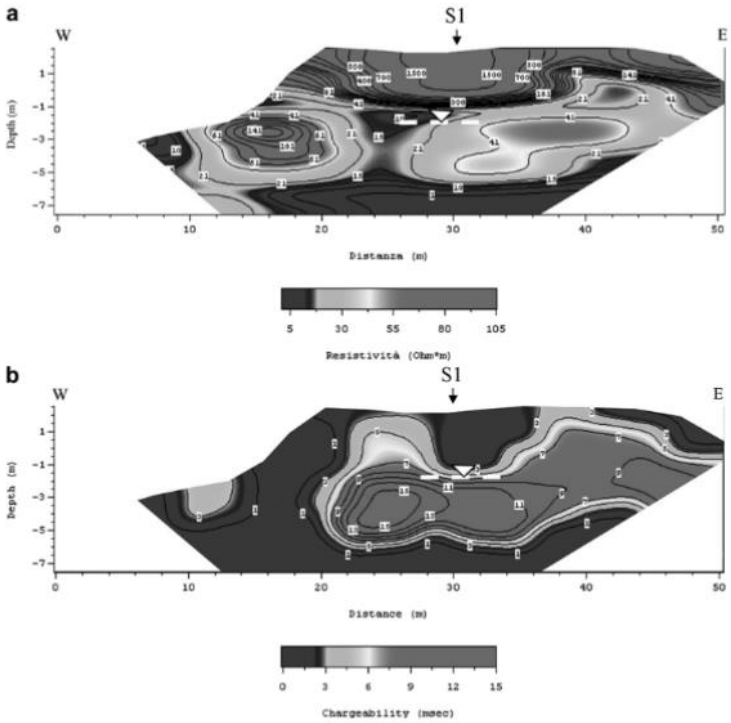

Figure 10: Representation of a 2D tomographic section along the landfill. S1 is the designation of a borehole intersected by this profile. Shown is in: (a) the resistivity and in (b) the IP-chargeability (Abu-Zeid et al., 2003).

Another example of combining resistivity measurement and induced polarisation to study landfills is given by Cardarelli and Di Filippo (2004) who conducted a geophysical investigation of a landfill containing urban waste. In particular, the study on site 3 by Cardarelli and Di Filippo (2004) offers opportunities for comparison with those carried out in the course of this work. The analysis of the geoelectric measurements from site 3 are shown in *Figure 11*. *Figure 11 (a)* shows the resistivity tomography, which gives a good general overview of the landfill. There is clearly an area of low resistivity running like a band through the middle of the profile, bounded at the top and bottom by slightly higher resistivity values. Particularly high resistance values occur at the beginning of the profile. *Figure 11 (b)* shows the inversion model of the IP data as chargeability in *ms*. The authors attribute these measured values to the deposition of inert sludge from municipal sewage. The correlation between low resistivity values and high chargeability values suggests the presence of fluid flow (leachate) enabled by the drains located in this area.

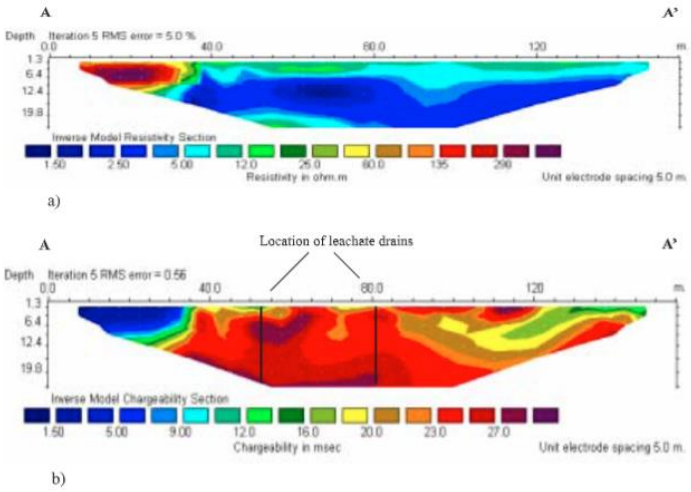

Figure 11: Plot of inversion results for site 3 measurements (a) is the resistivity inversion model and (b) is the IP inversion model (Cardarelli and Di Filippo, 2004).

Cardarelli and Di Filippo (2004) have classified the different measurements, which are listed in *Table 3*. This classification refers to the inversion models shown in *Figure 11 (a)* and (b).

Table 3: List of the classification of measured resistance and chargeability values for site 3 (Cardarelli and Di Filippo, 2004).

Resistivity ERT [Ωm]	Chargeability IP [ms]	Note
10 – 30	10 – 20	Urban
1 – 5	20 – 30	Saturated waste (leachate)
>100	<2	Inert sludge
5 – 30	5 – 50	Soil near the dump (organic liquids soak the terrain)
-	-	Soil outside the dump (unpolluted)

An example of the application of induced polarisation in the frequency-domain and in the time-domain is provided by Flores-Orozco et al. (2021). Although this example concerns the exploration of a graphite deposit, the results give a good insight into a possible data distribution. *Figure 12* shows an evaluation that gives a good overview of the results of the different measurements done along two profile lines. Measurements were made in the time-domain (TDIP) as well as in the frequency-domain (FDIP). For the measurements in the frequency-domain, the two measurement frequencies 0.5Hz and 15Hz were selected. The models in *Figure 12* show good agreement and a consistent picture of the subsurface. According to Flores-Orozco et al. (2021) the large anomaly in *Figure 12 (b)* TDIP is to be evaluated as an artefact, as the measurements with direct current react extremely sensitively to external sources of interference. In contrast, the deeper anomalies of the FDIP measurement are to be considered polarised areas, whose actual shape, however, may be distorted by the great depth. This is due to the fact, that in this case the sought graphite ore is close to the surface, which reduces part of the current flow to deeper layers. The recognisable anomalies in *Figure 12* are created by the presence of graphite, with the differences in polarizability within these anomalies suggesting varying amounts of graphite ore.

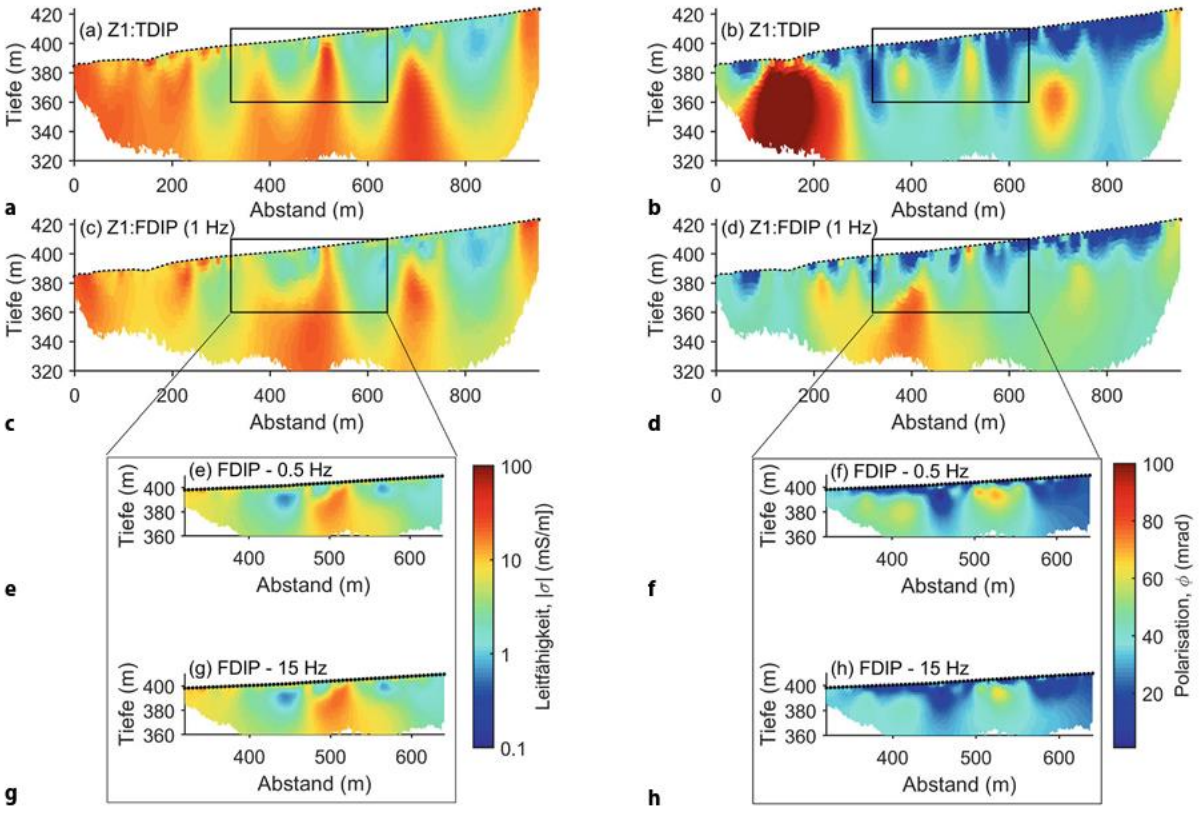

Figure 12: Presentation of the tomographic results of the field measurements carried out: profile Z1 in direct current measurements (a) and (b), the alternating current measurements (c) and (d), as well as the spectral IP that has been carried out along profile 2 (e) – (h) (Flores-Orozco et al., 2021).

Of particular interest for the subsequent evaluation of this work is that the scale of the phase angles for the evaluation of the induced polarisation has an upper limit of 100mrad, see *Figure 12 (f)*. From this it can be concluded that phase angles >100mrad have no significance and are therefore not included in the evaluation.

Flores-Orozco et al. (2021) emphasize one aspect: the results of the spectral induced polarisation, see *Figure 12 (f)* and *Figure 12 (h)*, show that at a low frequency, here 0.5Hz, the maximum of the polarisation effect is reached.

These three examples are representative of a whole spectrum of investigations already carried out on landfill bodies using geophysical, especially geoelectric, measuring methods. Due to the specialisation in the detection of metals with the induced polarisation method, the scope of literature examples and comparable investigations is limited. In addition, the number of examples of IP measurements in the frequency-domain is very limited, which is why only the example by Flores-Orozco et al., 2021, is treated as a representative example.

5. Field work

Several sensible placed profile lines were used to obtain enough IP data for interpretation and find adequate conclusion or guideline to improve prospective surveys. Therefore, a certain amount of fieldwork was necessary in order to acquire data from diverse measurement configurations and to enable the use of different equipment and electrodes to approach the time-domain as well as the frequency-domain and for neglection of possible unwanted effects such as electrode polarisation.

5.1. General task

The fundamental task of this thesis is the analysis of IP data recorded from field work including several comparable datasets with the primary aim of finding IP responses generated by a knowingly chosen metal source. The impulse for surveying this specific topic was once the precursory Bachelor Thesis which was also covering parts of geoelectrical methods, but with a larger focus on frequency depending resistivity measurements and secondly the fact, that many geoelectrical measuring devices are acquiring IP data besides the original resistivity surveys. So, there is an additional dataset to almost each resistivity measurement which is in many cases not considered for interpretation. Additional input was provided by the project called RAWFILL of Interreg North-West Europe which is about a recycling based circular economic for raw materials that are retrieved from landfills (Interreg North-West Europe RAWFILL, 2022).

5.1.1. RAWFILL

The RAWFILL project from Interreg North-West Europe is focused especially on landfill mining which is planned to be carried out commonly in the north-western region of the EU. This covers the process of finding still useful materials in landfills that are suitable for bringing them back in a recycling process to obtain worthwhile resources that would otherwise rot in disposal sides. Several geophysical survey methods such as electro-resistivity methods, seismic or electro-magnetic methods constitute cheap ways to determine the economic potential of a certain landfill (Interreg North-West Europe RAWFILL, 2022). Furthermore, they are invasive and therefore used prior to excavation (Bernstone et al., 2008). Especially the juxtaposition of the electric resistivity tomography ERT and the induced polarisation IP contains fundamental issues that were leading drivers for this thesis in the first place, although the final conclusion will slightly derogate from this original questioning.

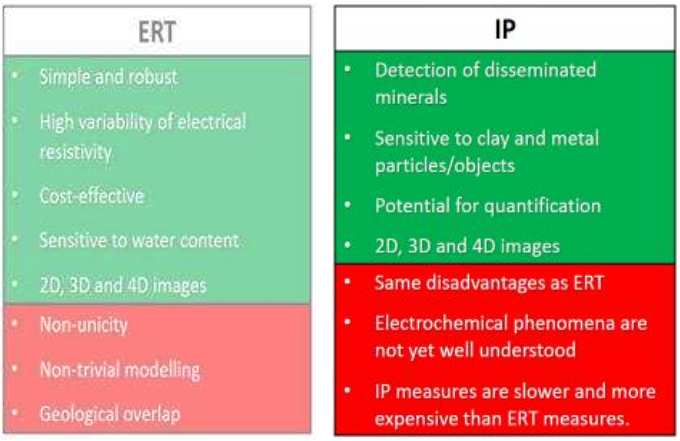

Figure 13: Comparison of the pros (green) and cons (red) of the electric resistivity tomography ERT and the induced polarisation IP (Interreg North-West Europe RAWFILL, 2022).

The advantages of each method are highlighted in green, the disadvantages in red, Figure 13(Interreg North-West Europe RAWFILL, 2022). The central point will be the analysis of 2D IP data to simply gain more information about the processing and the overall data quality in different lines but the ERT data which is measured simultaneously will be considered as well.

5.2. Test site Allerheiligen in the Mürz valley

The survey took place on the landfill Allerheiligen in the Mürz valley which has been in operation since 1979 and is managed from the AVW Mürzverband. The entire company premises cover an area of 14 hectares. In addition to the bulk waste landfill, there is also a recycling yard and a centre for hazardous or special waste as well as a waste treatment plant. The first expansion phase of the landfill lasted from 1979 to 1996. During this time, mechanical-biologically treated waste material (MBT material) and untreated or mechanically treated bulky and residual were deposited. In the second expansion phase, from 2012 no MBT material was deposed but only small amounts of already pre-treated bulk waste were lodged. The landfill area was divided into four zones in which material was deposited during different periods of time. The examined profile lines are all in sector 1 which is the oldest part of the landfill in which the material was deposited to a depth of approximately six meters below ground level (Wolfsberger, 2015, unpublished data).

Figure 14 shows the geographical overview of the measuring area in Allerheiligen in the Mürz valley which is located roughly 20 minutes eastwards from Leoben. The nearby river Mürz and the generally existing geology have no influence on the measurements, since the landfill body can be viewed as a separate system.

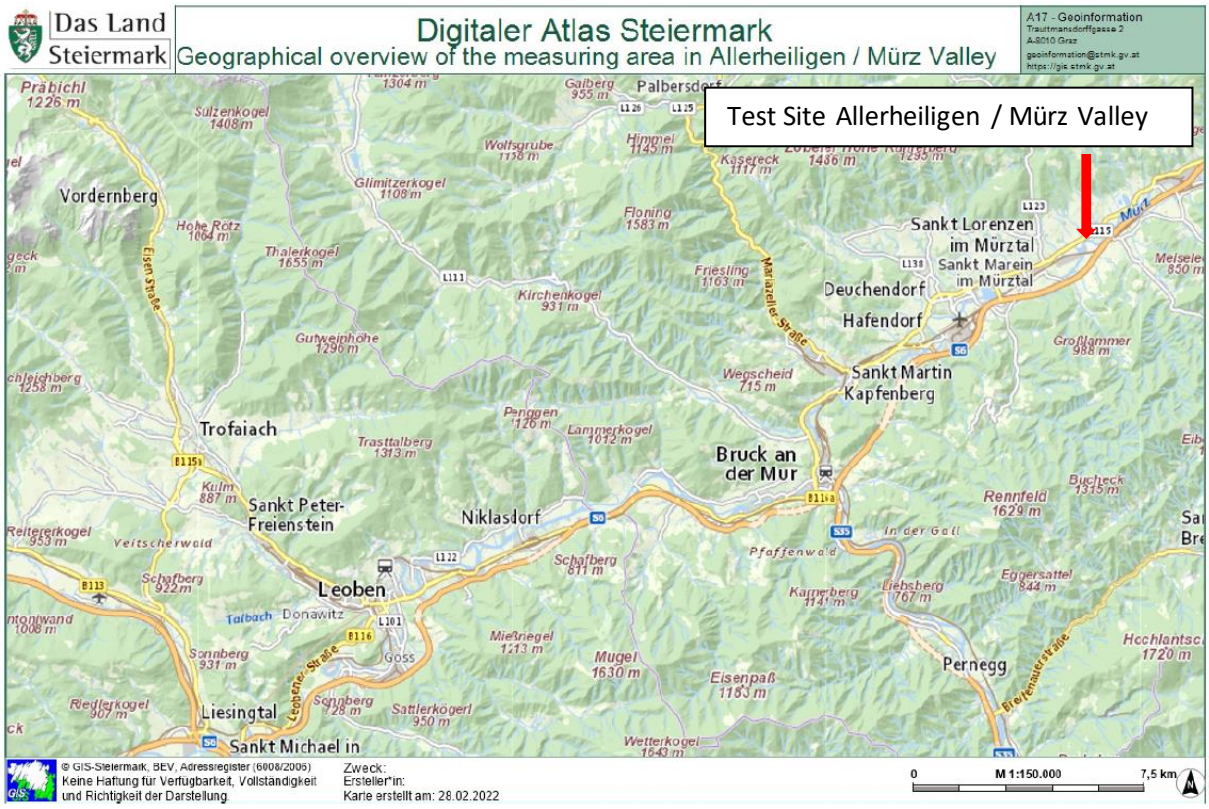

Figure 14: Geographical overview of the measuring area in Allerheiligen in the Mürz valley (GIS Steiermark, 2021).

5.2.1. Previous investigations

The aim of the investigations in 2013 and 2014 was the detection of metallic components. With the electromagnetic and geomagnetic methods used, the total magnetic intensity and the associated vertical gradient were measured at approximately 1200 measuring points and the electrical conductivity at approximately 1600 measuring points. No statements could be made about the metal content of the landfill based on the overall conductivity, since the water content in the upper soil areas was too high and blurred the signal. The direct current geoelectric reacts in particular to the electrolytic conduction of the current flow, which is caused by the pore water. In contrast, the influences of conductive metallic components that are spatially separated from each other are relatively small. Measurements with a distance between the electrodes of a=2m and a=5m resulted in conductivity values of 50-100mS/m in areas close to the surface. Measurements with a inter electrode spacing of *a*=10m showed a significant decrease in conductivity below 50mS/m in deeper areas. This increase in resistance with greater exploration depth provides evidence of the influence of surface water on the

total conductivity (Scholger, 2015). The problematic of the water content overtaking the role as dominant controller over the resistivity dispersion of landfills is also mentioned by Bernstone et al. (2008).

Due to the results of Scholger (2015) the overall metallic content of the landfill in section 1 can be assumed to be neglectable.

Therefore, a metallic target was chosen on purpose for the induced polarisation methods. For this, two of the gas domes were defined as metal source to generate a sufficient IP response apart from the overall metal-free surrounding soil.

5.2.2. Survey in May 2021

The first survey campaign set place in late May of 2021 and the realised measurements are listed in the *Appendix A*. Generally, 40 measurements were done, split in N-S and W-E profiles crossing directly at the metal target gas dome which was always placed in the middle of each profile line, *Figure 15*. The field work started with choosing suitable profile lines and calibrating them with the Garmin GPS gadget as well as manually due to the overall small distances which were strongly influenced by the inaccuracy of the GPS device.

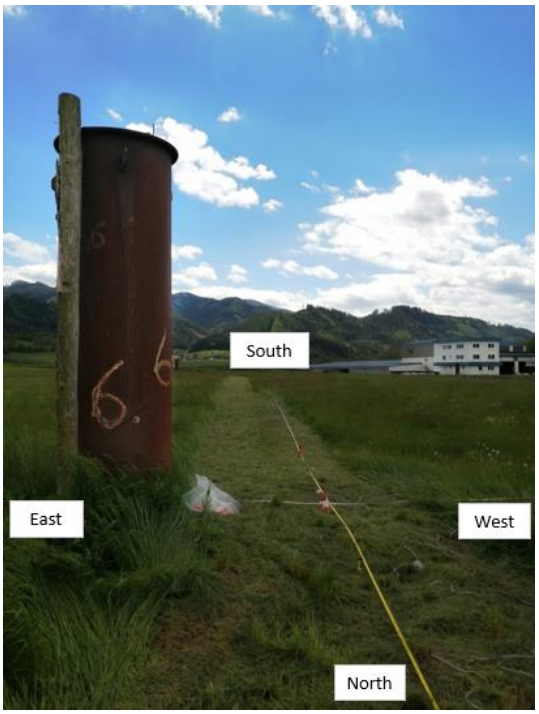

Figure 15: Showing the crossing of the profile lines directly next to the gas dome which was the metal target for detecting IP responses.

The gas dome is part of the degassing system which is used for the collection and controlled discharge of accruing landfill gas (DVO, 2008). Landfill gas is by definition greenhouse gas accumulating inside disposal sites mainly consisting of methane and carbon dioxide which is generated by biodegradation of municipal waste without any oxygen supply in a so-called anaerobic environment (Ahmed et al., 2014).

In order to be able to better assess the influence of moisture caused by rain, the weather conditions at the time were also taken into account, *Figure 16*. The end of May was characterized by a drier phase, preceded by heavy precipitation in mid-May (Wetter Online, 2021).

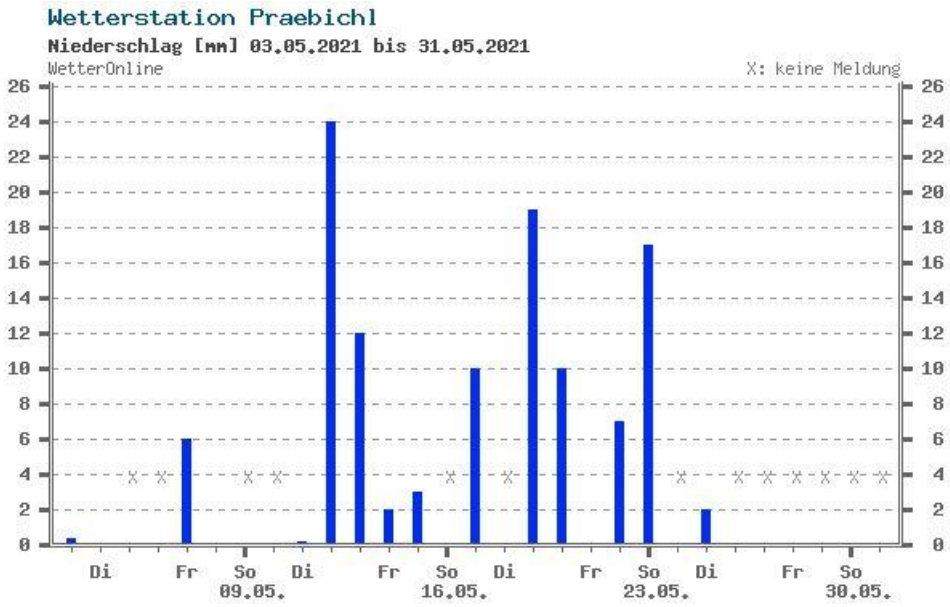

Figure 16: In order to be able to better assess the influence of moisture caused by rain, the weather conditions at the measurement time in May 2021 were also taken into account (Wetter Online, 2021).

5.2.2.1. Measurement settings

The *4point light 10W* from Lippmann geophysical instruments was used to carry out the geoelectrical measurements. It is an earth resistivity meter mainly applicated amongst others in any kind of environmental investigations and with the additional ability to measure the induced polarisation. The recommended frequency of 4.16 Hz is set as default for measurements in Europe, based on the ideal oppression of the mains frequency and its harmonic. (Lippmann, 2014). According to Reynolds (2011) frequency-domain measurements are based on using low frequencies for creating optimal measurement settings for induced polarisation. Therefore, the selected frequencies are chosen respectively to the smallest possible settings, including the default frequency, *Table 4*:

Table 4: List of frequencies that were used during the measurements in May 2021.

used frequencies:	[Hz]	[Hz]	[Hz]	[Hz]	[Hz]
	4.16	2.08	1.04	0.52	0.26

According to Vogelsang (1993), geophysical measurements for investigations close to the surface require close-meshed measuring arrangements in order to enable precise statements to be made about the shallow depth effect. For this reason, an electrode spacing of a=2m was chosen and a sum of 27 electrodes were used, resulting in a total length of 52m for each profile line in North-South and West-East direction.

The *4point light 10W* was set to remote mode and controlled by an external computer for setting further measurement settings by using the software *GeoTest* which is a program for managing geoelectrical measuring devices and for data acquisition with lines up to 100 electrodes (Rauen, 2021).

Wenner and Dipole-Dipole configurations were chosen in order to make the best possible use of the respective advantages. Furthermore, in addition to the conventional metallic electrodes, so-called non-polarisable electrodes filled with $CuSO_4$ and with tips of wood and plaster were also used.

Due to some suspicious IP responses which were detected during quick inversions while measuring, the presence of other metal objects along the profile line must be foreclosed. Therefore, an electromagnetic survey measuring the horizontal and vertical dipole along the profile with the use of the *EM31* from Geonics Limited Mississauga Canada was done, *Figure 17 (a)*.

Due to the possible influence on the conductivity, ground temperature measurements were also taken in order to be able to take account of areas with abnormal temperatures when interpreting the geoelectric measurement result, *Figure 17 (b)*.

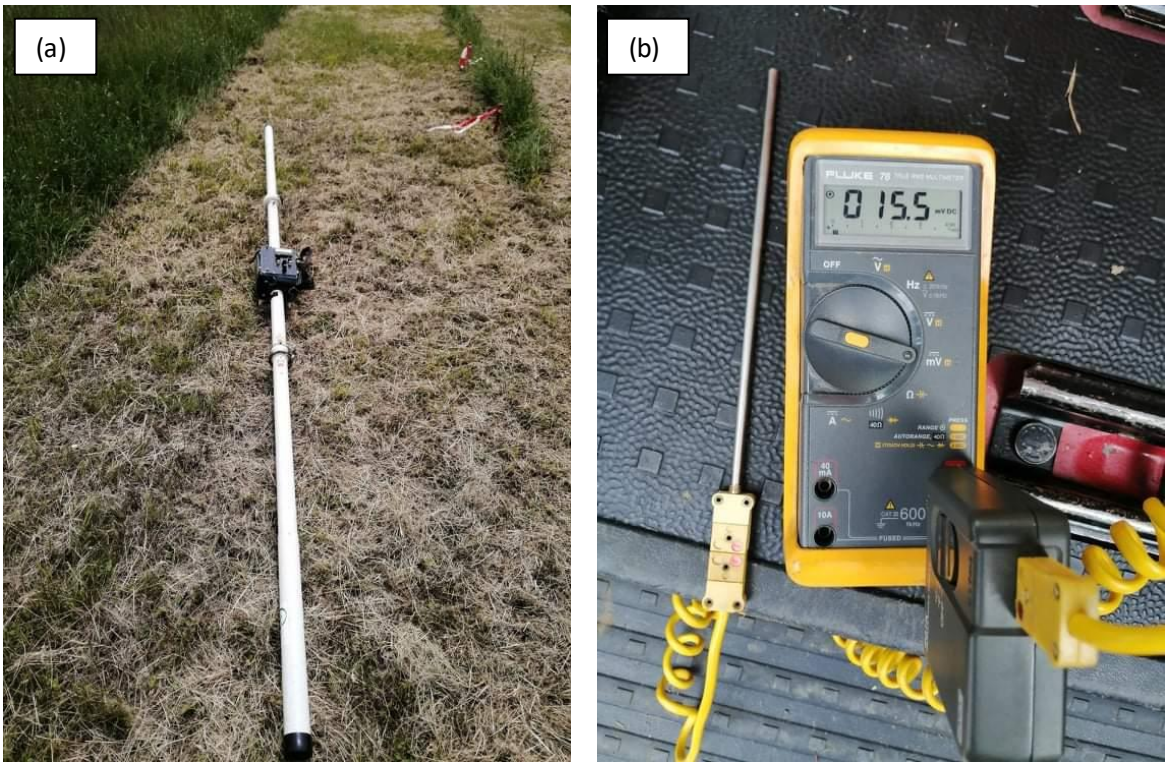

Figure 17: Additional measurements to support the interpretation of the geoelectrical measurements in May 2021: (a) electromagnetic equipment EM31 from Geonics Limited Mississauge Canada (b) ground temperature measurement was done with a voltmeter and a ground thermometer.

5.2.3. Survey in November 2021

Due to a research project at the University of Natural Resources and Life Sciences, the gas dome from the measurements in May 2021 was removed and replaced by a methane oxidation window. Therefore, a new gas dome further west in sector 1 was selected for the further measurements. Due to the spatial proximity to the original gas dome, the underground conditions can be classified as sufficiently similar. Based on the first results from the measurements in May 2021, these further investigations were adjusted accordingly. In this case, three profile lines were drawn parallel to one another from east to west, with the gas dome again being in the middle of the lines each time, *Figure 18*. In addition to the *Lippmann 4point light 10W*, another geoelectric gauge called the *Mangusta System MC 24/144E* from Ambrogeo Instruments was used in the November 2021 measurements. All measurements performed are listed in *Appendix B* and *C* according to the electrode configuration used, the number of electrodes and the measurement settings.

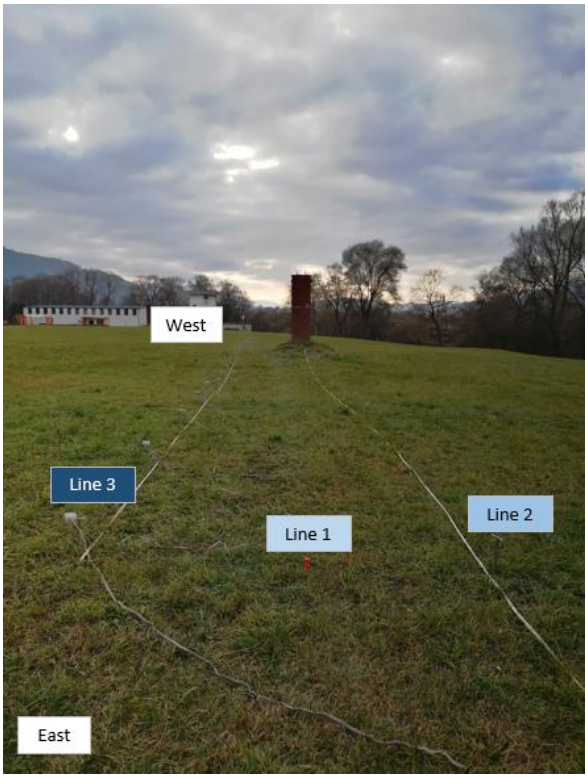

Figure 18: Overview of the three parallel profile Lines (1, 2 and 3) in West-East direction with starting point in the East and with the metal gas dome as target in the middle.

In order to enable a spatial relationship to each other, the lines were again measured with the Garmin GPS as well as manually. The absolute distance between Line 2 and Line 1 is 1.0 m and Line 1 and Line 3 are 1.40 m apart from each other.

Again, the weather conditions were observed in order to be able to determine any influence of rain showers on the water content in the landfill. *Figure 19* shows the weather conditions for November 2021. The measurements were carried out in mid-November and on another day at the end of November and were not influenced by heavy rain events (Wetter Online, 2021).

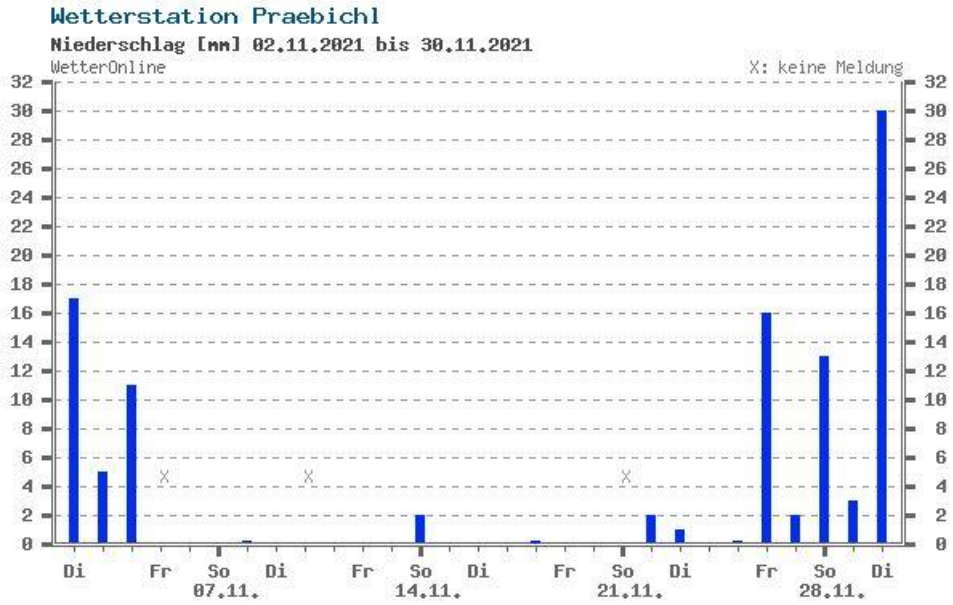

Figure 19: In order to be able to assess the influence of moisture caused by rain, the weather conditions at the measurement time in November 2021 were also taken into account (Wetter Online, 2021).

5.2.3.1. Measurement settings

In order to obtain a comparison with the results of a time-domain and a frequency-domain induced polarisation, the defined profile lines were measured with both the *Mangusta System MC 24/144E* and the *4point light 10W*. Based on the results of the measurements already received in May 2021, the lowest frequency of the *4point light 10W* could be dispensed with entirely, since it did not provide any better measurement quality or additional information, but only led to a significantly longer measurement duration, *Table 5*. The selected settings of the *Mangusta System MC 24/144E* for measuring the delay of the IP response in seconds as well as the delay from rising edge can be found in the *Appendix B*.

Table 5: List of frequencies that were used during the measurements in November 2021.

used frequencies:	[Hz]	[Hz]	[Hz]	[Hz]
	4.16	2.08	1.04	0.52

As with the measurements in May 2021, non-polarisable electrodes were also used in addition to the conventional metal spikes. However, the number had to be reduced from the original 27 to only 10, as the wooden tips were broken and the permeability was too high, resulting in too great loss of $CuSO_4$. Therefore, only the remaining 10 with plaster tips could be used. These were then interposed in the middle of the profile line in order to reproduce the effect on the metal target as unadulterated as possible. The metal skewers were used for the necessary remaining electrodes. 24 and 48 electrodes

with a spacing of *a*=1m or *a*=2m were used for the measurement of the three lines. This results in a general length of all lines of 48m with the starting point in the East.

Due to the results of the ground temperature measurement and the evaluation of the electromagnetic investigation from May 2021, these additional measurements were not carried out in November 2021.

5.3. Measurement Equipment

In the following, the geoelectrical measuring instruments used and their basic working method are described. The additional use of a second measuring device for the measurements in November 2021 means that the time-domain can also be covered and opens up the possibility of a comparison with the frequency-domain measurements. For the measurements in Mai 2021, however, only the frequency-domain was measured, as the second measuring device was not yet available at that time.

5.3.1. 4 point light 10W

The *4 point light 10W* is an earth resistance meter from *Lippmann* that is basically used to measure the resistance of the subsoil, which allows conclusions to be drawn about the soil type and water content. The general set-up consists of 4 electrodes: whereby the current is induced via electrodes *A* and *B* and the voltage is measured via electrodes *M* and *N*. In parallel, the induced polarisation can also be measured with each standard resistance measurement. The meter measures in the frequency-domain, where by measuring the phase shift between the output current and the voltage, information about the induced polarisation is obtained. For this purpose, not only the potential difference is measured, but also the phase shift between the output current electrodes *A* and *B* and the voltage at the electrodes *M* and *N*. This recorded phase shift is then specified as voltage U_{90}. This is also called out-of-phase voltage and is generally about 2 to 3 orders of magnitude below the so-called in-phase voltage, abbreviated to U_0. The phase shift can be calculated directly with the following *Equation (16)*:

(16)

$$\varphi = \frac{U_{90}}{U_0} * 1000\ [Phase\ shift\ in\ mrad]$$

With 1 mrad = 0,0572 degree
U90: out-of-phase voltage
U0: in-phase voltage

This phase shift can be seen as a direct indicator of the induced polarisation of the subsurface. The accuracy of the instrument is given as 0.1% with a maximum resolution of 100nV (Lippmann, 2014).

Figure 20 shows a typical measurement setup of the *4 point light 10W*. The core piece is the measuring device itself, which is directly connected to the measuring computer, to the row of electrodes and to the external power supply in the form of car batteries. With the so-called remote function, the measuring process can be completely controlled via the measuring computer with the help of the *Geotest* software. All necessary inputs for the electrode configuration as well as other measurement settings are adjusted directly in this software.

Figure 20: Representation of the measurement setup for a geoelectric measurement with the 4 point light 10W from Lippmann.

5.3.2. Mangusta System MC 24/144E

The *Mangusta System MC 24/144E* is a Multichannel Electrical Imaging System from Ambrogeo Instruments. In contrast to the *Lippmann 4 point light 10W*, it measures in the time-domain and thus corresponds more to a measuring device that is used in classic industrial projects. Again, parallel to the usual earth resistance measurements, the induced polarisation can also be recorded. In this case, the phase shift is not measured, but the so-called decay time and the rise time are used. These two parameters are dependent on the geological structure of the subsurface and can therefore be applied to reconstruct underground structures. Since the correct measurement of the polarisation potential is extremely difficult, the *Mangusta System MC 24/144E* measures the potential in time intervals instead. The values obtained are then integrated taking time into account. This results in the area between the

so-called discharge curve and the corresponding time axis. As already mentioned in *Equation (12)*, the chargeability given in milliseconds is then calculated. The precession of the instrument is given as 0.2% (Ambrogeo Instruments).

Figure 21 shows a typical measurement setup with the *Mangusta System MC 24/144E*. A car battery is again used as the external power source. In addition to the actual measuring device, there is also a control unit to control the power supply. The measurement setting as well as the general control of the measurement is carried out directly via the laptop.

Figure 21: Showing a typical measurement setup with the Mangusta System MC 24/144E, associated current control until as well as the measurement computer and external current supply.

5.3.3. Different used electrode types

Different types of electrodes were used: on the one hand, the classic metal probes that are also used as standard for earth resistance measurements, on the other hand, non-polarisable electrodes were also used. These non-polarisable electrodes are filled with $CuSO_4$, as this has a buffering effect on the transition from electrical conduction in the metallic electrode to ionic conduction in the soil electrolyte. Chemical impedance inconsistency occurs at the surface of the metallic electrodes due to the dissimilarity of transport mechanism of electric charges between these electrodes and the soil pore-fluid electrolyte (Everett, 2014). This electrode polarisation can lead to an artificial voltage at the surface which may result in misinterpretation of wrong surface chargeability zones. LaBrecque and Daily (2008) have proven that the polarizability of the metallic electrodes is subject to the sort of metal. By using non-polarizable electrodes, this electrochemical imbalance and the risk of misinterpretation can be minimized. Non-polarizable electrodes have the special property of a constant potential even if they are traversed by an electric current, as claimed by Bard and Faulkner (1980).

Figure 22 shows the different types of electrodes that have been used. In *Figure 22 (a)* one can see a non-polarisable electrode: this is a plastic case filled with $CuSO_4$ (blue liquid) and a permeable tip made of wood or plaster. This is then connected with a cable to the so-called *Act-Ele Box* by *Lippmann*. This *Act-Ele Box* is connected to the others via measuring cables and is used to switch the electrodes as current or potential electrodes and to record the measurement data. In *Figure 22 (b)* a metal skewer from *Lippmann* is shown, onto which the *Act-Ele Box* can be directly attached. *Figure 22 (c)* shows a classic metal electrode, which is also used in many commercial projects, as it is relatively insensitive to damage and easy to handle. The crocodile clip is then used to connect it to the multi-channel measuring cable.

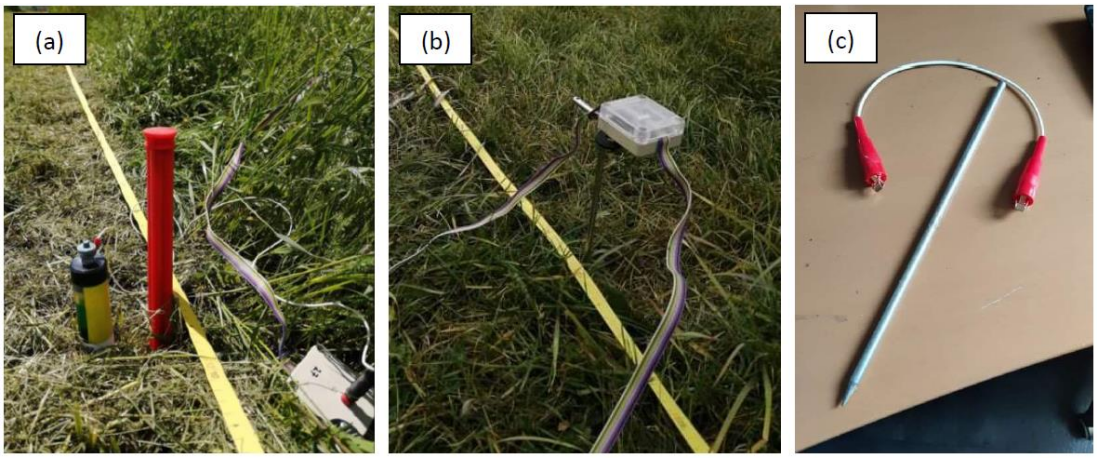

Figure 22: Illustration of the different types of electrodes used with (a) non-polarisable electrode with Act-Ele box from Lippmann (b) metal spike with Act-Ele box attached and (c) classical metal electrode for the Mangusta System MC 24/144E.

6. Laboratory survey

Another aspect are the laboratory measurements that have been carried out in addition to the field measurements in the basement of the Institute for Geophysics. For this purpose, the *4point light 10W* measuring device from *Lippmann* was used and measurements were taken in the frequency-domain.

6.1. General Task

The aim of the laboratory measurements was to present a scaled-down model of a landfill including geophysical prospection measurements. The different soil layers that were placed in the tank were to represent a landfill body including contents made of different materials. Through the targeted control of the water supply or the draining of the water, different degrees of saturation can be achieved and thus a natural drying effect of arid phases after previous periods of intensive precipitation can be imitated.

6.2. Experimental setup

The general experimental setup was taken from a previous Master Thesis by Stiegler (2019), which deals with the development and testing of geophysical prediction models for the composition of waste in landfills, and therefore did not have to be set up again. A 2000l plastic tank consisting of three chambers forms the test frame, whereby only one of these chambers with a volume of 218l is actually used. In *Table 6* the set-up parameters of the six electrode arrays are listed:

Table 6: List of the geometric parameters of the rows of electrodes attached to and in the tank (Stiegler, 2019).

marking	placement	number of electrodes	electrode spacing [mm]
A	vertically on the outside wall	25	20
B	vertically on the outside wall	25	20
C	vertically on the outside wall	25	20
D	vertically on the outside wall	25	20
U	inside the tank on the ground above the gravel, 45° twisted	31	20
O	ontop of filled material, runs on an imaginary line from A to C	31	20

Figure 23: Example photo of the iron granule installed in the tank, which serves as a metallic detection target.

In the course of this laboratory measurement, the installed iron granulate, *Figure 23*, was selected as the target object in this scaled-down landfill model in order to be able to study the efficiency of the induced polarisation in the field of landfill mining on the basis of a laboratory test.

At the base of the plastic tank is a layer of gravel with a thickness of *d*=470mm, which forms the basic building block of the experiment and extends under the first vertical electrodes. A separating fleece was placed on this, on which row *U* of electrodes is located. The remaining space was then filled with sand up to the uppermost of the vertical electrodes. Plastic and iron granules were installed in these to resemble a landfill structure. A thin layer of potting soil was applied as a final covering of the sand. Electrode row *O* enables a geoelectric resistivity measurement at the surface of the experimental landfill. In the course of his Master's Thesis, Stiegler (2019) dealt largely with various plastics, but these materials will not be discussed in more detail below. An important function is obtained by electrode row *U*, which is used to assess water saturation. Series *D* is of particular interest as it is intended to detect material with high conductivity, in the form of iron granules. These iron granules were installed

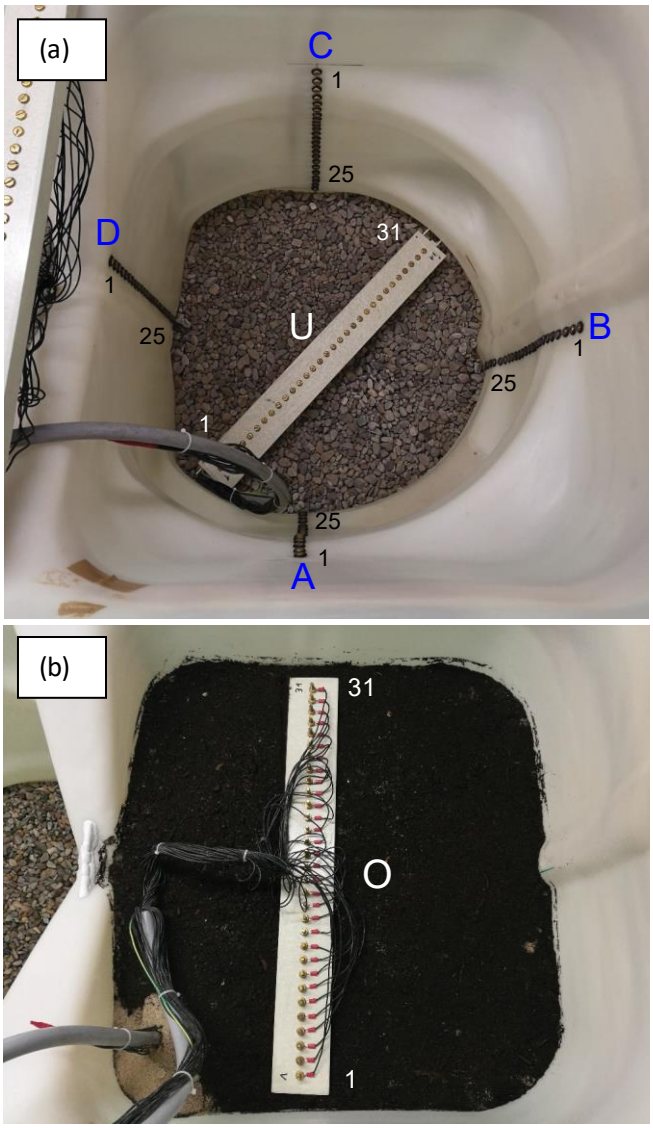

Figure 24: Illustration and description of the six different rows of electrodes that are attached to and in the tank (a) shows the situation before the sand layer (b) final situation with row O on top of the potting soil (Stiegler, 2019).

in the form of a cuboid with the following dimensions: width of 70mm, height of 20mm and depth of 8mm. The horizontal distance to the electrode row *D* is 50mm and the position of this iron target is in the middle of the profile between electrodes 12 and 13.

Figure 24 (a) shows the general test setup before the sand layer was introduced. The vertical rows of electrodes *A* to *D* can be seen on the side of the tank. The starting electrode close to the surface and the lowest electrode number 25 were also marked. The final configuration with rows of electrodes *O* on the complete installation on different materials can be seen in *Figure 24 (b)* (Stiegler, 2019).

For the measurement, the *Act-Ele boxes* of the *4 point light 10W* from *Lippmann* were closed on a grid plug-in plate connected to the electrodes on the tank. *Figure 25 (a)* shows the grid plug-in box and *Figure 25 (b)* the row of electrodes placed on the side of the tank to which the *Act-Ele boxes* are connected from the grid plug-in box via a cable system and which were used for the measurement.

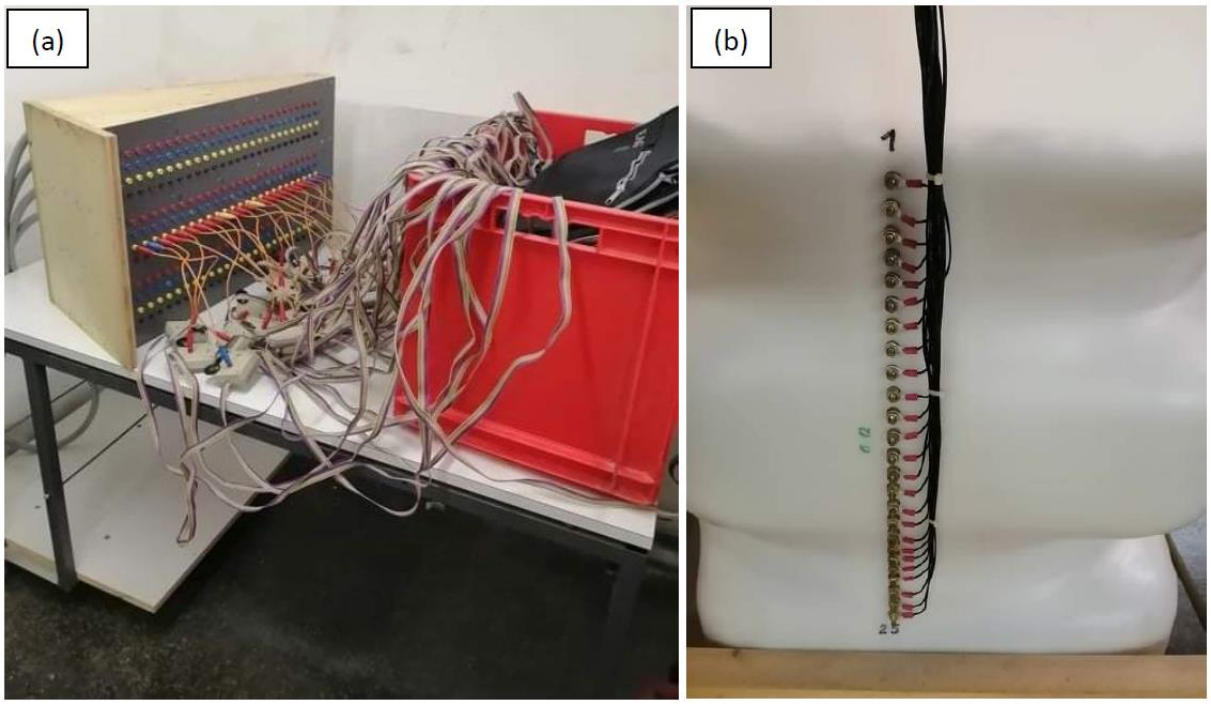

Figure 25: Shows the measurement set-up in the laboratory for the tank measurement with (a) the grid plug-in box and the associated Act-Ele boxes from Lippmann and (b) the associated row of electrodes placed on the side of the tank and used for this measurement.

Figure 26: The WTW TetraCond 3110 SET1 meter used for the temperature and conductivity measurements of the water in the tank is shown.

The tank was flooded to the lower edge of the humus layer for the first measurement. In order to estimate the conductivity of the water used for this purpose, measurements of temperature and conductivity were carried out. The *WTW TetraCond 3110 SET1* measuring instrument was used for this purpose, *Figure 26*.

This measurement setup was used both for a measurement run with almost 100% water saturation and in the subsequent drying process, where the water was drained to the upper edge of the gravel layer.

7. Data Evaluation – Laboratory Measurements

The data from the 100 field measurements obtained from the measuring instruments, as well as from the laboratory runs carried out, were imported into *Microsoft Excel* in order to be able to perform the data evaluation. Due to the good compatibility between the data formats and *Microsoft Excel*, as well as the possibility of clear representations and delimitations between the individual measurement-series, this programme was used for the evaluation. In order to get a better overview of the individual measurements, a corresponding overview table was created. This can be found in *Appendix A*, *B* and *C*. The measurements were categorised according to their name, measurement date, number of electrodes used, measurement configuration, frequency [Hz] or IP measure delay time [s] and the corresponding profile. In addition, a general subdivision was made into: Measurements May 2021 and measurements November 2021 as well as laboratory measurements.

Since the main focus is on the detection of the gas dome as a selected target metal object, the recorded IP effect is of particular interest. Therefore, a general statistical evaluation of these data was performed. In addition, various diagrams were created in order to visually represent the expression of trends between the compared parameters.

The measurements were therefore analysed individually, as well as with the corresponding comparison measurements or with the measurements of the same series of measurements, i.e., similar initial situation and measurement inputs.

7.1. Evaluation of laboratory measurements

Problems regarding the general conductivity in the model structure were already apparent during the implementation of the laboratory measurements. The measurement process began with full water saturation. The water was then drained up to the upper edge of the gravel in order to simulate drying out of the body of the landfill in arid times. Already during the measurement of the contact resistances, which was carried out before the actual measurement, it was noticed that these were clearly increased. In the case of the drying-out passage, such high contact resistances occurred that the measuring device was no longer able to measure them.

In order to be able to document the drying process adequately in terms of time, a so-called monitoring system was used that automatically runs through the individual measurement frequencies every 12 hours. The measuring frequencies used are listed in *Table 7*.

Table 7: List of frequencies that were used during the laboratory measurement.

used frequencies:	[Hz]	[Hz]	[Hz]	[Hz]	[Hz]
	4.16	2.08	1.04	0.52	0.26

The complete list of laboratory measurements can be found in *Appendix D*. There, the measurements are again listed categorically with regard to name designation, date, measurement frequency as well as measurement configuration. In addition, the measured temperature [°C] and conductivity values [µS/cm] are also added for the corresponding measurements. Both the room temperature and the temperature of the tank were measured.

7.1.1. Measurements T1 to T5 - complete saturation

Starting with the observation of measurements *T1* to *T5*, they were all carried out as so-called soundings in a period from 19.10.2021 to 28.10.2021. All frequencies in *Table 6* were measured one after the other.

Figure 27 shows a comparison of the contact resistances at almost complete water saturation for the measurement-series *T1* to *T5*. Already this compilation in *Figure 27* shows that the contact resistances were very high in the saturated state.

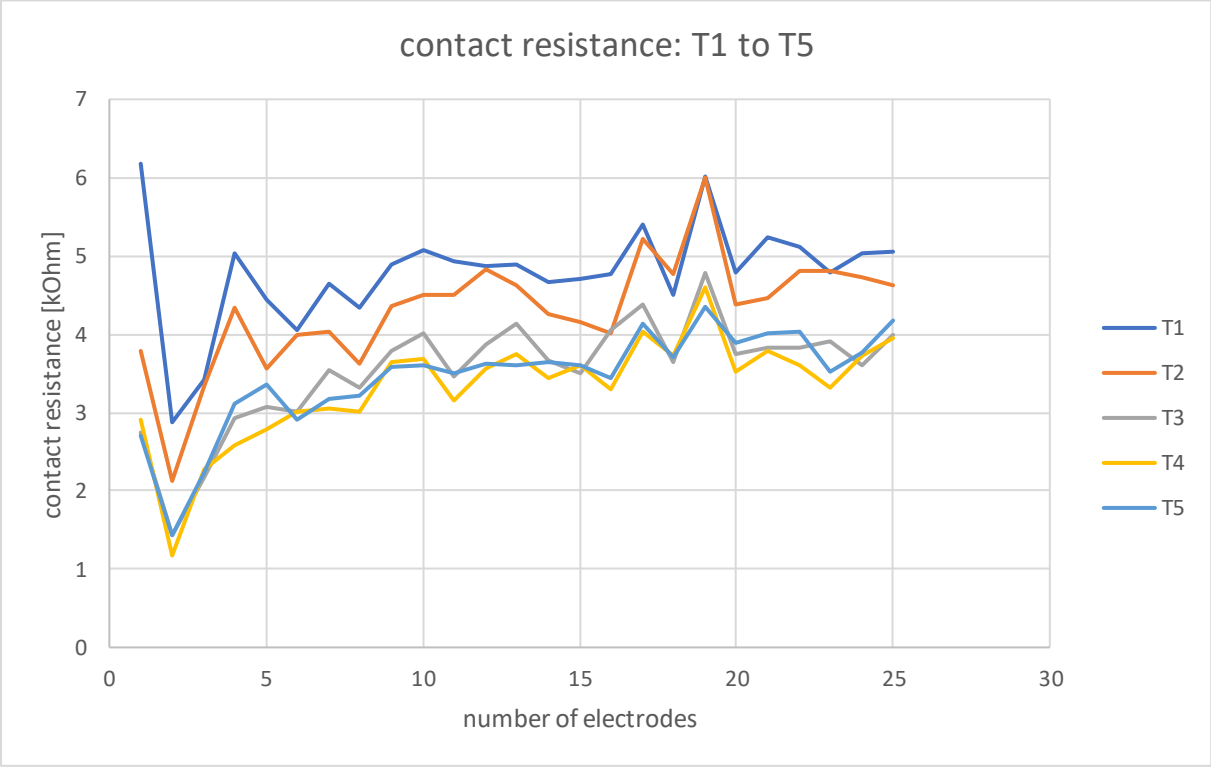

Figure 27: Diagram of the measurement-series T1 to T5 at almost complete water saturation. The individual settings and conditions of this measurement-series are listed in Table 8.

Table 8 lists the respective measurement settings and conditions of the measurement runs *T1* to *T5*

Table 8: List of measurement settings for measurement-series T1-T5 for fully saturated tank.

Name	Number of electrodes	Configuration	Frequency [Hz]	Temp. tank [°C]	Temp. room [°C]	Conductivity water [µS/cm]
T1	25	Wenner	0.26Hz-4.16Hz	12.8	19.5	398
T2	25	Dipole-Dipole	0.26Hz-4.16Hz	16.8	19.8	405
T3	25	Wenner	0.26Hz-4.16Hz	19.7	20.6	407
T4	25	Dipole-Dipole	0.26Hz-4.16Hz	19.8	20.6	405
T5	25	Wenner	0.26Hz-4.16Hz	19.8	20.6	404

Measurement *T1* started shortly after the tank was filled with water, so the difference between the room temperature and the temperature in the tank is the greatest. This is because the freshly filled water has not yet been able to warm up to room temperature within this short time. *Figure 27* shows a cross plot between the electrode array on the x-axis and the contact resistance [kOhm] on the y-axis. It can be clearly seen that the contact resistance is higher at the upper electrodes and then, from electrode number 2 onwards, a noticeable drop can be recognised. Subsequently, however, the contact resistances rise again, with the lower-lying electrodes reaching a positive peak. Subsequently, the contact resistance drops again somewhat.

In order to be able to make a well-founded statement about the measurements, a statistical evaluation of the *dU90* value is carried out first. The *dU90* value indicates the error of the measured voltage in %. This error is defined in *Equation (17)*:

(17)

$$dU90\ [\%] = ABS\left(\frac{standard\ deviation}{\sqrt{n} * U_{mean}}\right) * 100$$

n: number of measurements
$U90_{mean}$: arithmetic mean of all measured U

7.1.2. Detailed analysis of measurement-series T1

Table 9 lists the statistical evaluation of the *dU90* value corresponding to the individual measured frequencies of *Table 7*. These measurements from *Table 9* belong to measurement-series *T1* and are shown here as a representative. The list of measurements from *T3* to *T5* can be found in the *Appendix D*. One can clearly see that the mean value is significantly increased in all frequencies. The measurement with frequency 2.08Hz shows the relatively lowest values.

Table 9: List of the statistical evaluation of the dU90 values for measurement-series T1, split into the individual measurement frequencies of Table 7.

0.26Hz dU90 [%]		0.52Hz dU90 [%]		1.04Hz dU90 [%]	
min.:	3.541	min.:	2.104	min.:	0.128
max.:	5735.97	max.:	3802.61	max.:	6863.36
mean value:	160.438	mean value:	123.506	mean value.	151.057
median:	71.233	median:	68.174	median:	60.011
standard deviation:	616.899	standard deviation:	402.060	standard deviation:	710.522
variance:	384746.2	variance:	163428.9	variance:	510389.3

2.08Hz dU90 [%]		4.16Hz dU90 [%]	
min.:	0.233	min.:	0.117
max.:	812.888	max.:	20227.9
mean value:	48.774	mean value:	418.910
median:	25.529	median:	50.879
standard deviation:	98.897	standard deviation:	2124.540
variance:	9889.273	variance:	4563270.24

If the *dU90* values are split according to the frequencies used and compared to the *nr of measurement*, a diagram like in *Figure 28* is obtained. However, this representation is not ideal due to the high outlier values, as the lower area of the diagram is thus hardly meaningful. In principle, such high outliers are outside the tolerance limit and are therefore assumed to be a mismeasurement. A closer look at these faulty measurements did not reveal any pattern, i.e., these errors are not exclusively found in the same electrode circuits

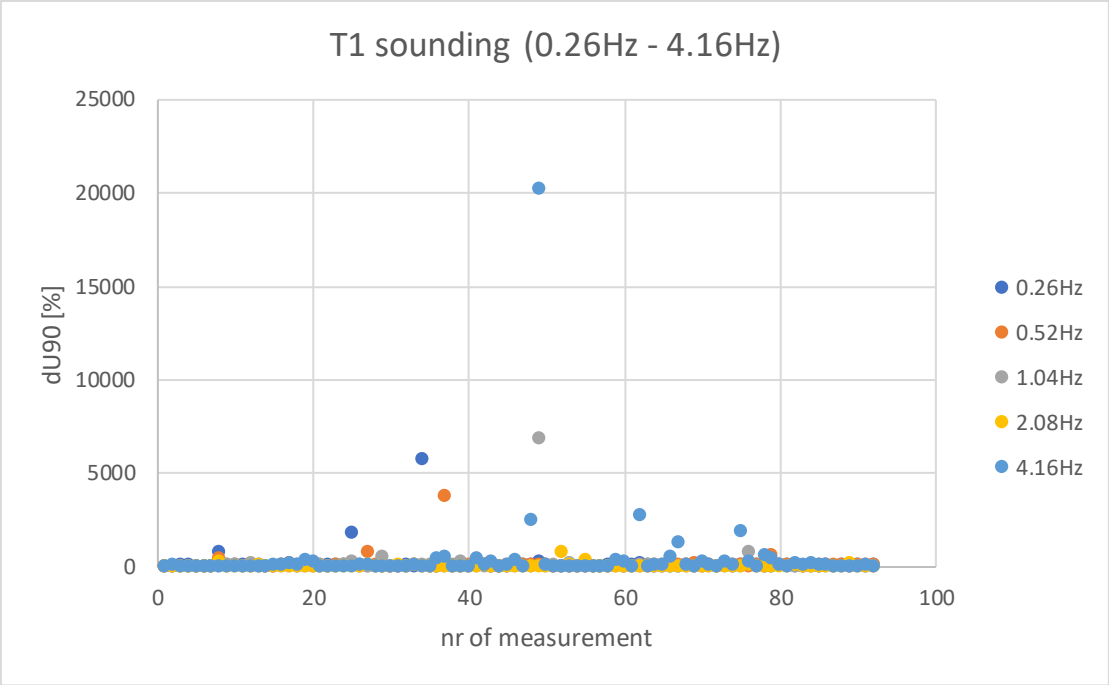

Figure 28: Shows the cross plot of measurement-series T1 between the nr of measurement (1-92) on the x-axis and the corresponding dU90 values on the y-axis split according to measurement frequency.

Table 10 shows these extreme outliers and the corresponding electrode circuit with *A*, *B*, *M* and *N*. The occurrence of such high *dU90* values does not seem to follow any particular pattern. The measurement with the frequency 2.08Hz once did not produce any value at all, whereas the measurement with 4.16Hz recorded five significantly increased *dU90* values.

Table 10: Intersection of the measurement of T1 with strongly increased dU90 for all measuring frequencies used (0.26Hz - 4.16Hz). The colour highlighting of the frequency column correlates with the colouring of Figure 28 and is intended to facilitate an overview of the data.

dU90	U90	phi	A	B	M	N	f
%	mV	mrad					Hz
1807.41	-0.00164	-0.084	**1**	**22**	**8**	**15**	0.26
5735.97	-0.00261	-0.052	**2**	**8**	**4**	**6**	0.26
3802.61	-0.00034	-0.007	**11**	**17**	**13**	**15**	0.52
6863.36	0.00066	0.003	**6**	**24**	**12**	**18**	1.04
-	-	-	**19**	**22**	**20**	**21**	2.08
2519.96	-0.0093	-0.44	**1**	**19**	**7**	**13**	4.16
20227.9	-0.0006	-0.029	**6**	**24**	**12**	**18**	4.16
2777.82	0.0146	0.269	**15**	**21**	**17**	**19**	4.16
1279.71	-0.00116	-0.032	**14**	**23**	**17**	**20**	4.16
1886.35	-0.00353	-0.103	**8**	**17**	**11**	**14**	4.16

To make *Figure 28* a little more meaningful, all outliers >1000% from *Table 10* were removed and the crossplot was generated again, *Figure 29*. One can clearly see how many values are generally above 100% and also that many of the remaining values still have an increased *dU90* value although they are below 100%.

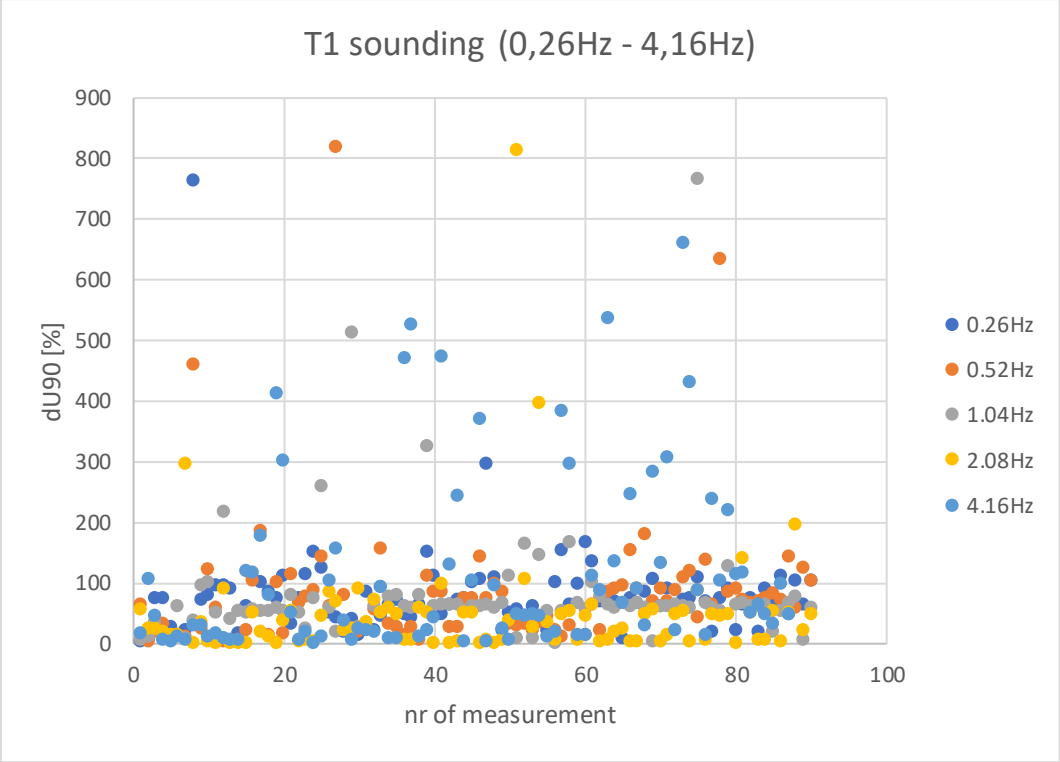

Figure 29: Shows the cross plot of measurement-series T1 between the nr of measurement on the x-axis and the corresponding dU90 on the y-axis split according to measurement frequency without all values above 1000%.

Figure 29 shows the *dU90* values of the five measurement frequencies used against the nr of the measurements. It can be seen that some *dU90*values are still above 100%. With error values above 100%, there appears to be no traceability. For this reason, all *dU90* above 100% were removed in the next step. On the one hand, this is to show the distribution of values below 100%, as these can be considered reliable values. On the other hand, it also shows how many measurements have too large an error value to be valid. *Figures 28* and *Figure 29* show the data clouds to get a general overview of the entire data set. The primary aim is to show the general range of values and the outliers. For this reason, the *dU90* values above 100% are filtered out in the next step. Since the values <100% are considered credible, a detailed presentation in the form of split diagrams was also chosen (*Figure 30*). This makes it easier to see the course of the individual measurement frequencies. A clear trend cannot be established, but in all frequencies, there is a strong fluctuation of the *dU90*, this oscillation is especially pronounced at 2.08Hz. In contrast, 1.04Hz shows comparatively little fluctuation and partly constant value ranges for *dU90* in the range above 50%. However, many gaps of the removed *dU90*

>100% can be seen in the diagrams of *Figure 30*. The resulting relatively large loss of measurement data must be taken into account.

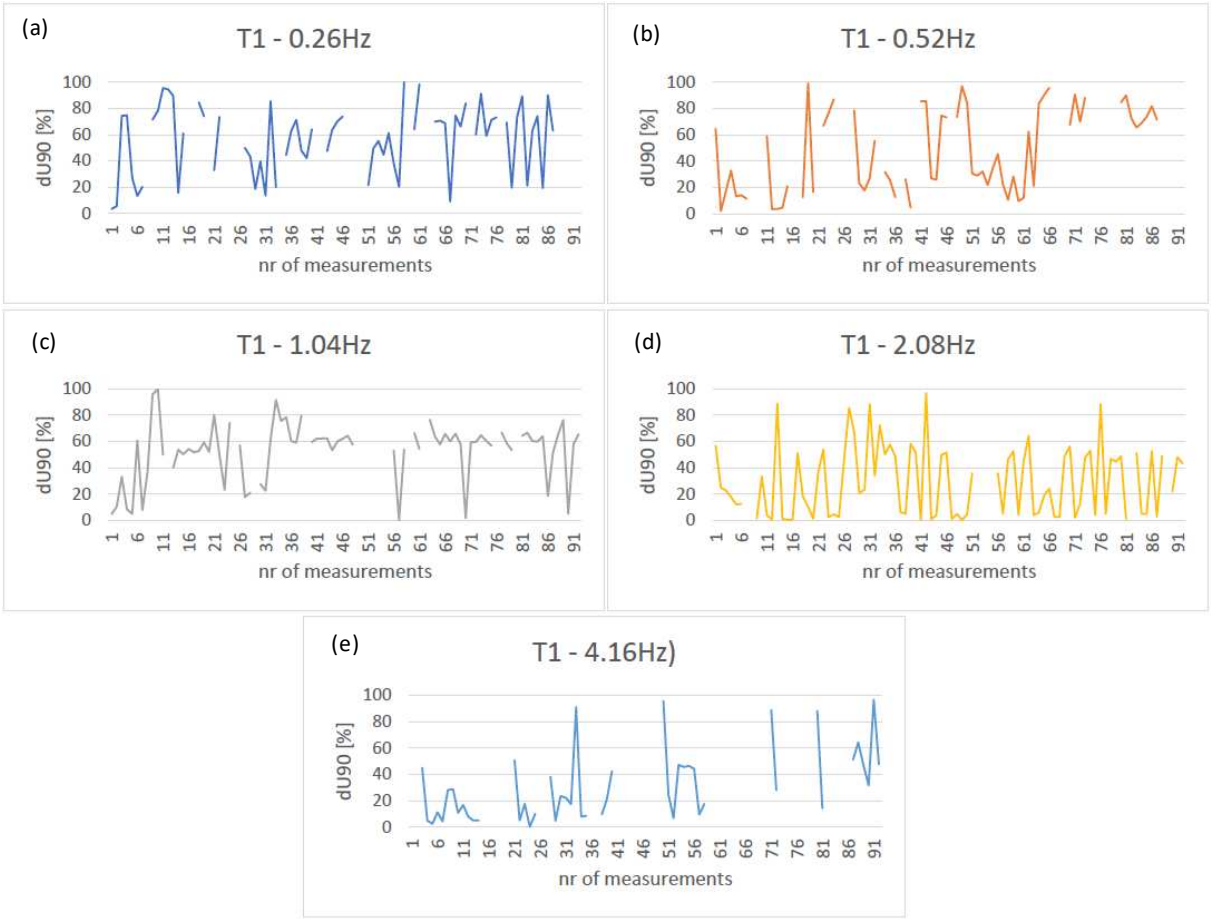

Figure 30: Split diagrams of the measurement-series T1 for the following measurement frequencies: (a) 0.26Hz, (b) 0.52Hz, (c) 1.04Hz, (d) 2.08Hz and (e) 4.16Hz.

Even when taking a closer look at the measured values >100%, no trend can be detected with regard to a certain switching of electrodes *A*, *B*, *M* and *N*. After this filtering of the *dU90* values, a look must be taken at the number of remaining measurements that are considered valid. *Table 11* lists the remaining valid measurements for the respective frequencies and the original number of measurements.

Table 11: Listing of the number of valid measurements of T1, also shown as a percentage, as well as the original number of measurements before data filtering.

	0.26Hz	0.52Hz	1.04Hz	2.08Hz	4.16Hz
remaining number of measurements	68	72	80	85	56
original number of measurements	92				
procentage of remaining measurements	73.91%	78.26%	86.96%	92.39%	60.87%

At a measuring frequency of 4.16Hz, approximately 60% of the measurements carried out are classified as valid. Also, at 0.26Hz, with almost 74% correct measurements occurred. For example, although at the measurement frequency of 2.08Hz the percentage of valid measurements is relatively high at 92.39%, it must still be remembered that the *dU90* value is very high.

Table 12: Statistical evaluation of the filtered data <100% of the measuring frequency 2.08Hz for T1.

2.08Hz dU90 [%]	
min:	0.233
max:	96.811
mean value:	29.304
median:	23.303
s.d.:	26.345
variance:	702.347

Table 12 lists the statistical evaluation of the filtered data with *dU90* <100% for the measurements with frequency 2.08Hz for *T1*. The mean value of 29.30% is a high error value for a measurement and reduces the quality of these measurements considered valid.

Compared to *Table 9*, the statistical values of the 2.08Hz measurement shown in *Table 12* have improved, but they are still very elevated and do not indicate good measurement quality.

7.1.3. Detailed analysis of measurement-series T2

The laboratory measurement *T2* has the same measurement setup as measurement *T1*, but it was carried out with a Dipole-Dipole configuration. Due to the different measurement configuration, this measurement *T2* is highlighted again, while the data of the remaining laboratory measurements can be found in the *electronic Appendix*. When looking at *Table 13*, a similar distribution of data as in *Table 9* from measurement *T1* is noticeable. The mean value is extremely high at all frequencies except 0.52Hz and 2.08Hz, and even at the two frequencies mentioned, the mean value is unacceptably high for an error indicator. The standard deviation shows a wide range of scatter in all frequencies, whereby these scatterings are clearly stronger at the measurement frequencies with increased mean value.

Table 13: Listing of the statistical evaluation of the dU90 value for measurement T2, split into the induvial measurement frequencies of Table 7.

0.26Hz dU90 [%]		0.52Hz dU90 [%]		1.04Hz dU90 [%]	
min.:	1.205	min.:	2.354	min.:	1.222
max.:	28868.77	max.:	1474.71	max.:	2445.56
mean value:	478.068	mean value:	94.251	mean value.	129.330
median:	35.727	median:	57.509	median:	47.877
standard deviation:	3066.700	standard deviation:	203.900	standard deviation:	315.031
variance:	9507996.3	variance:	42032.04	variance:	100335.3

2.08Hz dU90 [%]		4.16Hz dU90 [%]	
min.:	0.278	min.:	0.041
max.:	1446.3	max.:	8911.06
mean value:	85.906	mean value:	395.520
median:	40.4115	median:	66.348
standard deviation:	190.645	standard deviation:	1201.171
variance:	36745.043	variance:	1458666.76

Figure 31 shows the sounding of measurement *T2*, where all frequencies from 0.26Hz to 4.16Hz were measured. The *dU90* value is plotted against the *nr of measurement*. The high outlier values are very obvious, which make the remaining measured values difficult to recognise due to the resulting scaling. As with the analysis of measurement *T1*, these high values are also considered to be erroneous measurements in this evaluation.

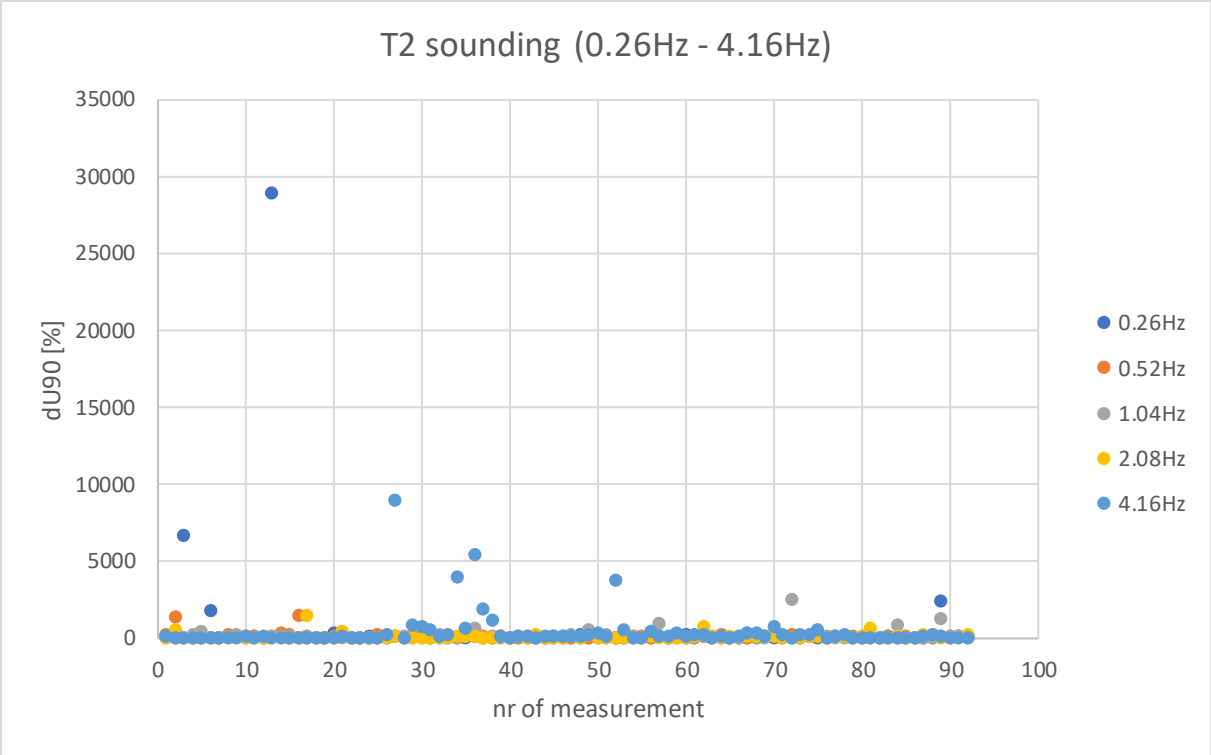

Figure 31: Shows the cross plot of measurement-series T1 between the nr of measurement (1-92) on the x-axis and the corresponding dU90 [%] values on the y-axis split according to measurement frequency.

Table 14 lists the outliers with values greater than 1000% *dU90*. When looking at the electrode columns *A*, *B*, *M* and *N*, a wide variety of electrodes are involved and therefore not a single defective electrode can be excluded as the cause for these measured values. Just like *Table 10* in the evaluation of *T1*, *Table 14* also shows that the measurements with the frequency 4.16Hz have the most outliers >1000%.

Table 14: Intersection of the measurements of T2 with strongly increased dU90 for all measuring frequencies used (0.26Hz-4.16Hz). The colour highlighting of the frequency column correlates with the colouring of Figure 31 and is intended to facilitate an overview of the data.

dU90	U90	phi	A	B	M	N	f
%	mV	mrad					Hz
6603.38	-0.00109	-0.05	**3**	**4**	**6**	**5**	0.26
2397.19	0.00321	0.05	**3**	**8**	**18**	**13**	0.26
1317.43	-0.00973	-0.339	**2**	**3**	**5**	**4**	0.52
1474.71	-0.01833	-0.629	**16**	**17**	**19**	**18**	0.52
2445.56	0.00163	0.02	**9**	**13**	**21**	**17**	1.04
1279.03	0.00376	0.059	**3**	**8**	**18**	**13**	1.04
1446.3	0.00822	0.261	**17**	**18**	**20**	**19**	2.08
8911.06	-0.00251	-0.153	**5**	**7**	**11**	**9**	4.16
3939.34	-0.00501	-0.319	**12**	**14**	**18**	**16**	4.16
5428.48	-0.00718	-0.428	**14**	**16**	**20**	**18**	4.16
1915.96	-0.00751	-0.453	**15**	**17**	**21**	**19**	4.16
1122.54	0.02843	1.811	**16**	**18**	**22**	**20**	4.16
3692.48	0.00698	0.64	**10**	**13**	**19**	**16**	4.16

The listed outliers in *Table 14* have been removed to improve the presentation of the data in *Figure 31*. The resulting *Figure 32* shows the distribution of the data slightly better, still including values above 100% *dU90*.

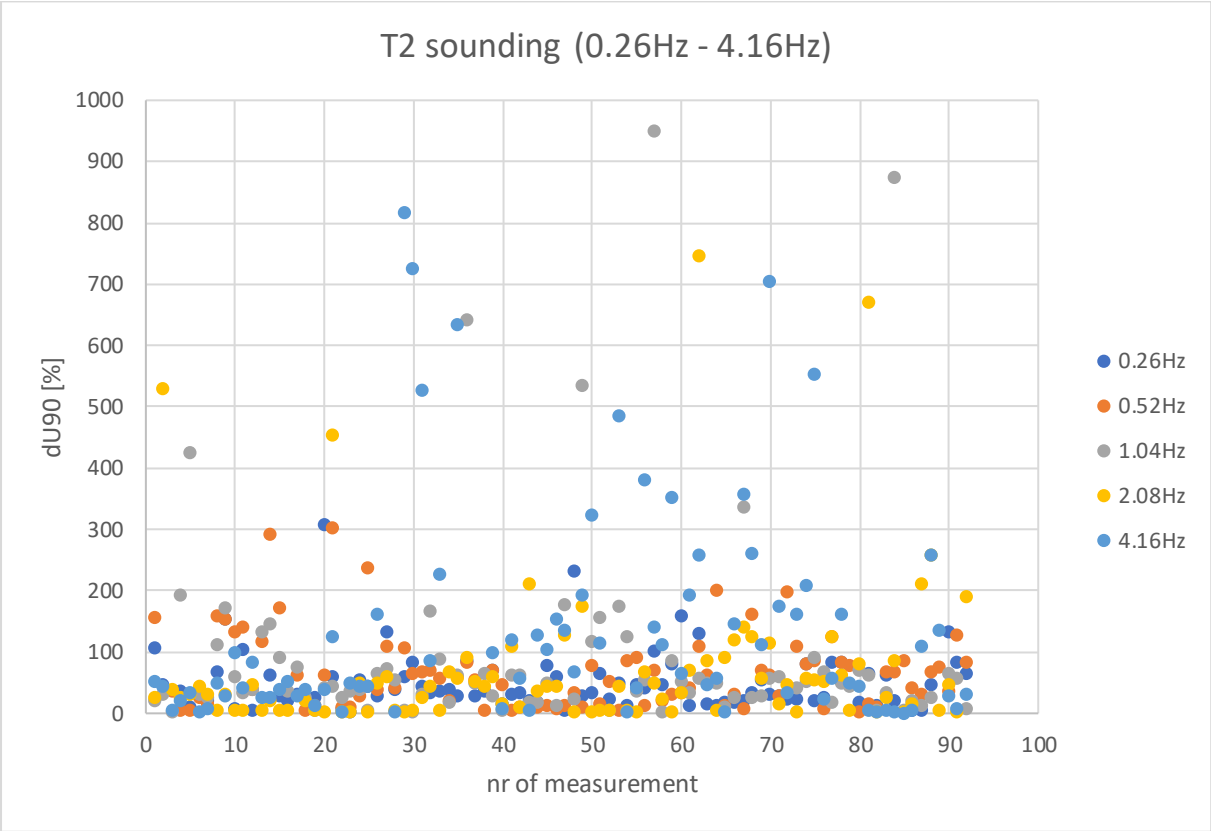

Figure 32: Shows the cross plot of measurement-series T2 between the nr of measurement on the x-axis and the corresponding dU90[%] on the y-axis split according to measurement frequency without all the values above 1000%.

Figure 32 shows that the measurement-series *T2* contains significantly more measurements with a *dU90* value greater than 100% compared to the measurement-series *T1* in *Figure 29*. These *dU90* values greater than 100% are also assumed to be erroneous measurements and therefore these are also removed in the next evaluation step. Through this further step, the values considered reliable can be displayed without the influence of erroneous interference values, *Figure 33*. For this purpose, the individual measurement frequencies were also displayed in individual diagrams and compared with each other. As with the *T1* measurement-series, no clear trend is discernible here, but there are also strong fluctuations in the *dU90* values. The measurement with 4.16Hz is clearly characterised by the deleted false measurements and shows large gaps in the data set. This large loss of data until the acceptable *dU90* values are reached has a significant impact on the validity of the results.

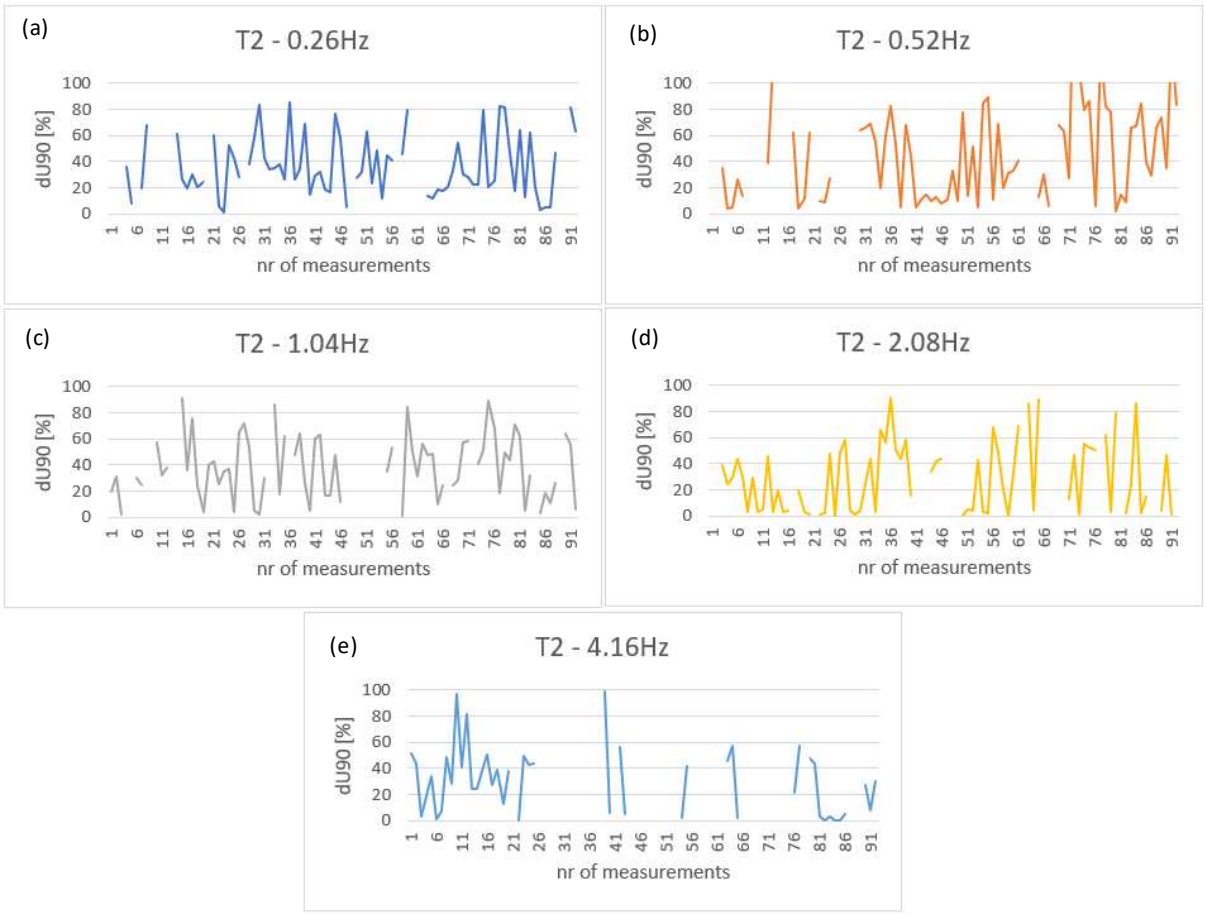

Figure 33: Split diagrams of the measurement-series T2 for the following measurement frequencies: (a) 0.26Hz, (b) 0.52Hz, (c) 1.04Hz, (d) 2.08Hz and (e) 4.16Hz.

These data losses are shown in *Table 15*: here the percentages of the remaining data with a *dU90* less than 100% are listed. It can be seen that, for example, the measuring frequency 4.16Hz performs comparatively poorly with only 57.61% of valid measured values. In contrast, the measuring frequency 0.26Hz shows the highest percentage of valid measured values with 84.78%. In comparison with the *T1* measurement-series, however, the values for the *T2* measurement-series are significantly lower.

Table 15: Listing of the number of valid measurements of T2, also shown as a percentage, as well as the original number of measurements before data filtering.

	0.26Hz	0.52Hz	1.04Hz	2.08Hz	4.16Hz
remaining number of measurements	78	73	72	75	53
original number of measurements	92				
procentage of remaining measurements	84.78%	79.35%	78.26%	81.52%	57.61%

7.1.4. Final statement on the laboratory measurements based on the example measurement-series T1 and T2 mentioned above

The detailed step-by-step presentation of the statistical evaluation for the laboratory measurement-series *T1* and *T2* shows how strongly error-prone these measurements are. Since the *dU90* values are regarded as an error indicator, statements about the quality of the measurement can be made by focussing the evaluation on them. For this purpose, the measurement-series *T1* and *T2* were used, as they do not differ from each other except for the measurement configuration. However, this shows that the number of *dU90* values greater than 100 is very high for both the Wenner and the Dipole-Dipole measurement configurations, which significantly reduces the validity and significance of the measurements. For this reason, the measurement-series for the fully filled test tank cannot be used for meaningful and valid theses.

After the measurement-series *T1* to *T5* have been carried out for the completely filled tank, the water in the tank was drained down to the inserted gravel layer. Directly afterwards, further series of measurements were carried out to document the drying process, listed in *Table 16*.

Table 16: List of measurement settings for measurement-series T6-T12 with half dry tank.

name	number of electrodes	configuration	frequency [Hz]	temp. tank [°C]	temp. room [°C]	conductivity water [µS/cm]
T6	25	Wenner	4.16Hz	18.9	21.3	349
T7	25	Wenner	4.16Hz	18.9	21.3	349
T8	25	Wenner	4.16Hz	18.9	21.3	349
T9	25	Wenner	4.16Hz	18.9	21.3	349
T10	25	Wenner	0.26Hz – 4.16Hz	18.9	21.3	349
T11	25	Dipole-Dipole	0.26Hz – 4.16Hz	18.9	21.0	356
T12	25	Wenner	0.26Hz – 4.16Hz	19.2	21.2	359

Measurements *T6* to *T9* are test measurements, these were carried out because there were problems with contact resistances being too high. For this measurement-series, no such detailed evaluation is carried out as for the measurement-series *T1* to *T5*, as the review of the measurement *T6* already revealed significantly more serious data gaps than for the measurement-series *T1* to *T5*. As shown, these gaps in the measurement-series *T1* to *T5* were mainly caused by too high *dU90* values, which were interpreted as incorrect measurements in the course of the evaluation. In contrast, the raw data of the measurement-series *T6* to *T12* show many gaps within the measurements, as the device was not able to measure a value at all. The extent of these data gaps is shown in *Table 17* for the four comparison measurements *T6* to *T9*, which were carried out with almost similar measurement settings.

Table 17: Shows the statistical evaluation of the dU90 values for measurements T6-T9. In addition, the number of measurements classified as valid is shown in relation to the total number of measurements.

T6		**T7**	
dU90 [%]		dU90 [%]	
max.:	2026.52	max.:	10784.70
min.:	0.004	min.:	0.019
mean value:	190.90	mean value:	245.00
standard deviation:	335.11	standard deviation:	1120.19
total number:	92	total number:	92
>100:	26	>100:	36
<0:	0	<0:	0
no measurements:	35	no measurements:	0
0-100:	**31**	0-100:	**56**

T8		**T9**	
dU90 [%]		dU90 [%]	
max.:	134392	max.:	4872.66
min.:	0.087	min.:	0.025
mean value:	1915.10	mean value:	198.58
standard deviation:	13984.76	standard deviation:	638.94
total number	92	total number:	92
>100	38	>100:	24
<0	0	<0:	0
no measurements	0	no measurements:	35
0-100	**54**	0-100:	**33**

When looking at *Table 17*, the significantly reduced number of measurements with a *dU90* between 0-100% is striking. *T7* and *T8* show a higher number of measurements with a *dU90* value between 0-100%, since the current *I* has been set to 0.001mA for these measurements. This was an attempt to improve the measurement quality, as the default setting of current *I* of 0.1mA was chosen for measurements *T6* and *T9*. This change in current means that there are no empty measurements, i.e., no measurements where the device does not match any measured value. However, despite this change, it was not possible to achieve a satisfactory number of measurements that are classified as valid. The 56 or 54 measurements that were interpreted as valid are only 60% of a total of 92 measurements and therefore 40% of the individual measurements that were carried out are to be regarded as invalid or faulty. As the measurements in the semi-dry state show significantly worse percentages of valid measurements, the laboratory measurements were not continued at this point, as no improvement of the measurement quality can be expected with ongoing drying process. Possible reasons for this poor measurement quality were found to be the too rapid drying out of the upper humus and sand layer as well as a possible corrosion of the electrodes, which lead to a reduction of

the conductivity in the semi-dry state. A possible corrosion of the electrodes cannot be ruled out, as the experimental setup was unused for several months.

Replacing the metal electrodes on the side of the tank would mean completely emptying and reinstalling the tank contents. This additional work is not related to the actual research question of this thesis, as the main focus is on the field measurements. For this reason, the laboratory measurements were not continued from this point onwards, as they were originally only considered as supporting investigations on a smaller scale.

8. Data Evaluation - field measurements

The evaluation of the field measurements is initially divided into the measurements from May 2021, which were carried out with the *Lippmann 4 point light 10W* measuring device, and the second measurement run from November 2021, which were carried out with the *Mangusta System MC 24/144E* measuring device as well as with the *Lippmann 4 point light 10W*.

Since a large number of measurements have been carried out, these are first examined statistically and then compared with regard to their inversion results in addition to the statistical results. The aim is, among other things, to find indications of the existence of the gas dome as a measurement target, as well as to compare the results of the November 2021 measurements in time-domain and frequency-domain with each other, since these were carried out along the same profile lines.

8.1. Statistical evaluations of the measurements May 2021

In May 2021, a total of 40 measurements were carried out, these were divided into a N-S and a W-E profile around a gas dome. The list of measurements including all settings is listed in the *Appendix A*. The designation of the measurements also includes the measurement date, however, for the sake of simplicity, only the final designation without the preceding date is mentioned below.

To avoid confusion due to the high number of measurements, the evaluation follows a strict scheme. Basically, the two profiles N-S and W-E are considered individually first. Within a profile, those measurements with the same measurement configurations but different electrode types are then compared with each other in order to be able to make statements about a preferred electrode type. Then the two measurement configurations used, Wenner and Dipole-Dipole, are compared in order to be able to discuss disadvantages and advantages.

8.1.1. North-South profile

The comparison of the *dU90* values along the N-S profile starts with the Wenner measurements *M1* to *M5* with non-polarisable electrodes and the Wenner measurements *M11* to *M15* with conventional electrodes. *Table 18* shows the statistical evaluations of the measurement-series *M1* to *M5*. Compared to the statistical results of the laboratory measurements, see *Table 13*, significantly more acceptable values were achieved here. In principle, the values for all frequencies used look very similar, with the exception of the higher maximum value for measurement *M4*. It is also noticeable that the median for the two higher-frequency measurements *M1* and *M2* is significantly lower than for measurements *M4* to *M5*. However, all these deviations are negligibly small and within acceptable limits.

Table 18: Listing of the statistical evaluation of the dU90 values for the measurements M1-M5, with Wenner configuration and non-polarisable electrodes.

M1 dU90 [%] - 4.16Hz		M2 dU90 [%] - 2.08Hz		M3 dU90 [%] - 1.04Hz	
min.:	0.013	min.:	0.004	min.:	0.016
max.:	4.995	max.:	4.985	max.:	4.991
mean value:	1.376	mean value:	1.055	mean value.	3.118
median:	0.840	median:	0.530	median:	3.899
standard deviation:	1.420	standard deviation:	1.280	standard deviation:	1.781
variance:	2.034	variance:	1.653	variance:	3.202

M4 dU90 [%] - 0.52Hz		M5 dU90 [%] - 0.26Hz	
min.:	0.082	min.:	0.169
max.:	8.638	max.:	4.997
mean value:	3.683	mean value:	4.043
median:	4.485	median:	4.431
standard deviation:	1.577	standard deviation:	1.111
variance:	2.509	variance:	1.246

In addition to the tabular listing of the data, graphical representations were also created, as these allow for a better visualisation of the data, as well as for a visually easier comparison. *Figure 34* shows the compilation of the *dU90* values against the *nr of measurement*.

In *Figure 34 (a)* all plots of the 5 measurement frequencies for the *dU90* values against the *nr of measurement* for the measurements *M1* to *M5* are shown simultaneously. The measurement frequencies are listed in colour in the adjacent legend. When looking at *Figure 34 (a)*, the outlier value of *M4*, measured at 0.52Hz, immediately catches the eye. All other *dU90* values do not exceed the 5% mark, as this has been set as a threshold value in the default settings. With the outlier value of *M4*, the measuring device does not seem to have managed to fall below the 5% mark despite the repeat measurements carried out at each measuring step. The plots for the two higher frequency measurements *M1* and *M2* with 4.16Hz and 2.08Hz look comparatively similar compared to the other plots. The plots show sections with higher *dU90* values, which in turn are followed by areas with lower *dU90* values. The plots of *M3* and *M4* with 1.04Hz and 0.52Hz also show a similar pattern, although an outlier value can be seen in *M4* that exceeds even the 8% mark. However, compared to the plots of *M1* and *M2*, these plots show more pronounced jumps between higher and lower *dU90*, seemingly after each individual measurement, while for *M1* and *M2* these jumps are not as pronounced. Measurement *M5* with the lowest measurement frequency of 0.26Hz shows a completely different picture: here it appears as if the basic value of *dU90* is almost continuously at the 5% mark, with some lower values. The assumption that for *M3*, but especially also for *M4* and *M5*, the basic value of *dU90* is close to the 5% mark can also be confirmed by a cross-check with the values from *Table 18*: these

measurements show a median of 3.899% for *M3* and a median above 4% for the measurements of *M4* and *M5*. This means that 50% of the measured values are above this median value. This also explains the different characteristics of the plots compared to the measurements of *M1* and *M2*, which both have a median of less than 1.

In general, the statistical evaluations and the resulting plots show that the measurements are of good quality and the *dU90* values are within the tolerable range.

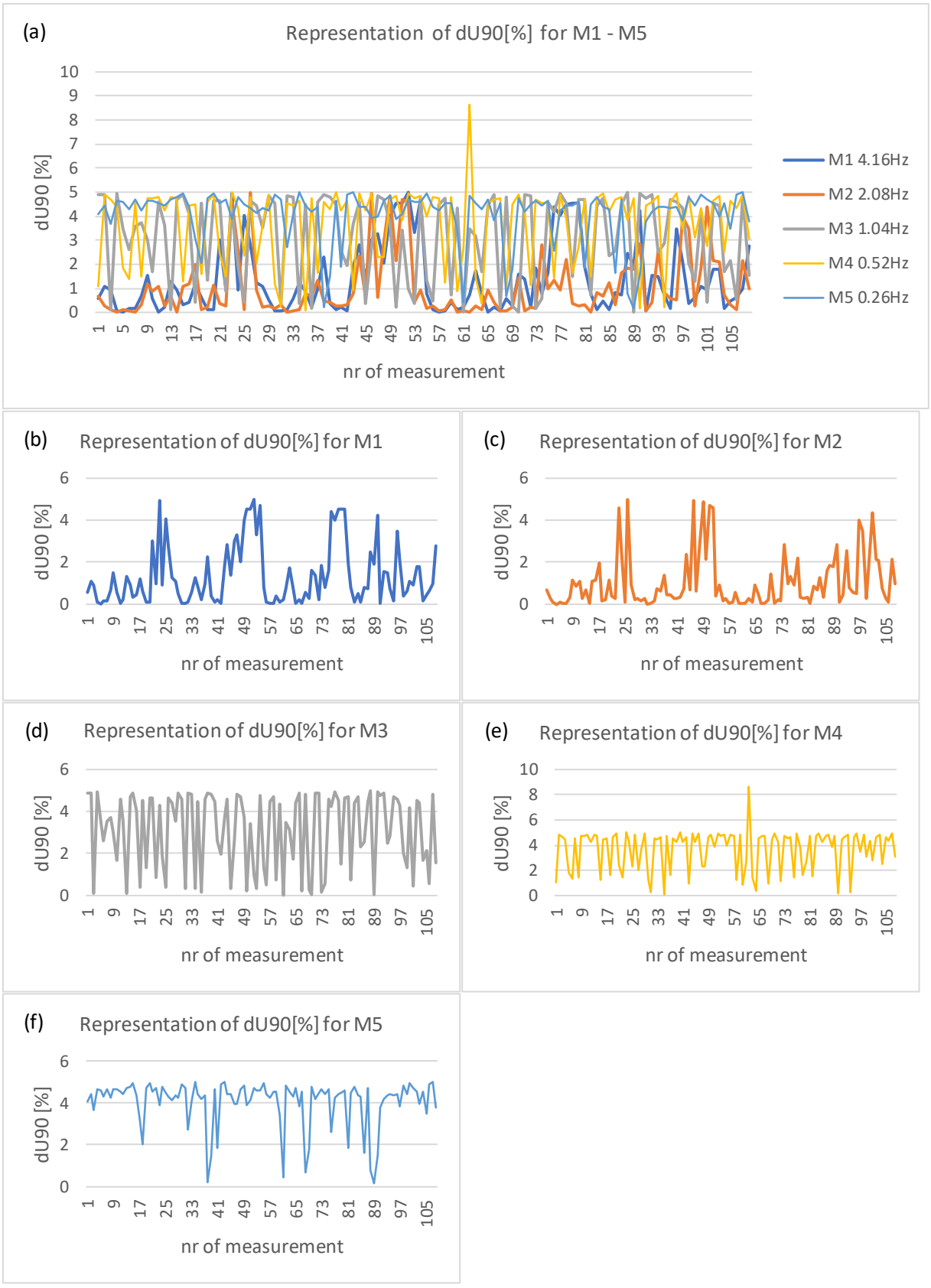

Figure 34: (a) all plots of dU90 values against nr of measurement for all five frequencies used. (b) for the measurement frequency 4.16Hz (c) for the measurement frequency 2.08Hz (d) for the measurement frequency 1.04Hz (e) for the measurement frequency 0.52Hz (f) for the measurement frequency 0.26Hz.

Another way to obtain additional information regarding the *dU90* value is to plot these values against the pseudo-depth *m* of the measurements. To keep the figure clearer, only the high-frequency measurement *M1* is shown together with the low-frequency measurement *M5*, *Figure 35*.

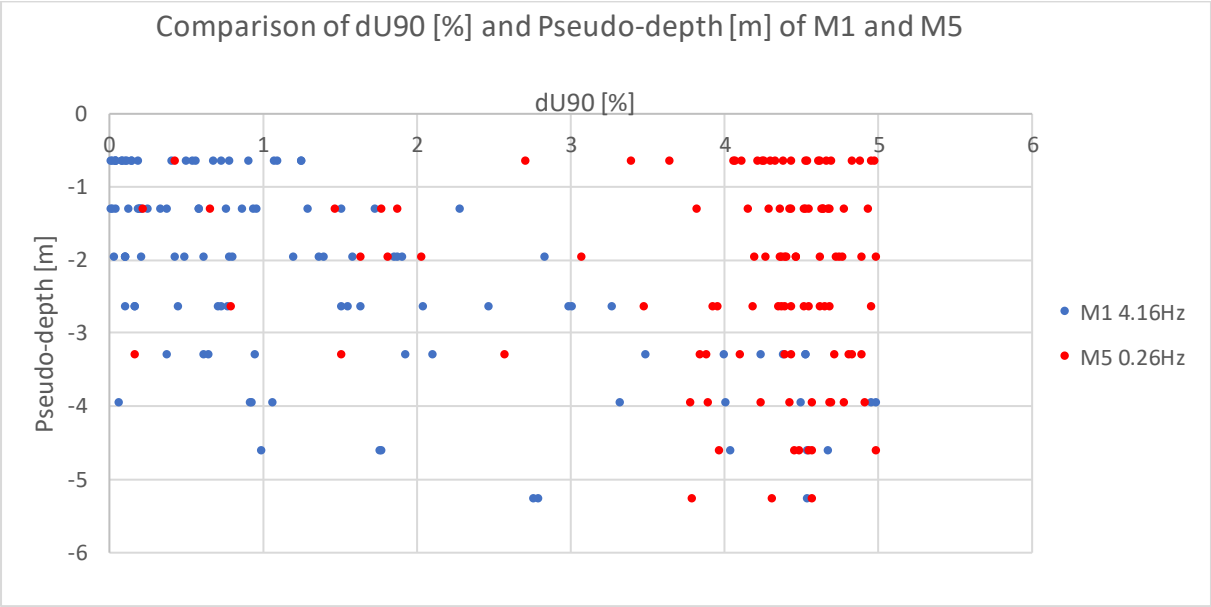

Figure 35: Shows the correlation of the dU90 values and the pseudo-depth for the two measurements M1 with 4.16Hz and M5 with 0.26Hz.

One can clearly see that the higher frequency measurement *M1* with 4.16Hz has lower *dU90* values along the entire pseudo-depth. However, it can be seen that with increasing pseudo-depth there is a shift of the data points towards higher *dU90* values.

Measurement *M5* at 0.52Hz, however, shows a general trend towards higher *dU90*, as has already been determined in the statistical evaluations, but these *dU90* values are generally found along the entire pseudo-depth. Only in areas of lower pseudo-depth are some data points associated with lower *dU90* values.

Measurements *M11-M15* can be used as direct comparisons to the *M1-M5* measurement range. These were also carried out with Wenner configuration, but with classic metal electrodes. The aim of this comparison is to show the influence of the different electrode types with the same measurement configuration on the measured values. The statistical evaluation of the *dU90* values is listed in *Table 19*. A comparison with *Table 18* reveals very similar aspects: again, the two higher frequency measurements *M11* and *M12* show the lowest median in contrast to the other measurements *M13* to *M15*. The maximum value of *M13* slightly exceeds the 5% mark with 6.272%, as does measurement *M14*. In general, however, at first glance these statistical values are very similar to those of the measurement-series *M1* to *M5*.

Table 19: Listing of the statistical evaluation of the dU90 values for the measurements M11-M15, with Wenner configuration and metal electrodes.

M11 dU90 [%] - 4.16Hz		M12 dU90 [%] - 2.08Hz		M13 dU90 [%] - 1.04Hz	
min.:	0.018	min.:	0.012	min.:	0.000
max.:	4.813	max.:	4.994	max.:	6.272
mean value:	1.073	mean value:	1.311	mean value:	2.586
median:	0.737	median:	0.923	median:	2.572
standard deviation:	1.146	standard deviation:	1.208	standard deviation:	1.956
variance:	1.325	variance:	1.472	variance:	3.860

M14 dU90 [%] - 0.52Hz		M15 dU90 [%] - 0.26Hz	
min.:	0.156	min.:	0.193
max.:	5.597	max.:	4.995
mean value:	3.854	mean value:	4.035
median:	4.619	median:	4.394
standard deviation:	1.488	standard deviation:	1.057
variance:	2.235	variance:	1.129

Figure 36 shows plots between the *dU90* values of the respective measurement frequencies plotted against the *nr of measurement*. In *Figure 36 (a)* again all plots are shown on top of each other. The outlier value of *M13* with 1.04Hz stands out. This is at the same position of the *nr of measurement* as in measurements *M1* to *M5*, only the outlier was in measurement *M4* with 0.52Hz. *M11* and *M12* show a similar pattern to *M1* and *M2*, again explained by the low median value of less than 1%, which means that 50% of the data are below and the remaining 50% of the data are above the median. Therefore, it can also be seen in the diagrams that a large part of the data density is found in the lower *dU90* values.

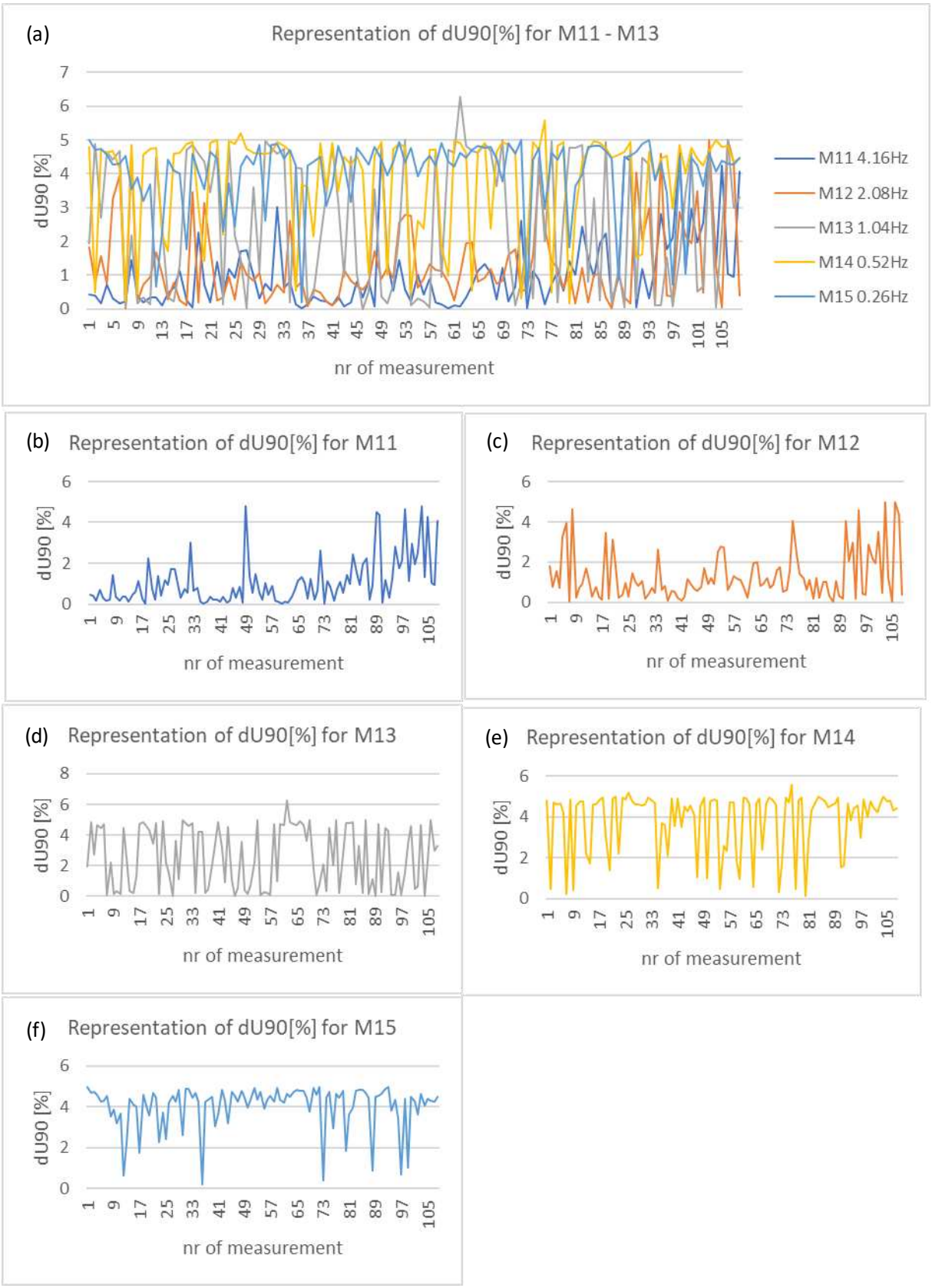

Figure 36: (a) all plots of dU90 values against nr of measurement for all five measurement frequencies used. (b) for the measurement frequency 4.16Hz (c) for the measurement frequency 2.08Hz (d) for the measurement frequency 1.04Hz (e) for the measurement frequency 0.52Hz (f) for the measurement frequency 0.26Hz.

The opposite phenomenon can be seen in the measurements *M14* and *M15*, where the median has also assumed a significantly higher value. This is then reflected in the plots, where 50% of the data therefore show relatively high *dU90* values.

In addition, a plot was made showing the correlation between the pseudo-depth and the *dU90* values, *Figure 37*. Again, only the high-frequency measurement *M11* with 4.16Hz and *M15* with 0.26Hz was used. The picture is similar to that of the measurement-series *M1* to *M5*: the high-frequency measurement *M11* shows significantly lower *dU90* values, even at greater pseudo-depths. Although there are individual data points that lie in the range of higher *dU90* values, the majority remain below the 1% mark, even at greater pseudo-depths. The opposite picture is shown by the *M15*, where the majority of the data lies between 4-5% *dU90*, even in shallow pseudo-depths where a generally higher amount of data is present.

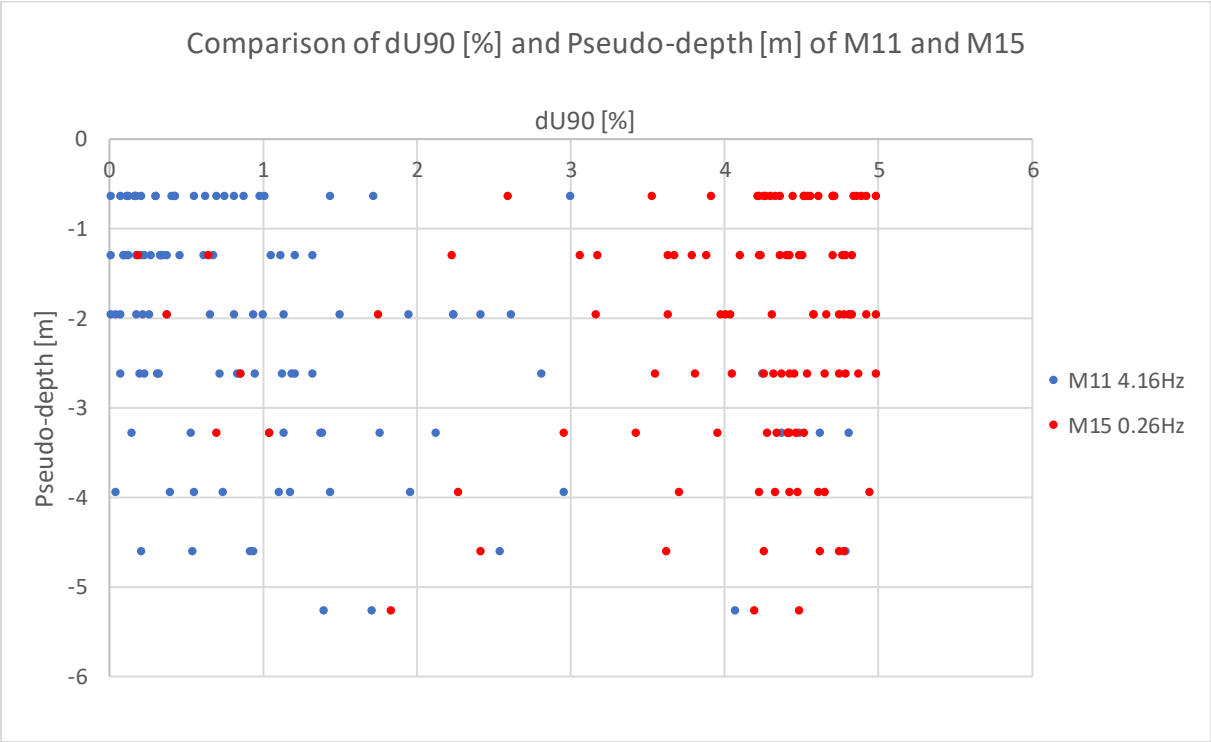

Figure 37: Shows the correlation of the dU90 values and the pseudo-depth for the two measurements M11 with 4.16Hz and M15 with 0.26Hz.

This type of comparison between the two measurement-series *M1-M5* and *M11-M15* does not yet allow a clear statement regarding a preference of an electrode type. For this reason, another comparison test was made: For this purpose, the *dU90* was no longer considered, as this can be classified as sufficiently good for the two measurement-series mentioned and therefore testifies to a good measurement quality. Therefore, the focus was specifically on a parameter that is supposed to

represent the IP effect. This parameter is the phase angle phi, which is given in *mrad* and defines as shown in *Equation (18)* (Lippmann, 2014):

(18)

$$\varphi\ [mrad] = \frac{U_{90}}{U} * 1000$$

U_{90}: Measured voltage (phase-shifted component) in mV

In order to be able to make a better statement regarding the electrodes used and the measurement configurations, a further focus was placed on the distribution of the *phi* values. For this purpose, crossplots were created for the two measurement-series *M1-M5* and for *M11-M15*. The individual measurement frequencies were plotted against the lowest measurement frequency of 0.26Hz. Looking at both plots, *Figure 38 (a)* and *(b)*, a basically similar trend is noticeable: in both plots, the higher frequency measurements show lower data values, see relevant area on the y-axis. The difference between the different measurement frequencies is clearly visible, while the measurement with 4.16Hz shows data points between 15 and less than 30mrad, the measurement with 0.52Hz shows points between greater than 20 and up to 40mrad, *Figure 38 (a)* using the non-polarisable electrodes. *Figure 38 (b)* shows similar ranges of values, although these are influenced by the generally larger scatter and outlier values. *Figure 38 (b)* shows the same series of measurements but using the classic metallic electrodes. In this plot, one can see a clear scattering of the data points compared to *Figure 38 (a)*. The data points show some scatter in both plots, resulting in a cloudy distribution. In order to be able to make a more differentiated statement, regression lines were generated for the individual data pools. As a measure of the quality of the model fit, a quantity is used which is based on this scatter decomposition, namely the so-called coefficient of determination R^2. This indicates just the proportion of the total scatter of y_i that is explained by the regression of *Y* to *X* and is thus the quotient of the explained and total dispersion. The coefficient of determination takes on values between zero and one. A value of zero means that the explained dispersion is equal to zero and thus the model is conceivably bad (Fahrmeier et al., 2016). Looking at the R^2 values in *Figure 38 (a)* and *(b)*, it can generally be seen that the R^2 values in both plots vary to some extent, but are in a similar size range. *Figure 38 (b)* shows generally lower values for R^2. Compared to this, *Figure 38 (a)* shows significantly better R^2 values, as these are closer to 1, which testify to a better validity of the regression model.

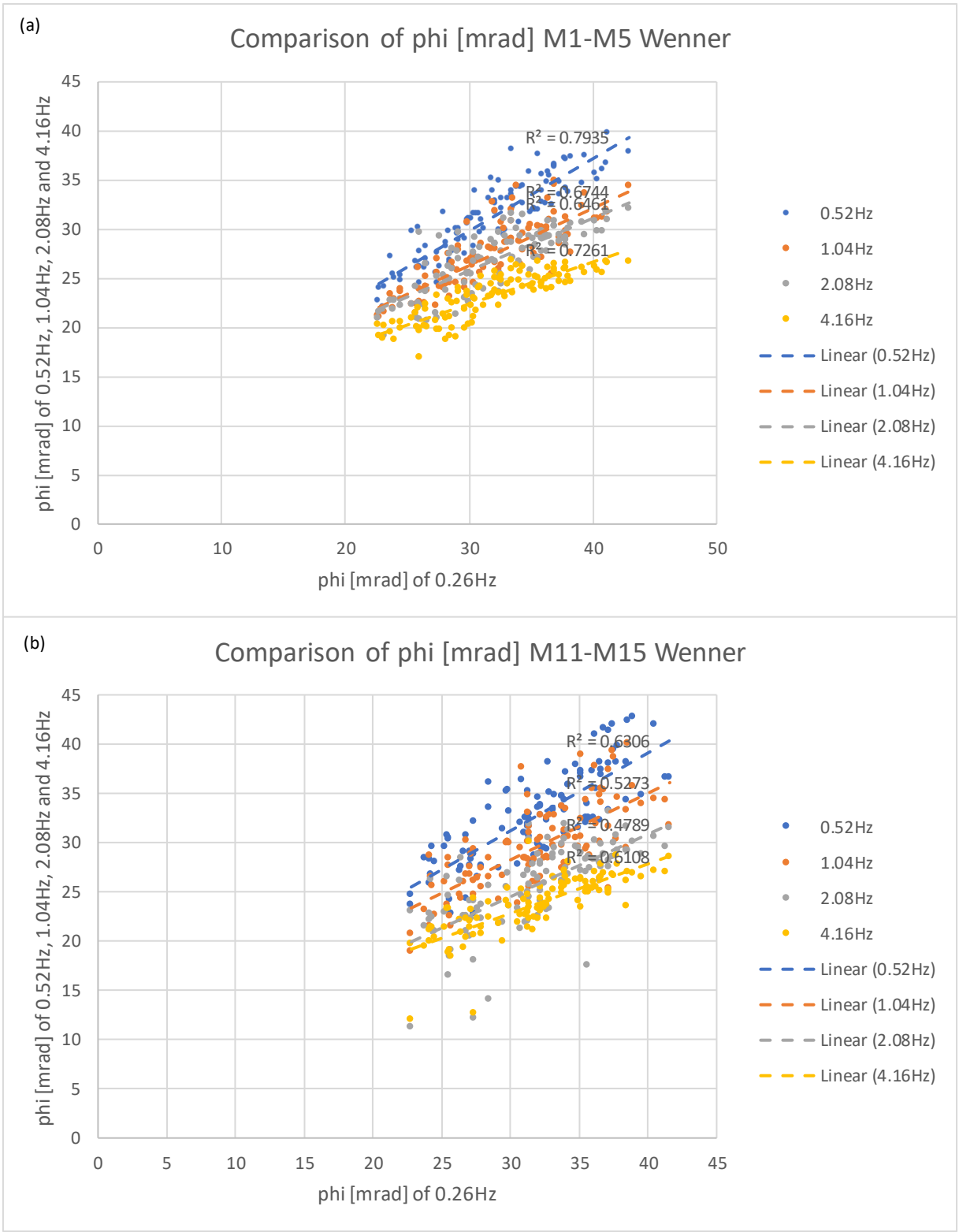

Figure 38: (a) Crossplot between the measurement at 0.26Hz against all other measurements at frequencies 4.16Hz, 2.08Hz, 1.04Hz and 0.52Hz for the measurement-series M1-M5 using non-polarisable electrodes and with Wenner configuration. (b) Crossplot between the measurement with 0.26Hz against all other measurements with the frequencies 4.16Hz, 2.08Hz, 1.04Hz and 0.52Hz for the measurement-series M11-M15 using non steel electrodes and with Wenner configuration.

In *Figure 38 (b)* the R^2 values are somewhat lower. Within a measurement-series, for example *M1* to *M5* in *Figure 38 (a)*, a gradation of the R^2 values can be seen: the measurement with 0.52Hz has the highest value, followed by the measurement with 4.16Hz, with 1.04Hz and the measurement with 2.08Hz has the lowest value. This change in the R^2 values can also be seen in *Figure 38 (b)* in the same order of gradation. This means that the scatter of those measurements with a higher R^2 value can be better explained. When comparing these two plots, it is clear that the measurements made using non-polarisable electrodes have a lower scatter and a generally higher coefficient of determination R^2. This comparison confirms the thesis assumed from the literature that for IP measurements the non-polarisable electrodes are advantageous, as unwanted polarisation effects can be reduced and thus a lower scatter and greater stability of the measured *phi* values can be achieved.

Along the N-S profile, the same series of measurements were also carried out in Dipole-Dipole configuration. The basic idea behind this was to make optimal use of the advantages and disadvantages of both the Wenner and Dipole-Dipole measurements. Therefore, comparative measurements were also taken with the Dipole-Dipole configuration.

Starting with a statistical evaluation of the *dU90* values to get a general overview of the data quality. *Table 20* shows this evaluation for the measurement-series *T6-T8*, which was carried out in Dipole-Dipole configuration with non-polarisable electrodes.

Table 20: Listing of the statistical evaluation of the dU90 values for the measurements M6-M10, with Dipole-Dipole configuration and non-polarisable electrodes.

M6 dU90 [%] - 4.16Hz		M7 dU90 [%] - 2.08Hz		M8 dU90 [%] - 1.04Hz	
min.:	0.009	min.:	0.074	min.:	0.018
max.:	75.6	max.:	71.54	max.:	75.63
mean value:	4.107	mean value:	3.224	mean value:	4.241
median:	3.02	median:	1.603	median:	4.314
standard deviation:	7.771	standard deviation:	7.132	standard deviation:	7.236
variance:	60.95	variance:	51.34	variance:	52.85

M9 dU90 [%] - 0.52Hz		M10 dU90 [%] - 0.26Hz	
min.:	0.264	min.:	0.051
max.:	216.1	max.:	30.44
mean value:	6.022	mean value:	4.234
median:	4.593	median:	4.422
standard deviation:	20.43	standard deviation:	3.067
variance:	421.2	variance:	9.493

The strongly increased maximum value is clearly noticeable. Compared to this, however, the mean value is in an acceptable range, although it is noticeably higher than in the measurement-series with

Wenner configuration, see *Tables 19* and *18*. This also results in an increased variance. Measurement *M9* shows an enormously high maximum value of 216.1% for *dU90*. However, the median in all five measurements of this series is relatively low, considering the clearly increased maximum values. This means that at least 50% of the data is below the median and since this is low, at least 50% of the data is in an acceptable range for *dU90* values. Compared to the *dU90* values of the Wenner configurations, where the high-frequency measurements show relatively low median values of 4.16Hz and 2.08Hz, these are also increased in the measurement-series with Dipole-Dipole configuration.

Figure 39 (a) to *(f)* shows the *dU90* values of the measurement-series *M6-M10* against the *nr of measurement*. *Figure 39 (a)* is very different from the comparable diagrams of the measurement-series with Wenner configuration *M1-M5* and *M11-M15*. The larger peak at *nr of measurement* 69 and the smaller one at 97 are particularly striking and distort the general picture. In the individual representation it becomes clear that all measurements have at least one of the two prominent peaks. The high maximum value of *M9* was already shown in *Table 20* by the statistical analysis and is also clearly visible in the diagrams. *Figure 39 (a)* is a compilation of the other graphs and shows stronger fluctuations with increasing *nr of measurement* compared to lower *nr of measurements*. This seems to be related to the increasing depth of investigation. The more prominent peak at *nr of measurement* 70 involves the following electrodes: 1, 5, 13 and 9, where 1 and 5 are current inducing electrodes and 13 and 9 are potential electrodes. The target gas dome is placed approximately at electrode 13 and may have some influence leading to these outliers in the *dU90* values. Apart from the two clear peaks, the other values are in a relatively acceptable range.

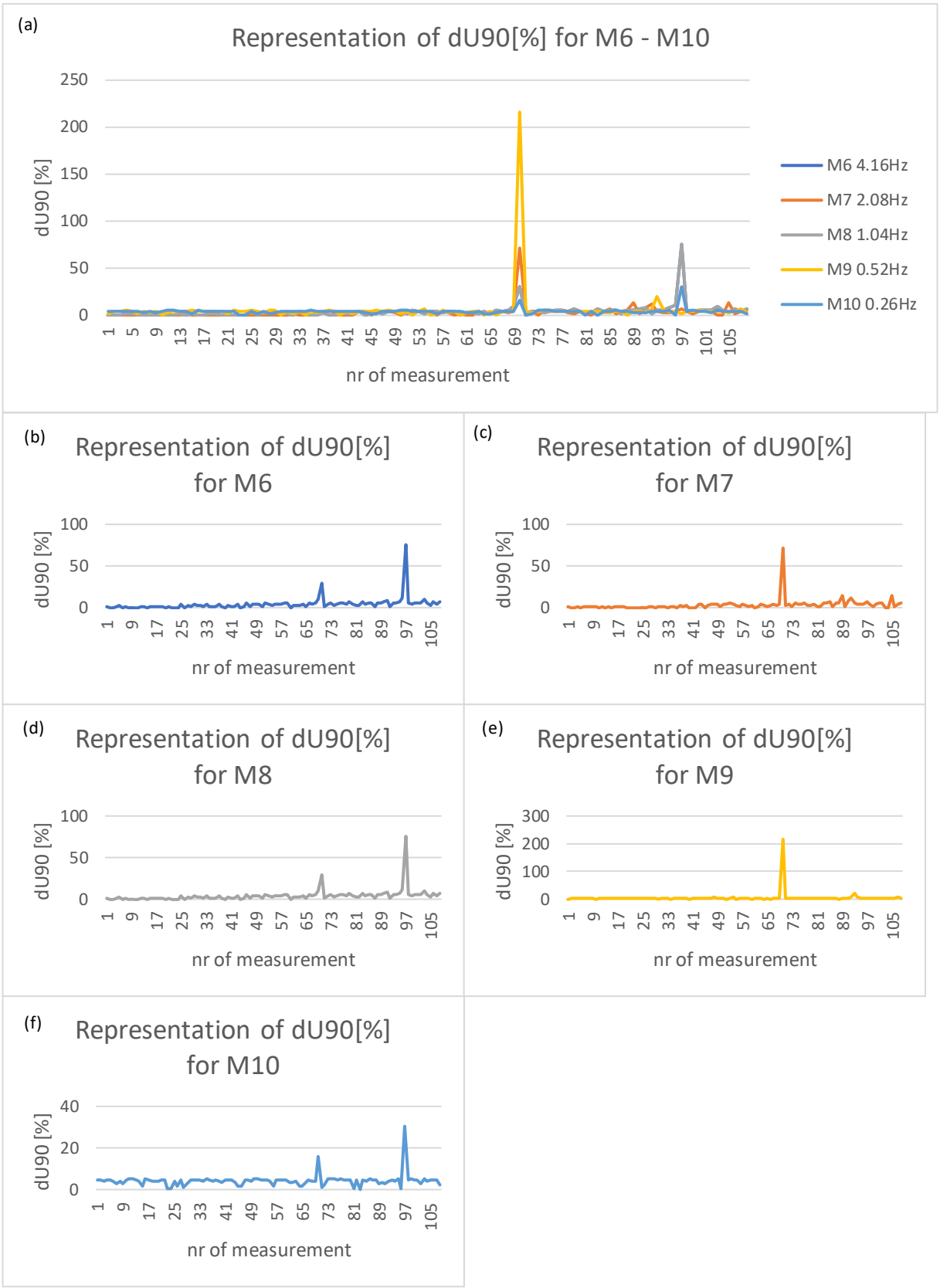

Figure 39: (a) all plots of dU90 values against nr of measurement for all five measurement frequencies used. (b) for the measurement frequency 4.16Hz (c) for the measurement frequency 2.08Hz (d) for the measurement frequency 1.04Hz (e) for the measurement frequency 0.52Hz (f) for the measurement frequency 0.26Hz.

Looking at the dependence of the *dU90* values on the pseudo-depth, it is noticeable that the outliers of the high-frequency measurement *M6* with 4.16Hz are in the higher value range than those of the measurement *M10*, *Figure 40*. For the data points in low pseudo-depth, the values of the two comparison measurements *M6* and *M10* overlap. In greater pseudo-depths the data points of the *M6* measurement with 4.16Hz occur significantly more often in the higher value range compared to those of measurement *M10*. Thus, the data in this comparison show a different picture than in the measurement-series *M1-M5* and *M11-M15*, which were measured in Wenner configuration.

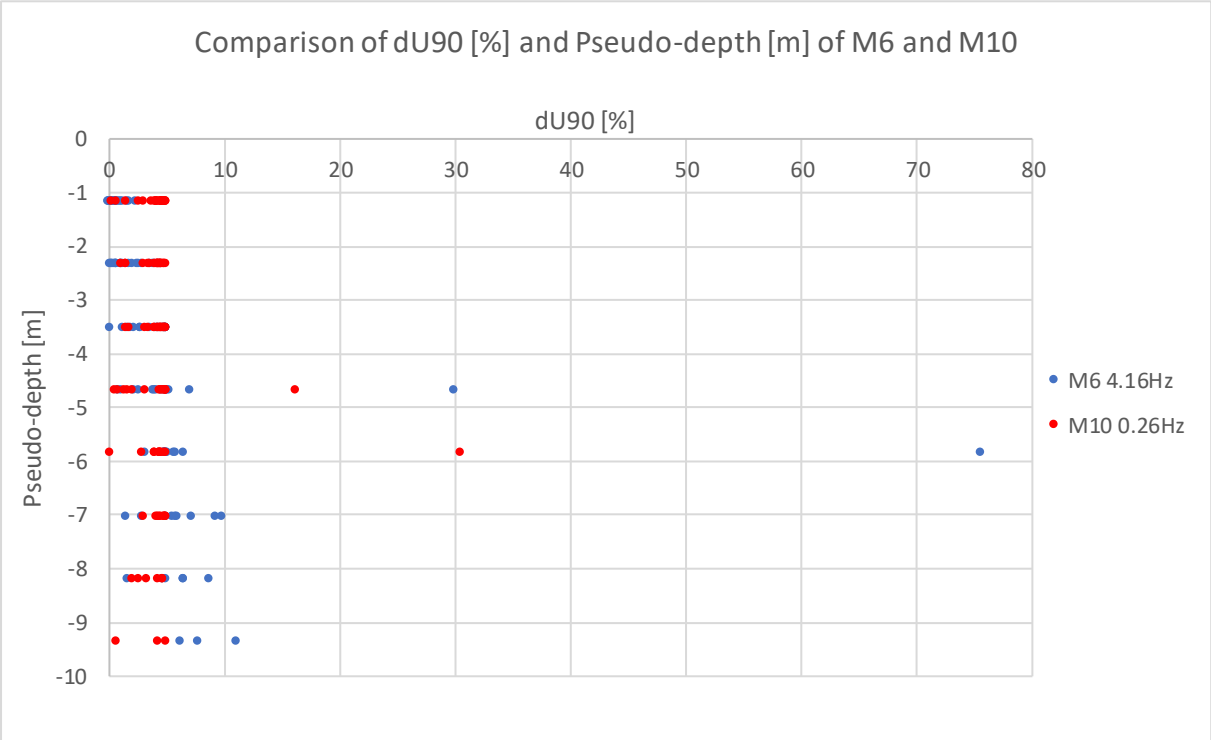

Figure 40: Shows the correlation of the dU90 values and the pseudo-depth for the two measurements M6 with 4.16Hz and M10 with 0.26Hz.

For comparison, the *M16-M20* measurement-series was also carried out with a Dipole-Dipole configuration, but steel electrodes were used. Again, starting with the general statistical evaluation of the *dU90* of the measurements *M16-M20*, *Table 21*. Here, too, the relatively high maximum values are noticeable, whereas the median values are acceptably low. Compared to the measurements with non-polarisable electrodes, the *dU90* values of those measurements with steel electrodes are slightly increased. However, measurement *M9* with 0.52Hz stands out due to the clearly higher mean value. With a value of 33.99%, this is strongly increased compared to the other measurements.

Table 21: Listing of the statistical evaluation of the dU90 values for the measurements M16-M20, with Dipole-Dipole configuration and non-polarisable electrodes.

M16 dU90 [%] - 4.16Hz		M17 dU90 [%] – 2.08Hz		M18 dU90 [%] – 1.04Hz	
min.:	0.017	min.:	0	min.:	0.017
max.:	43.66	max.:	35.33	max.:	35.47
mean value:	2.848	mean value:	2.466	mean value:	3.82
median:	2.163	median:	1.444	median:	4.507
standard deviation:	4.788	standard deviation:	3.713	standard deviation:	3.803
variance:	23.14	variance:	13.91	variance:	14.6

M19 dU90 [%] – 0.52Hz		M20 dU90 [%] – 0.26Hz	
min.:	0.099	min.:	0.361
max.:	3282	max.:	115.9
mean value:	33.99	mean value:	4.994
median.	4.575	median:	4.444
standard deviation:	314	standard deviation:	10.83
variance:	99547	variance:	118.3

Since measurement *M19* with a maximum value of 3282% extremely distorts the comparison with the other measurements, this outlier value was processed with the next-neighbour method to achieve better comparability of the measurements. *Figure 41* shows the original compilation of all *dU90* diagrams plotted against the *nr of measurement*. The outlier value of measurement *M9* is very significant and leads to a massive distortion of the y-axis, which means that the other values can hardly be represented. Therefore, this value was processed with the next-neighbour method.

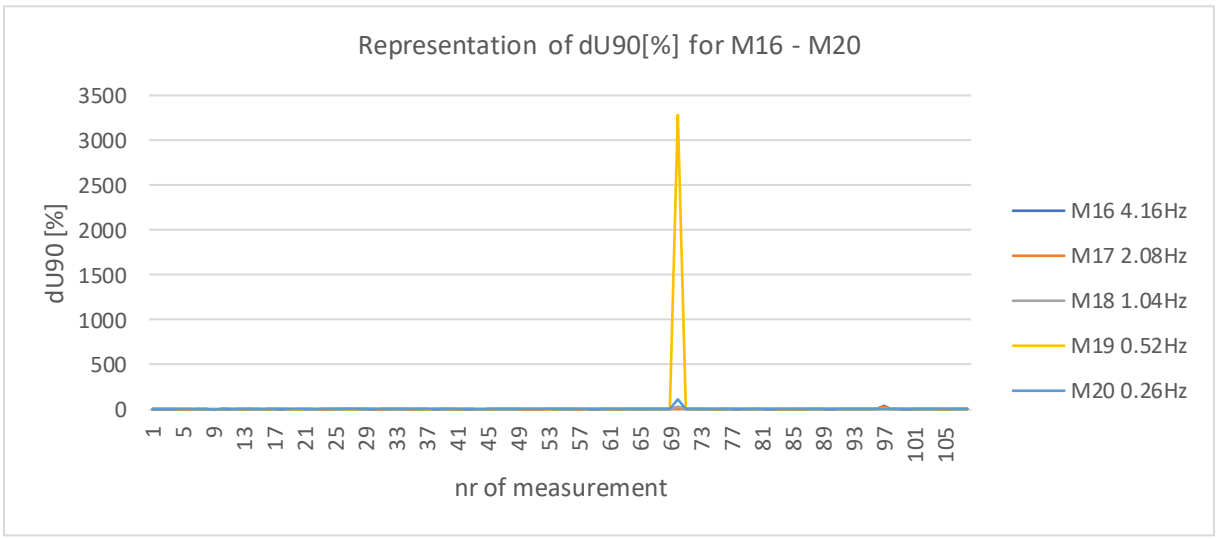

Figure 41: Unedited compilation of the diagrams for the measurement-series M16-M20. The outlier value of measurement M19 stands out strongly.

Figure 42 shows the edited diagram again; the changed scaling of the y-axis also makes the other measured values clearer visible.

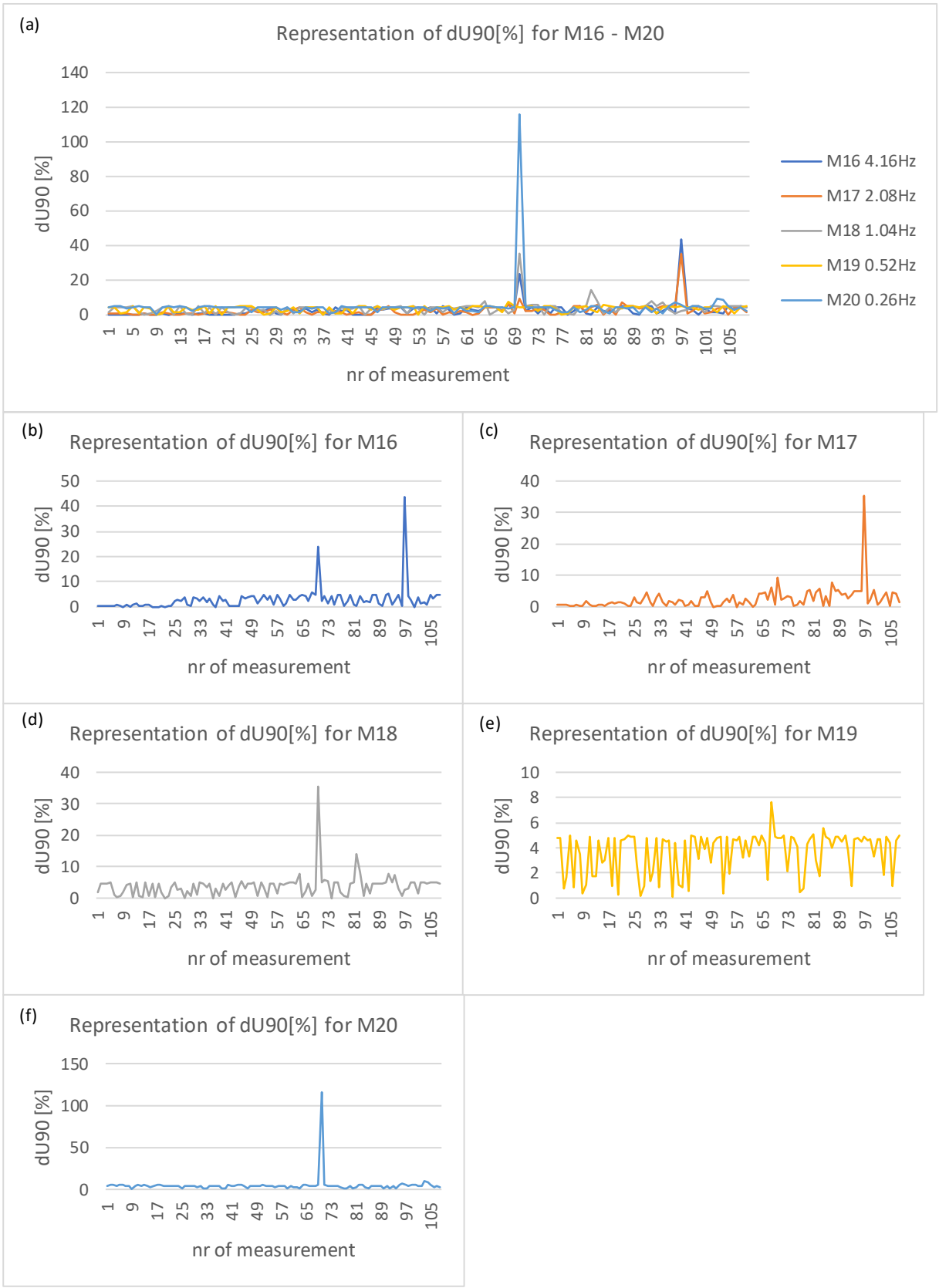

Figure 42: (a) all plots of d90 [%] values against nr of measurement for all five measurement frequencies used, edited for M19 (b) for the measurement frequency 4.16Hz (c) for the measurement frequency 2.08Hz (d) for the measurement frequency 1.04Hz (e) for the measurement frequency 0.52Hz (f) for the measurement frequency 0.26Hz.

When comparing *Figure 41* with *Figure 42 (a)*, it is noticeable that for all measurements except *M17* a peak occurs at *nr of measurement* 70. By editing the peak, the new value adapts to the surrounding values, this effect is clearly visible in *Figure 42 (a)*, as no strong peak is visible for measurement *M19* anymore. In the diagrams *42 (b)* to *42 (f)*, the edited diagram for measurement *M19* is striking: by removing the peak, the distribution of the other data values becomes better recognisable. Therefore, *Figure 42 (e)* shows a more similar picture to the diagrams of the Wenner measurement-series, see *Figures 36* and *Figure 34*. The remaining diagrams are similar to those of the Dipole-Dipole measurement-series *M6-M10*, as all these measurements are more affected by outlier values. The outlier values occur with the same *nr of measurement* as with the Dipole-Dipole measurement-series *M6-M10*. This means that defective connecting cables of the electrodes can be excluded, as different electrode types were used for the two Dipole-Dipole measurement-series. Therefore, this identical occurrence of the peaks seems to have something to do with the measurement configuration itself, as they only occur in the Dipole-Dipole measurement-series. In the Wenner measurement-series, the *dU90* values are generally lower or without such serious outliers and these measurements do not show any abnormalities at those *nr of measurement* where the Dipole-Dipole measurements show their peaks.

For the sake of completeness, *Figure 43* shows the dependence of the pseudo-depth on the *dU90* values. Here again a similar distribution of the *dU90* values can be seen as in the Wenner measurement-series: the higher-frequency measurement *M16* shows significantly lower *dU90* values over the entire pseudo-depth than the low-frequency measurement *M20*. There is also a stronger concentration of lower *dU90* value in lower pseudo-depths, which is particularly noticeable in the case of *M16*.

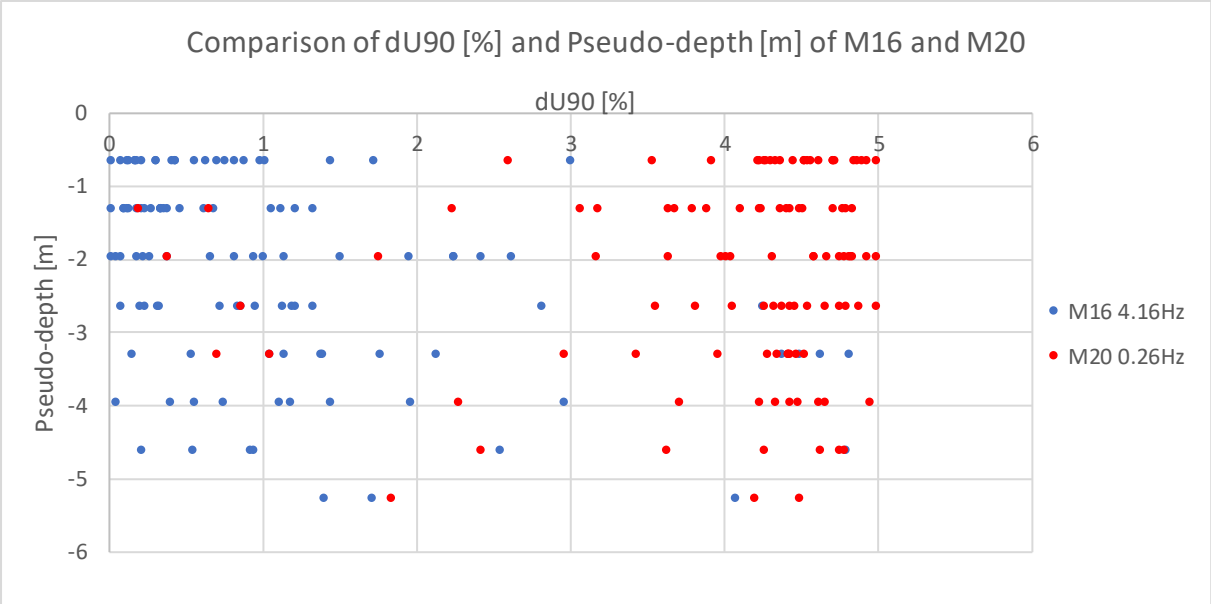

Figure 43: Shows the correlation of the dU90 values and the pseudo-depth for the two measurements M16 with 4.16Hz and M20 with 0.26Hz.

In order to be able to make a differentiated statement regarding the Dipole-Dipole measurement-series in relation to the IP effect, the phase angle comparisons were displayed in crossplots. All *phi* values are plotted against the measurement with the lowest frequency. *Figure 44 (a)* shows the compilation of the measurements *M6-M10*, which were carried out with non-polarisable electrodes.

In general, there is a greater scattering of the data, and negative *phi* values also occur. Especially the measurement *M7* with 2.08Hz shows a strong scattering of the measured values. In general, however, the picture is similar to the comparison of the *phi* values of the Wenner measurement-series, see *Figure 38*. The very low R^2 values are immediately noticeable. These R^2 values are very close to the value 0, which means that the scatter can be insufficiently explained.

Figure 44 (b) shows the *phi* values of the Dipole-Dipole measurement-series *M16-M20* which were carried out with the classic steel electrodes. Due to the outlier value of measurement *M18* with 1.04Hz, there is a distorted trend line in this diagram from the measurement with 1.04Hz. This trend line shows a completely different trend than the trend lines of the other measurements in this series. The outlier value of measurement *M18* with 1.04Hz is interpreted as a false measurement, as the *phi* value is >100mrad and this was determined as a false measurement in advance. The R^2 values of the *M16-M20* measurement-series are also very low and are close to 0, which means that the explanation of the scatter in this measurement-series can also be classified as insufficient.

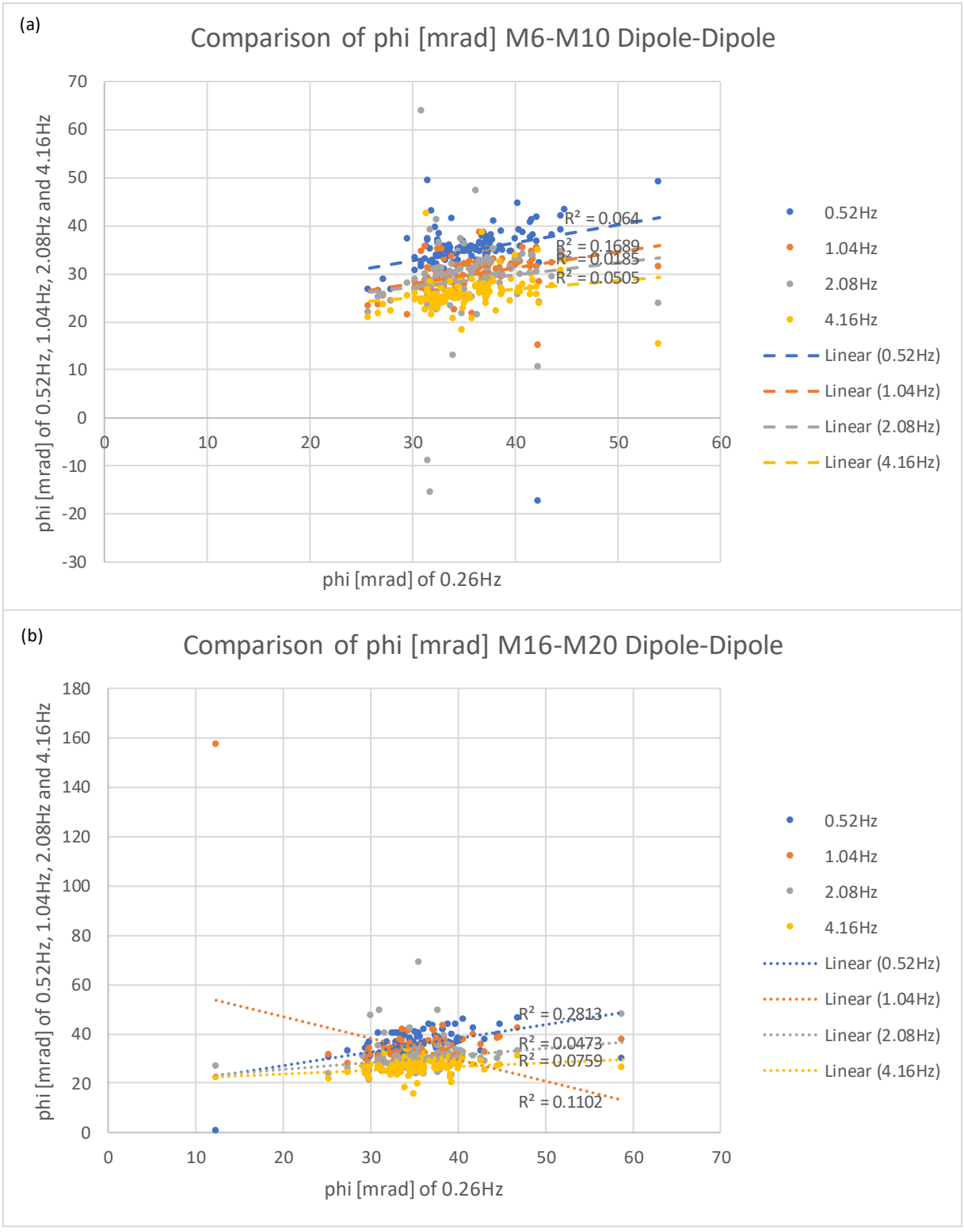

Figure 44: (a) Crossplot between the measurement at 0.26Hz against all other measurements at frequencies 4.16Hz, 2.08Hz, 1.04Hz and 0.52Hz for the measurement-series M6-M10 using non-polarisable electrodes and with Dipole-Dipole configuration. (b) Crossplot between the measurement at 0.26Hz against all other measurements with the frequencies 4.16Hz, 2.08Hz, 1.04Hz and 0.52Hz for the measurement-series M16-M20 using steel electrodes and with Dipole-Dipole configuration.

Conclusion of N-S profile

When comparing all measurements of the profile N-S, different aspects can be recognised that lead to answers of the extended question. Both in the Wenner configuration measurements and in the comparative measurements with Dipole-Dipole it is clearly noticeable that those measurements that were carried out with non-polarisable electrodes have a better data quality with regard to the analysed *dU90* and *phi* values. Compared to this, the scatter and the occurrence of outlier values is significantly higher in the measurement-series with the classic steel electrodes. These observations confirm the original thesis, which has also been put forward in the literature: the use of non-polarisable electrodes is recommended for IP measurements compared to the classic steel electrodes. Even if the handling of these electrodes is somewhat more complex and the electrodes are more sensitive with regard to their hardware compared to the metal spikes. But the measured values speak for a measurement with non-polarisable electrodes in order to achieve the best possible data quality.

8.1.2. West-East profile

As a comparison profile, a W-E profile was drawn that has an intersection with the N-S profile near the gas dome. The W-E profile was measured with the original intention to exclude directionality of the IP measurement. The hope was also to obtain additional evidence to prove the presence of the gas dome. To create comparability, the exact same measurements were taken in the same order as for the N-S profile. The order of the measurements has no influence on the results but is merely intended to facilitate navigation between the different measurements. No detailed analysis of this W-E profile is given below, as the individual steps have already been sufficiently described. The statistical evaluations and *dU90* diagrams can be found in the *electronic Appendix*. Only the crossplots with the *phi* values and a general comparison of the two measurement profiles are given.

For the two Wenner measurement-series *M21-M25* and *M31-M35*, the *dU90* values in the statistical evaluation lie in a comparably similar value range as those of the measurement-series *M1-M5* and *M11-M15* in the N-S profile. There are isolated outliers that show up in the maximum values, such as measurement *M23* with a maximum dU90 of 12.96% or measurement *M34* with a maximum dU90 of 10.05%. However, these maximum values alone are not a sign of poor measurement quality. Especially when looking at the other statistical values in parallel, especially the median, it is noticeable that the measured data volumes of these measurement-series can be classified as valid and plausible. The *dU90* plots show a very similar error distribution, with majority values <5% and few outliers exceeding this limit. Somewhat higher *dU90* values tend to be found in the low-frequency measurements, whereas the higher-frequency measurements, especially 4.16Hz and 2.08Hz, show a majority of *dU90* values between 0 and 2%. This picture is shown by the diagrams of the measurements with metal electrodes as well as those with non-polarisable electrodes.

The Dipole-Dipole configuration was carried out for the measurement-series *M26-30*, metal electrodes, and *M36-M40*, non-polarisable electrodes. Thus, they represent the direct comparison measurements to the measurement-series *M6-M10* and *M16-M20* of the N-S profile. Again, very similar statistical values are found when comparing these series of measurements of the W-E profile and the N-S profile, although the values of the W-E profile are slightly higher than those of the N-S profile. In general, the values are strongly increased compared to the measurements with Wenner configuration. A particularly strong outlier occurs in measurement *M39* with a maximum *dU90* value of 11255%. Otherwise, measurements *M26*, *M29*, *M30* as well as *M36* and *M37* each show a maximum value of >100%, in each case an incorrect measured value can be assumed. The unprocessed *dU90* diagrams of the Dipole-Dipole measurements are strongly influenced by the outliers and apart from that hardly allow any interpretations. This is the case for all measurements with Dipole-Dipole configuration.

Since the IP effect is the focus of the investigations, the *phi* diagrams are presented in particular in the following, as these provide an insight into the general distribution of the *phi* values and thus enable statements to be made about the IP effect. For this purpose, the *phi* values of the higher frequency measurements were plotted against the measurement with the lowest frequency of 0.26Hz. These plots were made for the associated measurement-series. In addition, trend lines were created and plotted in the diagrams together with the coefficient of determination R^2 for each measurement. This allows a more differentiated statement about the scatter of the data.

The comparison of the *phi* diagrams of the measurement-series *M21-M25* and *M31-M35* begins, *Figure 45 (a)* and *Figure 45 (b)*. Both series of measurements were carried out with the Wenner configuration and show a similar distribution of *phi* values. No negative measured values occur, and the majority of the data lies between 15 and 40mrad. The data clouds of all compared measurements show an acceptable scatter rate, also the superimposed coefficients of determination R^2 show this. In general, the values of the coefficients of determination for all measurements are in a range that means a good explanation of the scatter. The only exception is the measurement *M22* with 2.08Hz which only has a coefficient of determination of R^2=0.2789. This means that the regression model cannot sufficiently explain the scatter of the data. This is also recognisable by the greater scatter of the data cloud with individual data points that clearly deviate from the regression model. When comparing *Figures 45 (a)* and Figure *45 (b)*, it can be seen that the scatter is larger when using steel electrodes, which is also reflected in the lower values of the coefficients of determination R^2 in *Figure 45 (a)* compared to those from *Figure 45 (b)*.

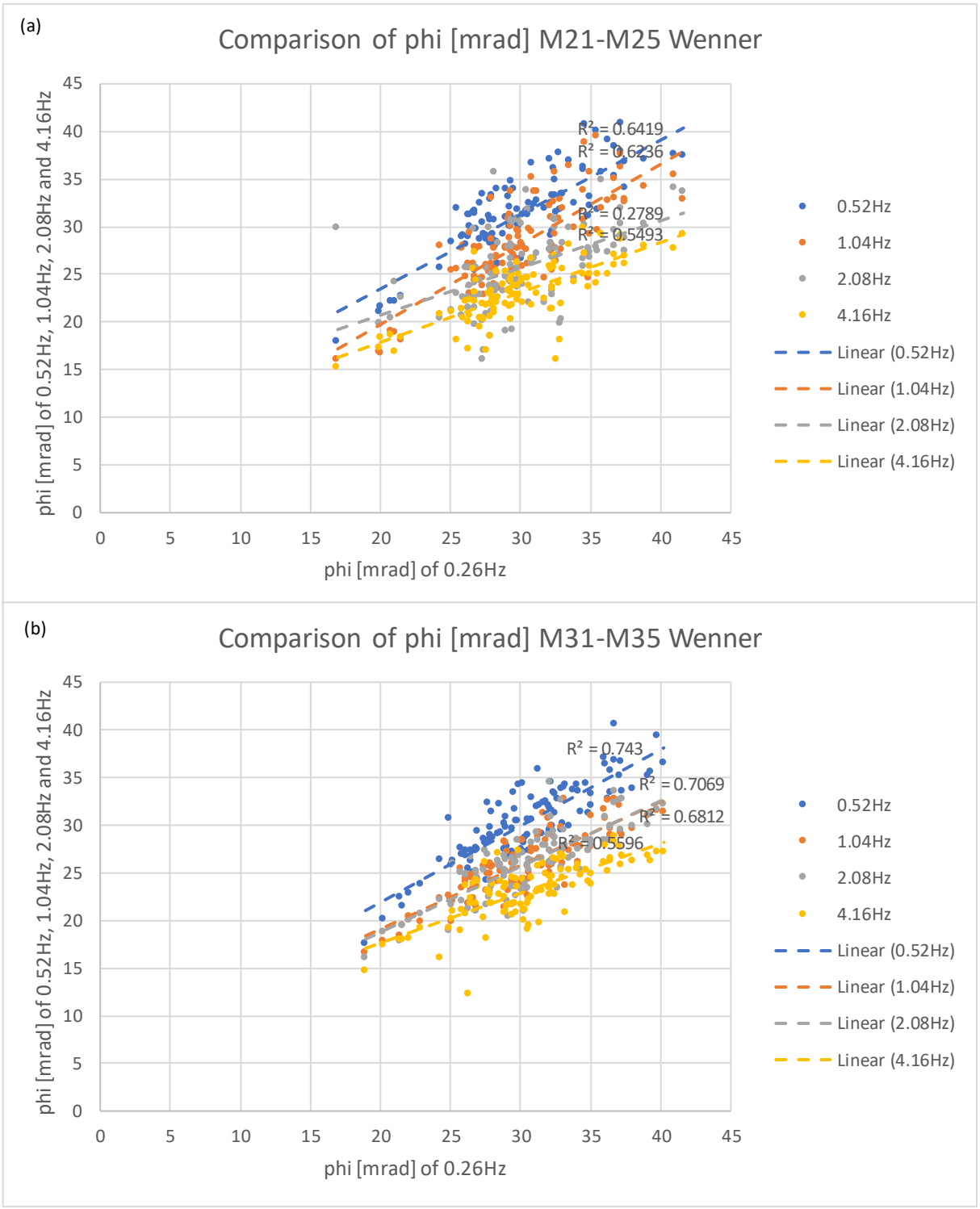

Figure 45: (a) Crossplot between the measurement at 0.26Hz against all other measurements at frequencies 4.16Hz, 2.08Hz, 1.04Hz and 0.52Hz for the measurement-series M21-M25 using steel electrodes and with Wenner configuration. (b) Cross plot between the measurement at 0.26Hz against all other measurements with the frequencies 4.16Hz, 2.08Hz, 1.04Hz and 0.52Hz for the measurement-series M31-M35 using non-polarisable electrodes and with Wenner configuration.

Such crossplots were also created for the measurement-series *M26-M30* and *M36-M40*, which were carried out with Dipole-Dipole configuration. These are shown *in Figure 46 (a)* and *Figure 46 (b)*. The isolated negative values that can be found in both figures are striking. Besides these negative values, there are also some outliers with high phi values >100mrad. Especially in *Figure 46 (a)* of the measurement-series *M26-M30* using steel electrodes, there are more outlier values in negative or positive directions. This trend of increased scattering using steel electrodes is also in line with the results of the measurements carried out with Wenner configuration. The core of the data clouds is concentrated in the <50mrad range, which is in the same value range as the Wenner configurations. In *Figures 46 (a)* and *Figure 46 (b)* these data clouds are not shown in such detail due to the outliers and thus it is not easy to see to which data cloud which coefficient of determination belongs. Therefore, this is listed separately for the respective measurements in *Table 22*.

Table 22: Shows the coefficients of determination R^2 for the measurements M26-M39 which can be seen in Figure 46 (a) and Figure 46 (b).

measurement	R^2	measurement	R^2
M26	0.5872	M36	0.1863
M27	0.02	M37	0.0357
M28	0.2921	M38	0.436
M29	0.0723	M39	0.6084

Looking at *Table 22*, it is immediately noticeable that all the R^2 values listed, with the exception of *M26* and *M39*, are very low and close to 0. Such a low coefficient of determination means that the generated regression models cannot sufficiently explain the existing data clouds. The R^2 values of the measurement-series *M36-M39* in *Table 22* show slightly higher values than for the measurement-series *M26-M29*. This can again be attributed to the difference between the measurement-series with non-polarisable electrodes and with steel electrodes: *M36-M40* was measured with non-polarisable electrodes and shows correspondingly higher R^2 values compared to those measured with steel electrodes.

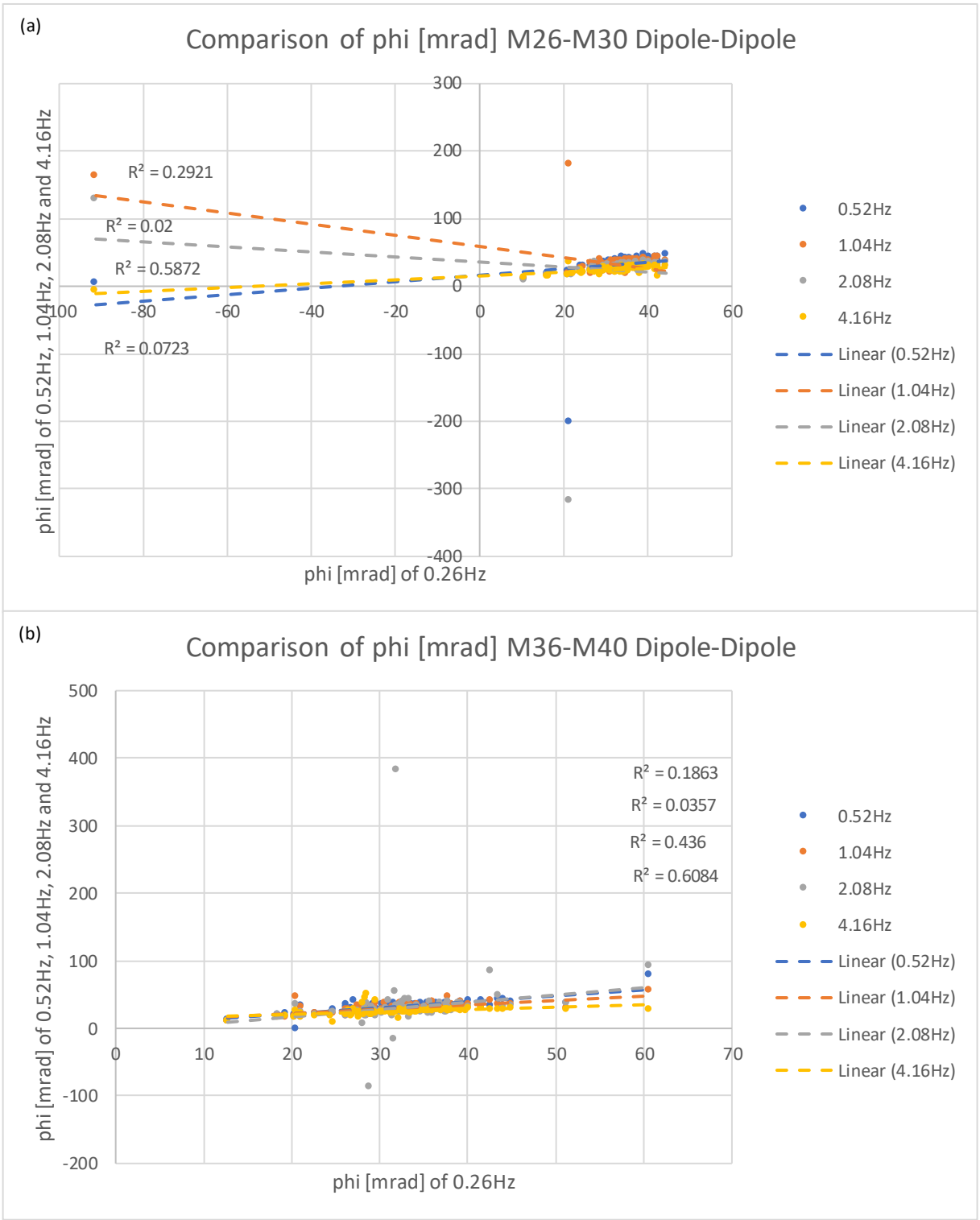

Figure 46: (a) Crossplot between the measurement at 0.26Hz against all other measurements at frequencies 4.16Hz, 2.08Hz, 1.04Hz and 0.52Hz for the measurement-series M26-M30 using steel electrodes and with Dipole-Dipole configuration. (b) Crossplot between the measurement with 0.26Hz against all other measurements with the frequencies 4.16Hz, 2.08Hz, 1.04Hz and 0.52Hz for the measurement-series M36-M40 using non-polarisable electrodes and with Dipole-Dipole configuration.

Conclusion of W-E profile:

When comparing the measurement-series of W-E profile, similar trends can be seen as with the N-S profile. The statistical evaluation of the *dU90* values shows a generally good measurement quality, with a tendency towards more stable *dU90* values for those measurement-series that were carried out with Wenner configuration. Those with Dipole-Dipole configuration show larger maximum values, which, however, can already be classified as outlier values. This results in large variance values, but the median values are within acceptable ranges, i.e., 50% of the data values are below this value. Therefore, at least the majority of the data can be considered acceptable and valid, although there are still some outlier values. The discussed crossplots of the *phi* values enable a good interpretation of the various measurements through a visual representation of the results of the IP effect. As a result, the same conclusions can be drawn as for the N-S profile: the Wenner configuration shows a more stable quality of the *phi* values compared to the Dipole-Dipole configuration and the resulting better compatibility of the regression models. The same applies to the comparison between steel electrodes and non-polarisable electrodes: the non-polarisable electrodes are preferable to the steel electrodes for measurements with a focus on the IP effect.

8.1.3. Comparison between the N-S and W-E profile

The W-E profile was measured with the original purpose of being able to rule out a directional dependency of the measurement or to obtain additional indicators and indications of measurement sensitivity with regard to the gas dome as the measurement objective. The measurements carried out are identical on both profiles in terms of their settings and measurement configurations. The statistical evaluation of the *dU90* values as an error indicator as well as the investigation of the correlations of the *phi* values and the crossplots generated from them show almost identical results for the measurements of both profiles. Thus, the following statements could be confirmed for the measurements carried out here for both the N-S profile and the W-E profile: *(1)* the measurements with Wenner configuration show a more stable data quality with few to no outlier values based on the statistical evaluation. The measurements with Dipole-Dipole configuration, on the other hand, show clear fluctuations in the *dU90* values as well as the *phi* values, which, however, are not necessarily related. The distribution of the outliers can also only be attributed to a limited extent to certain electrode arrangements that were actively switched during the individual measurement. For the most part, there is an incomprehensible pattern of extremely deviating values that are subsequently interpreted as incorrect measurements. *(2)* The statement from the literature regarding the use of non-polarisable electrodes could be confirmed. These show a smaller scatter of the data and a better fit of the regression models for the measured *phi* values. This effect is clearly visible in the crossplots. For the subsequent analysis of the inversions carried out and the models obtained from them, the

following thesis must be checked: If the differences between measurements with non-polarizable electrodes and steel electrodes in the final inversion models are classified as too small, then one could generally use non-polarizable electrodes for these measurements carried out here, reconsider them with reference to the aspect of working time and intensive work.

The non-polarizable electrodes used here are self-made and are also somewhat fragile due to their age, which means that more careful handling during installation in the field is required. The filling of these electrodes with the $CuSO_4$ solution is also time-consuming, especially if this has to be refilled again and again throughout the measurement day, since the loss of liquid into the subsoil is too great. There is a risk that an electrode will run dry during a measurement and then generate incorrect measurement values. This fact can lead to problems and massive time delays, especially when using the *Lippmann 4 point light 10W* measuring device and when measuring with low frequencies, which have long measuring times.

From this, a differentiated examination of this topic must also take place in the course of the analysis of the generated inversion models, in order to illuminate not only the characteristics in the raw data, such as a lower data scatter, but also the characteristics in the final inversion models in order to examine all aspects, such as in the include discussion. In particular, the work intensity and the time component should not be ignored, as these affect the costs of commercial measurements. Of course, it must also be considered that the problems of the non-polarisable electrodes used here cannot be transferred one-to-one to all non-polarisable electrodes that are on the market, since they are self-made and already have some signs of aging such as leaking tips, which there is an increased loss of liquid into the subsoil.

8.2. Evaluation of the inversions carried out for the profiles N-S and W-E

For all measurements carried out, inversions were performed with the inversion software *Res2dinv*. This made it possible to obtain inversion models for each measurement for both the IP measurements and the resistance tomography, with the focus on the IP measurement. The resistivity models are nevertheless created automatically but are not a main component of the interpretation in this evaluation.

In general, the inversion models are compared and analysed within a category, i.e., measurement configuration and electrode type used, as well as across categories.

N-S profile M1-M5 compared to M11-M15:

Starting with a comparison of the inversion models of the measurement-series *M1-M5* and *M11-M15*. *Table 23* lists the measurement parameters of these two measurement-series:

Table 23: List of the measurement parameters of the two measurement-series M1-M5 and M11-M15 along the N-S profile.

Measurement-series	Measurement configuration	Electrode type	Measuring frequencies
M1-M5	Wenner	Unpolarizable ($CuSO_4$)	4.16Hz, 2.08Hz, 1.04Hz, 0.52Hz, 0.26Hz
M11-M15	Wenner	Metal	4.16Hz, 2.08Hz, 1.04Hz, 0.52Hz, 0.26Hz

The aim is to identify the differences that have already been worked out in the statistical analysis of these measurement-series in the quality of the inversion models. In addition, the focus is on whether the presence of the gas dome can be detected in the inversion models.

The inversion models, including the measured and the calculated pseudo sections, are listed in *Figure 48*. The measurement-series *M1-M5* is shown with descending frequencies from 4.16Hz to 0.28Hz in the left column and the measurement-series *M11-M15*, also with descending frequencies from 4.16Hz to 0.28Hz, on the right. According to this, the models lying at the same level in each case only differ based on the electrode type used. *Figure 48* should help to obtain a general overview of the inversion models of the measurement-series to be compared. The two pseudo sections for the measured and the calculated pseudo sections are also shown, so that more differentiated statements can be made about the validity of the inversion models generated from them.

For all inversion models shown, which were performed with the *Lippmann 4 point light 10W*, the following range of values was chosen for the representation of the phase angles, see *Figure 47*. Reference was made to the analytical evaluation, in which such a range of data values already emerged.

Figure 47: enlarged view of the range of phase angles in mrad for all measurements made with the Lippmann 4 point light 10W.

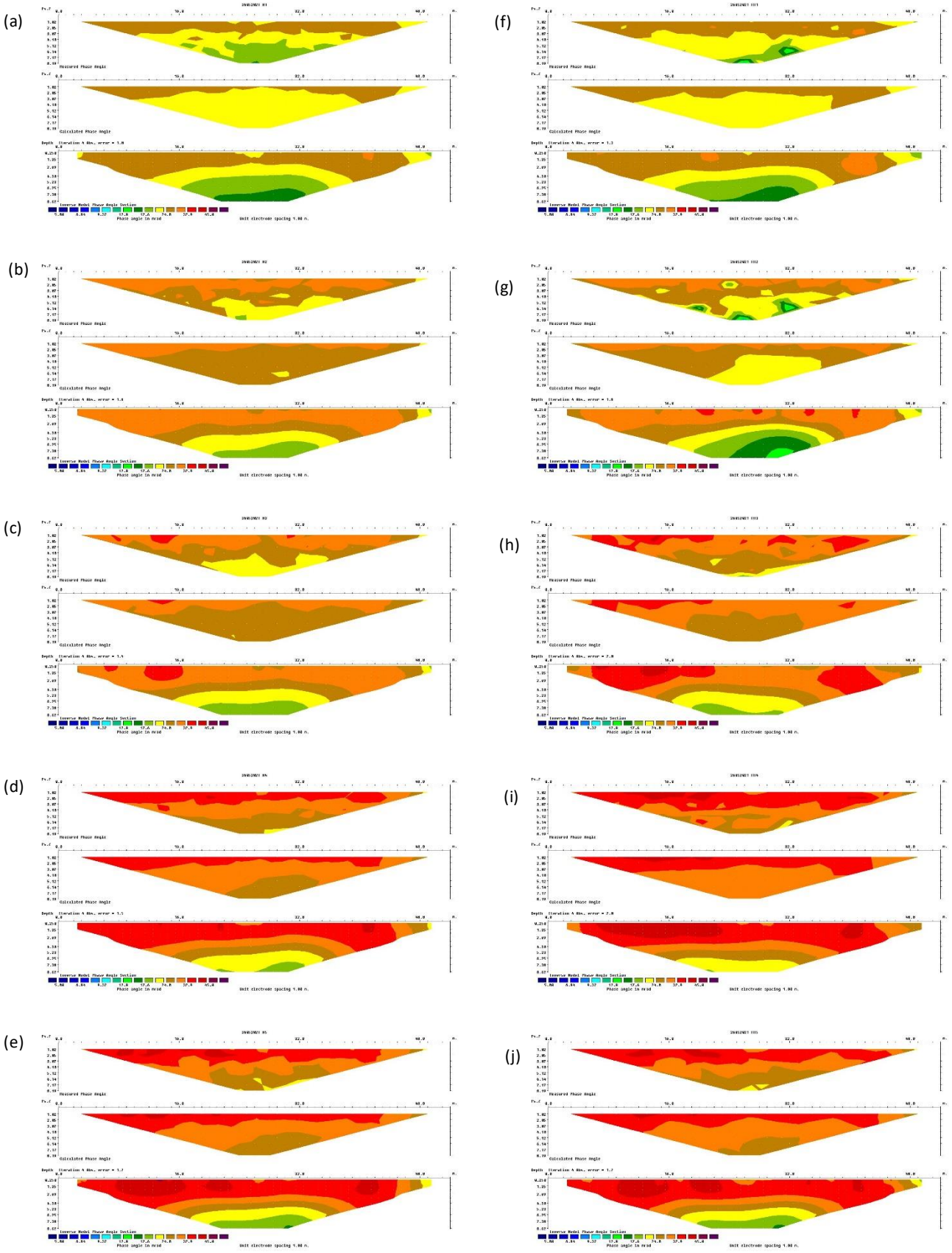

Figure 48: Shows the inversion models of the measurement-series M1-M5 (a)-(e) and M11-M15 (f)-(j). The respective inversion model is always the lowest of the three related sections. The two pseudo sections of the measured (top) and calculated (middle) values are also shown here. The measurement frequencies run from 4.16Hz (top figure) to 0.28Hz (bottom figure) in the same order for both measurement-series.

When looking at *Figure 48*, it is noticeable that the fundamentally occurring structures can be seen in all models. It is noticeable that near the surface there is a zone with larger phase angles, which is marked with brownish to red colours. The phase angles decrease with increasing depth, this is represented by the yellow and green colours. This trend can be seen in all models. The higher phase angles are more pronounced in layers near the surface. A zone with lower phase angles can be seen there in all models and also in the pseudo sections of the measured and calculated values. In the inversion models, the transition between the zone with higher phase angles and that with lower phase angles appears almost horizontally at a depth of about 6m below ground level. The spherical centers with higher phase angles are located in the near-surface zone at an average depth of up to 2m below ground level. The general data distribution of these series of measurements shows that the landfill body largely has values around 30mrad, indicated by the orange colour. It is noticeable that the lower the measurement frequency, the higher the measured phase angles: the colour scheme changes significantly from brownish-yellow for the measurements with 4.16Hz to orange-red for the measurements with 0.28Hz.

A closer look at the pseudo sections (upper and middle figure) also shows good agreement between the two series of measurements. The measured pseudo sections of the higher-frequency measurements (4.16Hz and 2.08Hz) show a significantly more disturbed picture than with the low-frequency measurements. This can be seen from the significantly more restless and irregular data values that are displayed in the corresponding colours in the pseudo sections. Compared to this, the pseudo sections in the low-frequency measurements are very similar, suggesting good agreement and high measurement precession.

However, there is no clear indication of the presence of the gas dome, which is located in the middle of the profile and, according to theory, should show a strong deflection in the IP measurements due to its metallic structure. The regions with higher phase angles around 45mrad tend to occur near the surface and show no correlation with the location of the gas dome.

The following can be said about the quality of the inversion: the average iteration errors after 4 iteration steps can be classified as very low for both series of measurements with *(a)* 1.44% for series of measurements *M1-M5 (b)* 1.76% for series of measurements *M11-M15*, although especially with the higher-frequency measurement sweeps shows a certain difference between the pseudo sections of the measured and the calculated data. In the case of the low-frequency measurements of 1.04Hz, 0.52Hz and 0.28Hz, these differences between the two pseudo sections are not very pronounced.

N-S Profile M6-M10 compared to M16-M20:

The same comparison of the inversion models is also carried out for the two measurement-series *M6-M10* and *M16-M20*. These were both performed in the Dipole-Dipole configuration and again differ in the type of electrodes used. *Table 24* lists the measurement parameters of the two measurement-series:

Table 24: List of the measurement parameter of the two measurement-series M6-M10 and M16-M20 along the N-S profile.

Measurement-series	Measurement configuration	Electrode type	Measuring frequencies
M6-M10	Dipole-Dipole	Unpolarizable ($CuSO_4$)	4.16Hz, 2.08Hz, 1.04Hz, 0.52Hz, 0.26Hz
M16-M20	Dipole-Dipole	Metal	4.16Hz, 2.08Hz, 1.04Hz, 0.52Hz, 0.26Hz

The inversion models including the pseudo sections of the measured and calculated values are shown in *Figure 49* in the same scheme as in *Figure 48* for the inversion models of the measurement-series *M1-M5* and *M11-M15*.

Compared to the inversion models of *Figure 48*, the results of the Dipole-Dipole configuration show much more disturbed images. *Figure 49 (b)* and *(d)* are particularly striking: The reason for this could be the negative phase angles that occur in these measurements, although they are not shown due to the generally adjusted scale of the phase angles. Interestingly, however, these only occur in the measurements with non-polarisable electrodes.

In general, however, the picture is different from the evaluations in *Figure 48*. The layered structure is no longer so dominant, but spherical zones with higher phase angles appear more frequently. The gas dome is again not clearly recognizable. One common feature with the inversion models of the Wenner configuration can be identified, however: the lower the measurement frequency, the higher the average phase angles displayed. This is again recognizable by a change in the colour scheme from beige-yellow for the measurements with 4.16Hz to mostly red colours for the dump body and values around 45mrad for the measurements with 0.28Hz.

Important to be able to make statements about the quality of the models is, among other things, the agreement of the pseudo sections of the measured and the calculated values. These show a certain agreement, but by far not in the same precession as in the measurements with Wenner configuration. Another indicator that is treated in this respect is the iteration error of the individual inversion models. After 4 iteration steps, the average iteration error is *(a)* 2.34% for the measurement-series *M6-M10 (b)* 2.56% for the measurement-series *M16-M20*. Thus, the iteration errors are significantly higher than those of the Wenner configuration.

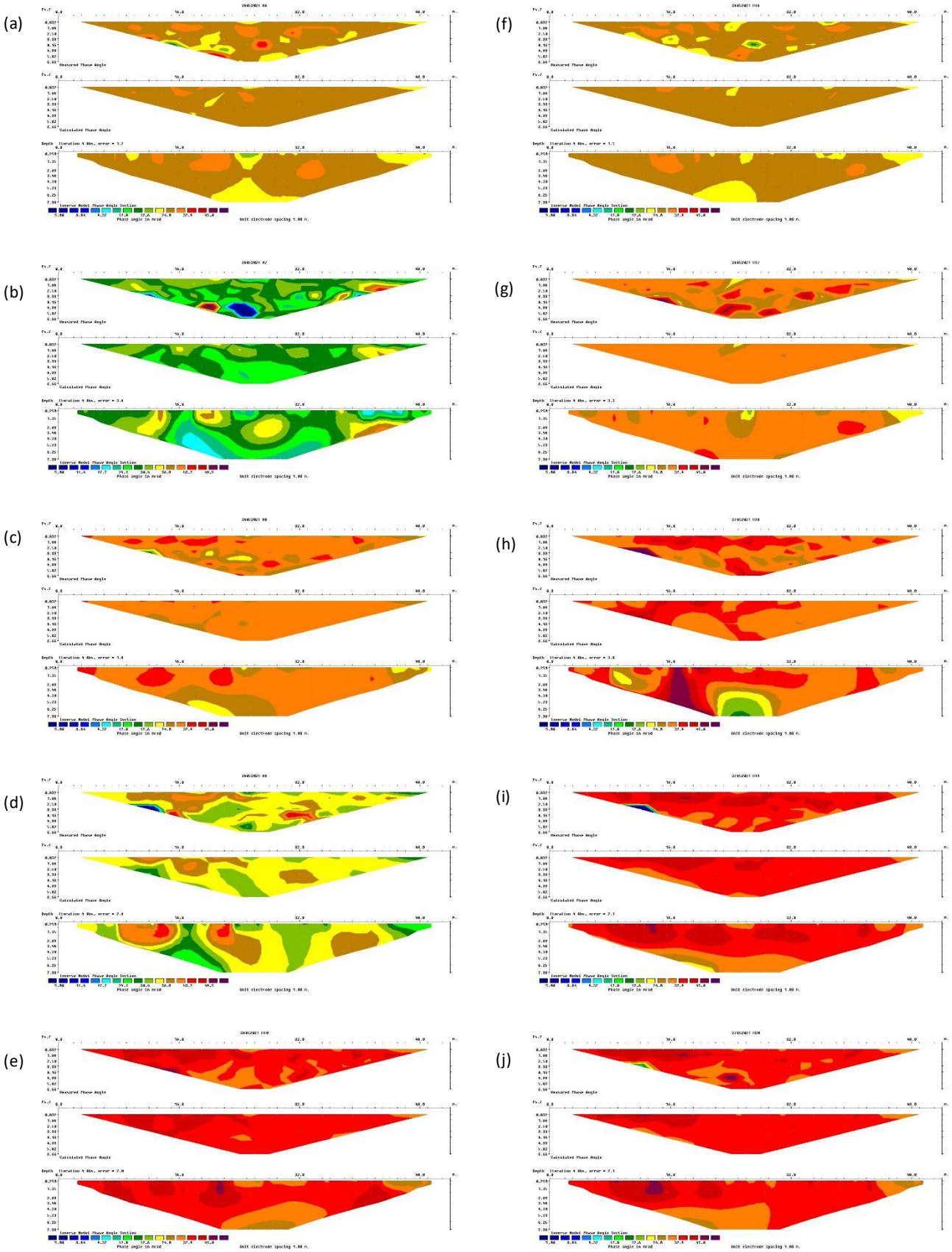

Figure 49: Shows the inversion models of the measurement-series M6-M10 (a)-(e) and M16-M20 (f)-(j). The respective inversion model is always the lowest of the three related sections. The two pseudo sections of the measured (top) and calculated (middle) values are shown here. The measurement frequencies run from 4.16Hz (top figure) to 0.26Hz (bottom figure) in the same order for both measurement-series.

The nearly horizontal transition to lower phase angles at a depth of 6m as seen in *Figure 48* is not seen in the results in *Figure 49*. Although the phase angles also decrease with increasing depth, the transition is not shown in the same detail. This transition is most readily seen in the two low frequency measurements, *Figure 49 (e)* and *(j)*, although positionally this appears to be mirrored.

W-E profile M31-M35 compared to M21-M25:

The W-E profile was laid directly after the N-S profile. This is intended to generate additional information and data that indicate the presence of the gas dome and at the same time to rule out any directional dependency of the measurements.

It begins with the comparison of the measurement-series *M31-M35* and *M21-M25*, both of which were carried out in the Wenner configuration. The remaining measurement parameters of these two series of measurements can be found in *Table 25*.

Table 25: List of the measurement parameters of the two measurement-series M31-M35 and M21-M25 along the W-E profile.

Measurement-series	Measurement configuration	Electrode type	Measuring frequencies
M31-M35	Wenner	Unpolarizable ($CuSO_4$)	4.16Hz, 2.08Hz, 1.04Hz, 0.52Hz, 0.26Hz
M21-M25	Wenner	Metal	4.16Hz, 2.08Hz, 1.04Hz, 0.52Hz, 0.26Hz

In *Figure 50*, the inversion models and the associated pseudo sections are presented in the same style as in *Figures 49* and *Figure 48*. The results of the measurement-series *M31-M35* are on the left and those of *M21-M25* are on the right. The frequencies are again listed in decreasing order of magnitude, with the top figure measured at a frequency of 4.16Hz and the bottom figure correspondingly at a frequency of 0.28Hz.

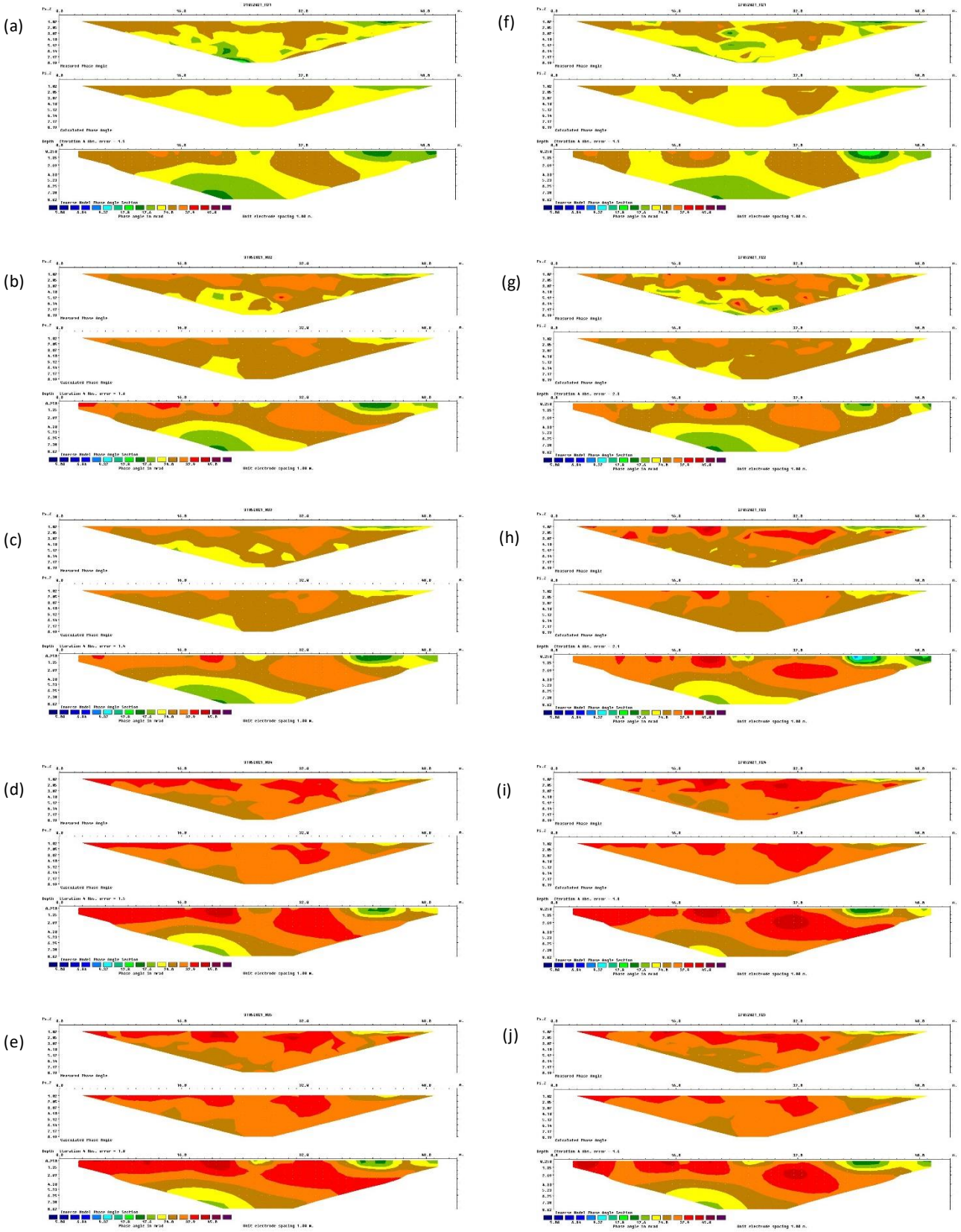

Figure 50: Shows the inversion models of the measurement-series M31-M35 (a)-(e) and M21-M25 (f)-(j). The respective inversion model is always the lowest of the three related sections. The two pseudo sections of the measured (top) and calculated (middle) values are shown here. The measurement frequencies run from 4.16Hz (top figure) to 0.26Hz (bottom figure) in the same order for both measurement-series.

The inversion models of F*igure 50* show a certain similarity with those of *Figure 48*, although some differences are to be pointed out. For example, the layered structure of *Figure 48* is not dominantly represented, but spherical regions with elevated phase angles are more prominent. These can be seen particularly well in the models of the right column of *Figure 50*. In the models *(a)* to *(e)*, which were carried out with non-polarisable electrodes, these areas are rather connected and not individual patches. At greater depth of investigation, a decrease in phase angles can again be seen, although this is not as prominent as in *Figure 48*. In the eastern part of the profile, all inversion models of *Figure 50* show a near-surface region with very low phase angles around 12.8mrad, marked by green colours. A near-surface gravelly layer was identified in the field in this area. The absence of fine-grained soil material and the greater pore content of the gravellier areas results in a general reduction in current flow, causing the measured values in these areas to decrease.

The inversion models of *Figure 50* show identical structures overall, although the measured phase angles are higher for the low-frequency measurements. There, phase angles of up to 45.0mrad are shown in the landfill body, whereas these are only around 24.0mrad for the higher frequency measurements. The differences between measurements with non-polarisable and metallic electrodes is marginal. With regard to the iteration errors, there are also few differences: The average iteration error after four iteration steps is relatively low for both measurement-series with *(a)* 1.56% for measurement-series *M31-M35 (b)* 1.86% for measurement-series *M21-M25*. This is comparable to the iteration error of the measurement-series *M1-M5* and *M11-M15*, whereby the iteration error of the measurement-series carried out with metallic electrodes is slightly higher than that of the measurement-series with non-polarisable electrodes.

W-E Profile M36-M40 compared to M26-M30:

Finally, the two measurement-series *M36-M40* and *M26-M30* are compared. Both were performed with the Dipole-Dipole configuration, further measurement parameters are listed in *Table 26*.

Table 26: List of the measurement parameters of the two measurement-series M36-M40 and M26-M30 along the W-E profile.

Measurement-series	Measurement configuration	Electrode type	Measuring frequencies
M36-M40	Dipole-Dipole	Unpolarizable ($CuSO_4$)	4.16Hz, 2.08Hz, 1.04Hz, 0.52Hz, 0.26Hz
M26-M30	Dipole-Dipole	Metal	4.16Hz, 2.08Hz, 1.04Hz, 0.52Hz, 0.26Hz

Figure 51 shows the listing of the inversion models of the measurement-series M36-M40 and M26-M30 with the same structure as in the previous compilations. The measurement runs of the

measurement-series *M36-M40* are shown on the left, *Figure 51 (a)-(e)*, and those of the measurement-series *M26-M30* on the right, *Figure 51 (f)-(j)*.

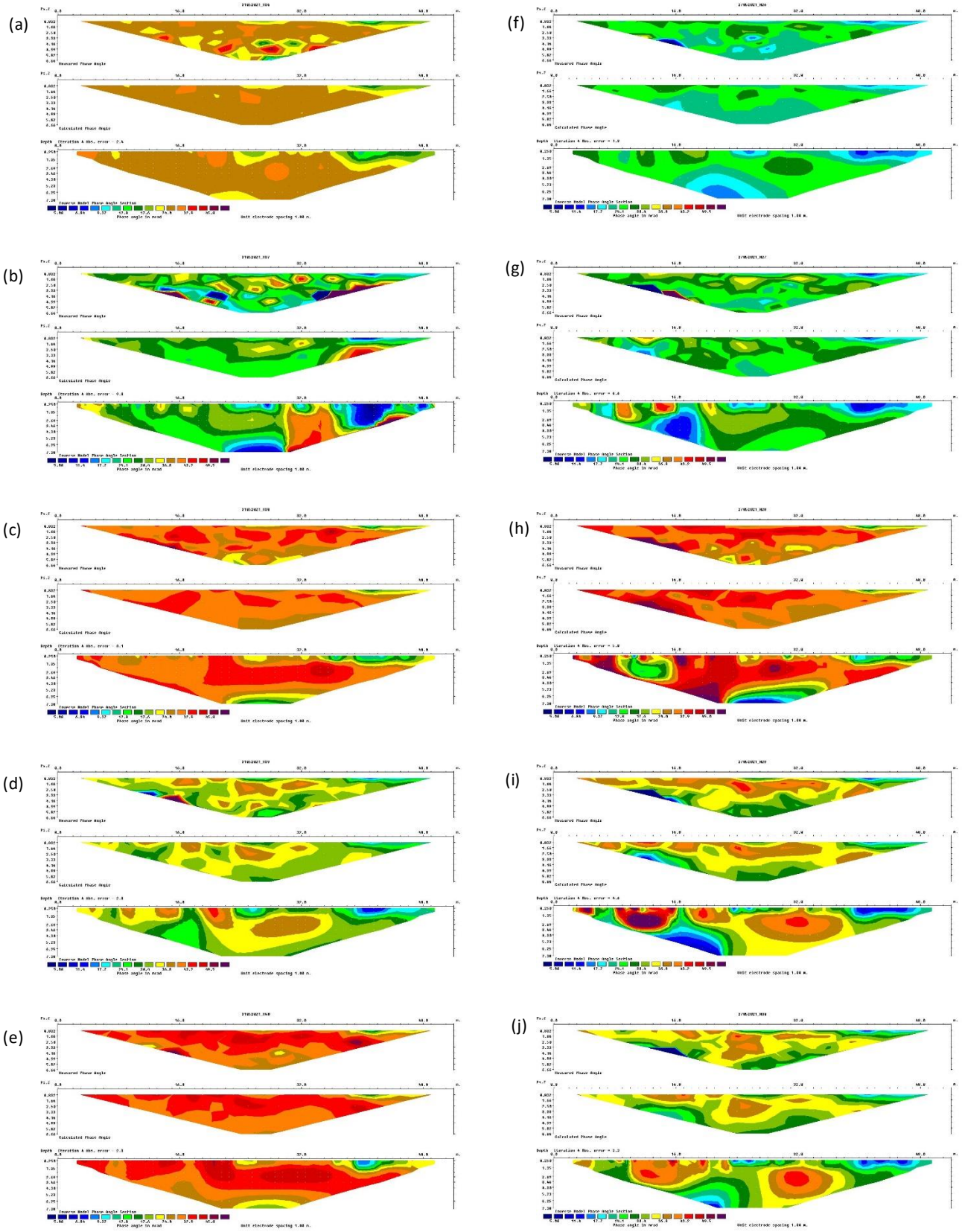

Figure 51: Shows the inversion of the measurement-series M36-M40 (a-e) and M26-M30 (f-j). The respective inversion model is always the lowest of the three related sections. The two pseudo sections of the measured (top) and calculated (middle) values are shown here. The measurement frequencies run from 4.16Hz (a and f) to 0.26Hz (e and j) in the same order for both measurement-series.

The models and pseudo sections of the measurement-series with Dipole-Dipole configuration show much more disturbed and restless distributions of the phase angles. Compared to the measurements with Wenner configuration, the inversion models of *Figure 51* are not very informative: the models show little agreement, both within a measurement-series (a)-(e) and compared to the measurement-series (f)-(j). The measured phase angles also vary: measurement *M37* at 2.08Hz, *Figure 51 (b)*, has phase angles in the range of 12.8mrad. Measurement *M38* with 1.04Hz, *Figure 51 (c)*, shows already significantly higher phase angles of up to 45mrad. Despite the identical scale of the phase angles, entirely different inversion models are shown. The inversion model in *Figure 51 (e)* shows the closest agreement with the models in *Figures 50* and *48*, but the eastern near-surface region with low phase angles also shows up in the inversion models of *Figure 51*. Also, the pseudo sections of the individual measurements show partly clear differences, whereby no good measurement quality can be guaranteed.

The average iteration errors after four iteration steps are *(a)* 4.08% for the measurement-series *M36-M40 (b)* 4.44% for the measurement-series *M26-M30*. Compared to the iteration errors of the measurement-series *M21-M25* and *M31-M35* with Wenner configuration, the iteration errors of the Dipole-Dipole configuration are strongly increased. Especially measurement *M37* has a high iteration error of 9.8%. This relatively high iteration error, compared to those of the Wenner configuration, may also be related to the occurrence of the negative phase angles.

8.2.1. Electromagnetic evaluation and soil temperature measurements

Due to the conspicuous spherical structures in the inversion models, especially in those of the Wenner configuration, an additional electromagnetic measurement was made. This is intended to rule out the possibility that there are larger metallic objects in these areas, which then cause these spherical areas with increased phase angles in the inversion models. These measurements were carried out with the *EM31*. The results obtained from the electromagnetic measurements are shown as graphs in *Figure 52* for the N-S and W-E profiles. The position of the gas dome is clearly visible in both graphs, namely where the horizontal and vertical readings become negative. In the area of the gas dome, both profiles show a strongly negative value for the horizontal dipole and no measured value at all for the vertical dipole. This is the case for both profiles at profile metre 25, as the profiles have been designed so that the gas dome is located in the middle of the profile. By using the vertical and the horizontal dipole, one obtains differentiated information about the examination depth, because with the vertical dipole one achieves an examination depth of up to 6m and with the horizontal dipole a depth of 3m. During the measurement, a three-dimensional ellipse is built up, which results in the different penetration depths for the vertical and the horizontal dipole. When measuring the profiles, a measurement was taken

every metre and the measured values were then entered per metre. This makes it easier to recognise the variations per metre. The electromagnetic measurement of the N-S profile shows a strong variation at profile metre 36, where the vertical dipole takes on a negative value whereas the horizontal dipole shows a positive peak. The W-E profile shows a small fluctuation next to the gas dome where the vertical dipole also shows a deviation from the horizontal dipole, even though there is no negative value. On the other hand, this profile shows a larger fluctuation with a negative value of the vertical dipole, but this is not a peak anomaly, but rather an elongated anomaly. However, there are no clear indications of further metallic objects, away from the gas dome, which could be located along the profile in the subsurface.

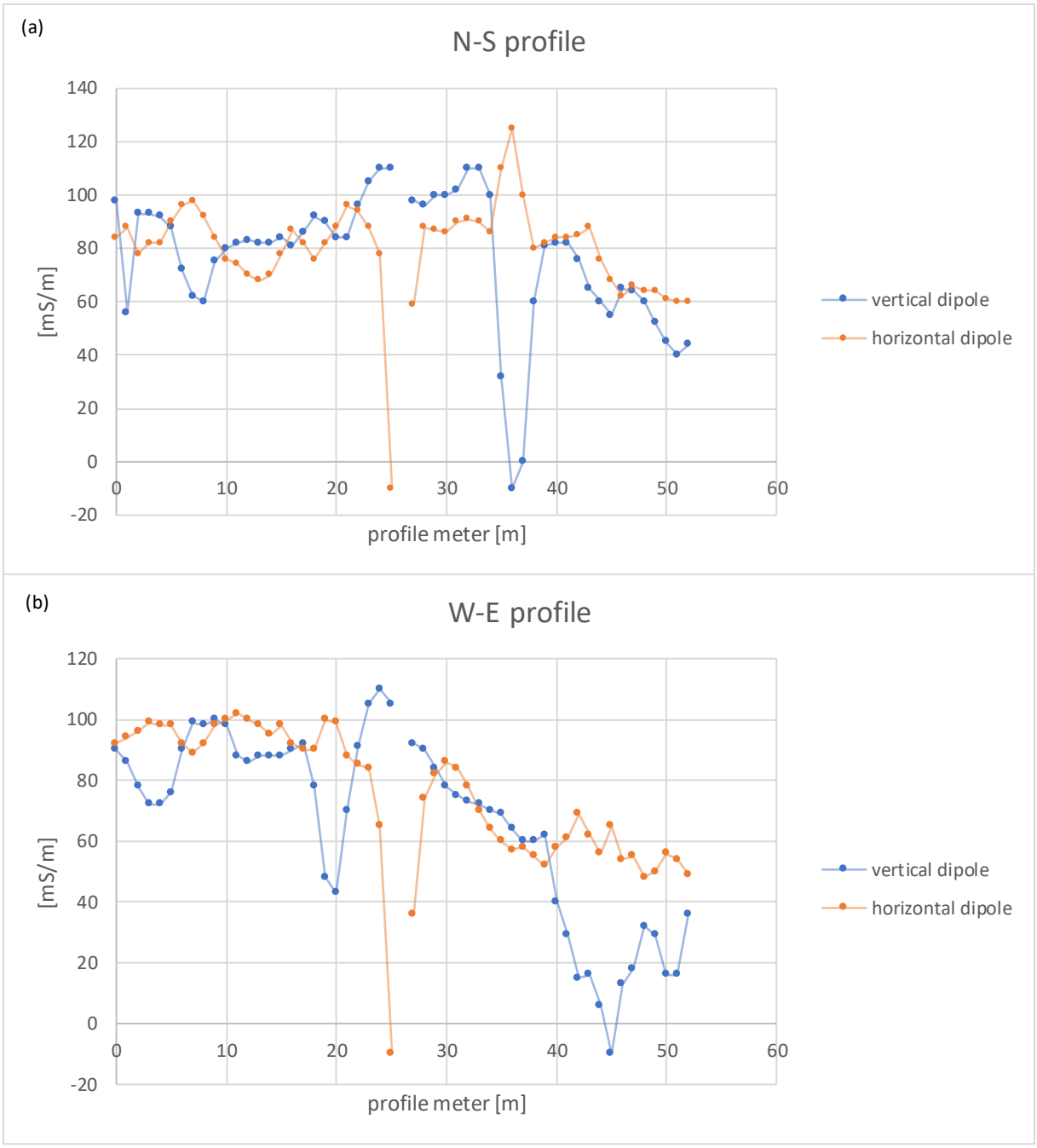

Figure 52: Shows the results of the electromagnetic measurement for the two profiles (a) N-S and (b) W-E, the vertical and the horizontal dipole are shown in each case.

For the two profiles N-S and W-E, additional soil temperature measurements were carried out since the soil temperature can also be an influencing factor on the conductivity of the subsurface. For this purpose, a measurement was carried out every ten meters along the profiles. The results obtained are shown in *Figure 53* for profiles *(a)* N-S and *(b)* W-E. Two different days were measured for each profile; these are indicated by different colours. The blue colour indicates measurements at an earlier time and the orange colour at a later time. The measurements in *Figure 53 (a)* for the N-S profile show a

good agreement and an almost identical course, but the temperatures recorded at a later time (orange colour) are slightly higher with a maximum of 12°C at the beginning of the profile. In the middle of the profile the temperatures are slightly lower, but there are no extreme temperature differences. The measurements in blue colour show a somewhat more inhomogeneous course, with temperature fluctuations up to 1.5°C. A slightly different picture is shown by the soil temperature measurements in *Figure 53 (b)* for the W-E profile: there is a temperature maximum at profile meter 20 and a subsequent flattening of the temperature curve towards the end of the profile with temperatures around 9.5°C.

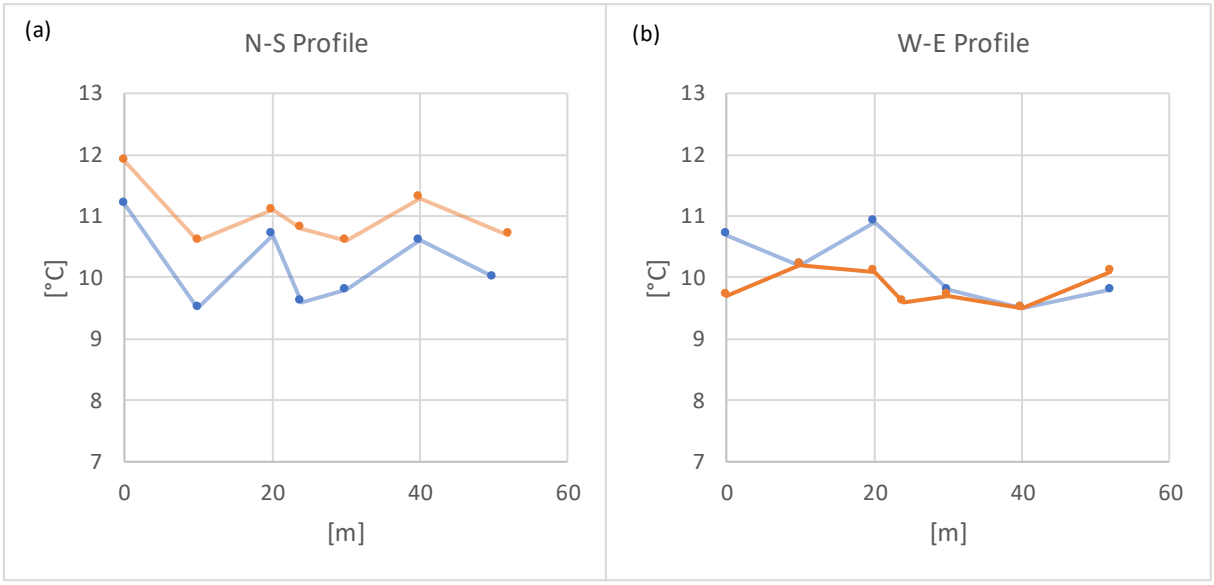

Figure 53: Comparison of the diagrams created from the results of the soil temperature measurements for (a) the N-S profile and (b) the W-E profile.

In general, the recorded temperature variations are within acceptable limits and therefore there is no need to focus specifically on these ground temperatures in further evaluation.

8.3. Measurements from November 2021

In November 2021, measurements were continued at the landfill in Allerheiligen in the Mürz valley. Due to a research project of the University of Natural Resources and Life Sciences in Vienna, the original gas dome of the measurements was removed in May 2021 and is therefore no longer available as an investigation target. Therefore, another gas dome in the immediate vicinity was chosen as the measurement target. In addition to the *4 point light 10W* measuring device from *Lippmann*, the *Mangusta System MC 24/144E* measuring device was now also available for measurements in the time-domain. During these measurement runs, three parallel profiles were drawn in the W-E direction at different distances from the gas dome. The aim was to see whether a change in the distance to the gas dome has an effect on the measurement results and whether this indicates the gas dome in the evaluations. In this test set-up, no N-S profile was deliberately drawn, as no directional dependence was shown in the measurements in the test set-up from May 2021. Due to damage to some of the non-polarisable electrodes, there was an increased loss of $CuSO_4$ into the subsurface, which meant that the $CuSO_4$ had to be refilled more often during the measurements. As a result, there were not enough non-polarisable electrodes available for an entire profile line. For this reason, only ten non-polarisable electrodes could be used. These were then used in profile Line 2 directly in the vicinity of the gas dome in order to be able to use the positive effect of the non-polarisable electrodes at least in this area, which is of greatest interest.

8.3.1. Lippmann 10W 4 point light

The analysis of the *Lippmann* measurements is done in the same way as for the measurement run in May 2021. Therefore, the statistical evaluation of the *dU90* values is started.

8.3.1.1. Statistical analysis of measurements with Lippmann 4 point light 10W – Line 3

It starts with the evaluation of the measurements of the Line 3 profile. Four measurements with different measuring frequencies were carried out for each configuration. The statistical evaluation of these two measurement-series is listed in *Table 27.* These are the measurement-series *B17*, *B18*, *B19* and *B24* which were measured with Wenner configuration and the measurement-series *B20-B24* which were measured with Dipole-Dipole configuration. Through this direct comparison of the two measurement-series, a clear comparison of the two configurations is achieved. On average, the individual statistical values of the recorded *dU90* values hardly differ from each other in the two measurement-series. There are no significant differences in the statistical evaluation of the *dU90* values for Line 3. In general, the four measurement frequencies 4.16Hz, 2.08Hz, 1.04Hz and 0.52Hz were measured. The measurement with the lowest possible measurement frequency of 0.28Hz was dispensed with because the evaluation of the measurement results of the measurement run from May

2021 showed that the measurement quality of the measurements with 0.52Hz is just as sufficient and is also much more time-saving.

When looking at the statistical evaluation of *Table 27*, it is noticeable that the maximum *dU90* for the two measurements *B17* and *B18* are below the 5% limit, while the lower-frequency measurements *B19* and *B24* show a very high level of just over 17% high maximum value of the *dU90* values. However, the median and the mean value for these two measurements are relatively low compared to the high maximum value, which means that 50% of the data are below the median value. Compared to this, the median of the measurement-series *B20-B23* is slightly increased. The maximum values of the *dU90* values are also all above the 5% threshold in the *B20-B24* measurement-series, although the deviation is also to be classified as very small here.

Table 27: Listing of the statistical evaluation of the dU90 values for the measurement-series B17, B18, B19 and B24 with Wenner configuration (left column) and the measurement-series B20-B23 with Dipole-Dipole configuration (right column). Both series were carried out with metal electrodes.

Line 3							
Wenner configuration				Dipole - Dipole configuration			
B17 dU90 [%] - 4.16Hz		B18 dU90 [%] - 2.08Hz		B20 dU90 [%] - 4.16Hz		B21 dU90 [%] - 2.08Hz	
min.:	0.016	min.:	0.007	min.:	0.025	min.:	0.023
max.:	4.819	max.:	4.859	max.:	7.872	max.:	9.244
mean value:	1.372	mean value:	1.377	mean value:	2.307	mean value:	2.451
median:	0.880	median:	1.013	median:	1.917	median:	1.874
standard deviation:	1.311	standard deviation:	1.208	standard deviation:	1.864	standard deviation:	1.786
variance:	1.740	variance:	1.477	variance:	3.517	variance:	3.229
B19 dU90 [%] - 1.04Hz		B24 dU90 [%] - 0.52Hz		B22 dU90 [%] - 1.04Hz		B23 dU90 [%] - 0.52Hz	
min.:	0.031	min.:	0.130	min.:	0.010	min.:	0.020
max.:	17.584	max.:	17.888	max.:	8.818	max.:	12.784
mean value:	2.939	mean value:	3.799	mean value:	2.917	mean value:	3.857
median:	2.473	median:	4.271	median:	2.880	median:	4.610
standard deviation:	2.929	standard deviation:	2.6108	standard deviation:	2.170	standard deviation:	1.849
variance:	8.682	variance:	6.899	variance:	4.765	variance:	3.461

The data from *Table 27* are shown in *Figure 54* as diagrams in which the *dU90* values are plotted against the *nr of measurement*. In addition to an overall compilation, there are also the individual diagrams broken down according to the individual measurement frequencies. It can be seen that for measurements *B17* and *B18* the *dU90* values are all below the 5% threshold. In contrast to this, the diagrams for the measurements *B19* and *B24* look a little different, since there 2 or 3 outlier values can be seen there, which occurred in both measurements with the same *nr of measurement*. This results in the high maximum values listed in *Table 27*. However, the remaining values in the two diagrams for *B19* and *B24* are also below the 5% values.

The diagrams created where the *dU90* values are plotted against the *nr of measurement* corresponding to the respective measurement frequencies are attached in the *electronic Appendix* and not listed in the body text, as the statistical evaluation of the *dU90* values turned out to be very moderate without any major outliers or discrepancies.

The analysis is continued with the interpretation of the phase angles: for this purpose, diagrams were again created in which the phase angles of the individual measurement frequencies are plotted against the lowest measurement frequency of 0.52Hz. These diagrams are shown in *Figure 54*. In addition, the regression lines and the coefficient of determination R^2 for each data cloud were added to get a better overview of the scatter and the fit of the model to the data points. When looking at the two diagrams in *Figure 54*, it is noticeable that the data cloud from the measurements with Wenner configuration appears less concentrated and more dispersed within itself. On the other hand, the scatter in the diagram of the Dipole-Dipole measurement seems to be smaller, although the maxima and minima values are further apart. This can also be seen in the scaling of the vertical axis, which shows an outlier value of up to 70mrad. The values of the equality measure are additionally listed in *Table 28* for the individual measurements, as these are difficult to recognise in *Figure 54*. It can be seen that the values for R^2 are lower on average for the measurement-series *B17-B19* than for the measurement-series *B20-B22*. This means that the scatter in the phase diagrams for the Dipole-Dipole measurements can be better explained by the generated regression model than for the data of the Wenner measurements. This shows a different behaviour of the values of the phase angles for the respective configurations than in the measurements in May 2021. At that time, a lower data scatter of the phase angles is consistently shown for the measurements with Wenner configuration, compared to those of the Dipole-Dipole configuration.

Table 28: Shows the coefficients of determination R2 for the measurement B17-B19 and B20-B22 which can be seen in Figure 53 (a) and (b).

Measurement	R^2	Measurement	R^2
B17	0.7123	B20	0.8088
B18	0.4593	B21	0.5275
B19	0.8011	B22	0.7940

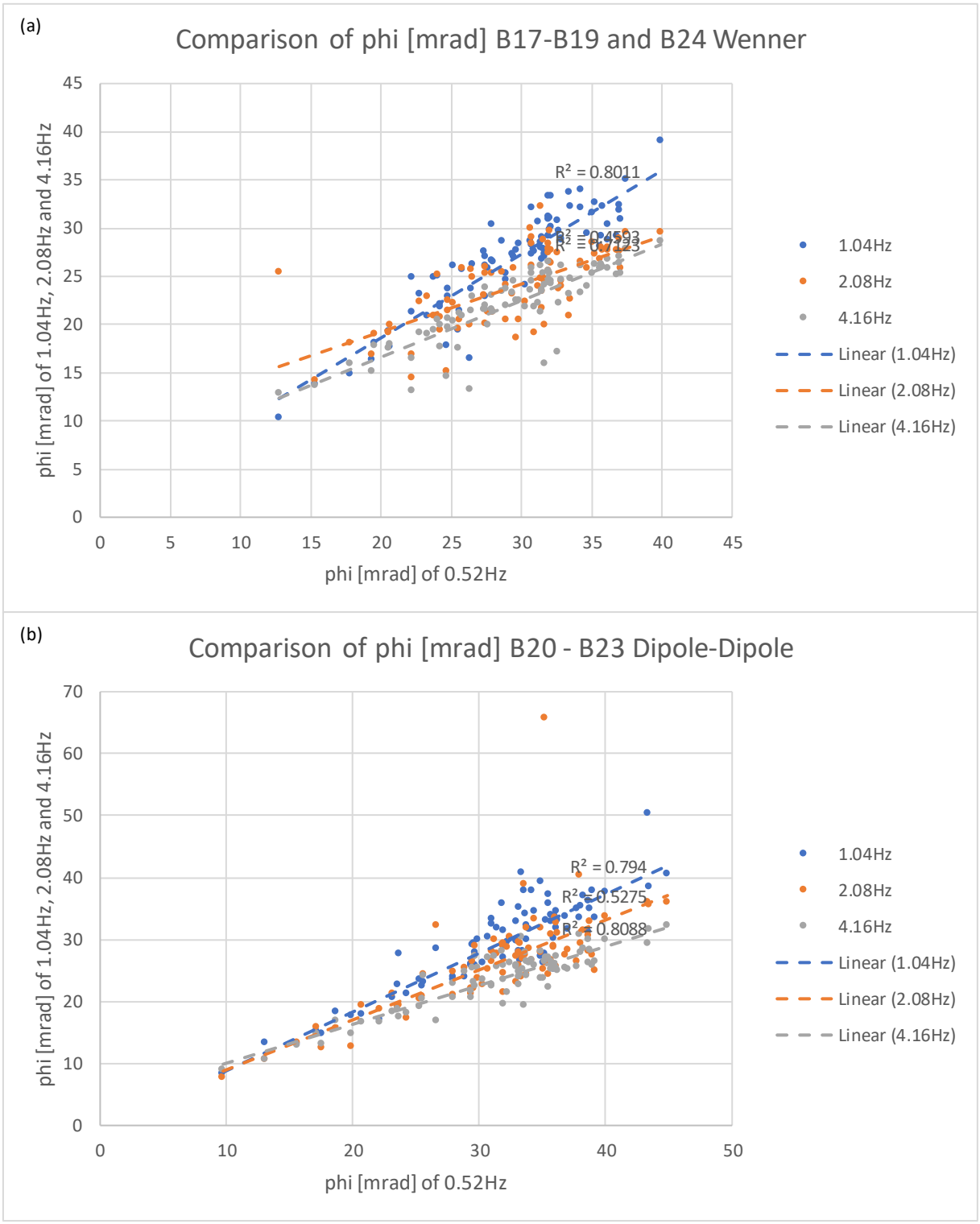

Figure 54: (a) Crossplot between the measurement at 0.52Hz against all other measurements at frequencies 4.16Hz, 2.08Hz and 1.04Hz for the measurement-series B17 – B19 and B24 using steel electrodes and with Wenner configuration. (b) Crossplot between the measurement with 0.52Hz against all other measurements at frequencies 4.16Hz, 2.08Hz and 1.04Hz for the measurement-series B20 – B23 using steel electrodes and with Dipole-Dipole configuration.

8.3.1.2. Statistical analyses of measurement with Lippmann 4 point light 10W – Line 1

Line 1 is placed exactly in the middle of Line 2 and Line 3 and thus runs at a distance of 1m from the gas dome in W-E direction. For Line 1, 48 electrodes were used for all measurements, i.e., twice as many as for Lines 2 and Line 3. This double number of electrodes should enable a higher resolution or more details in the inversion models. The distance between the electrodes is thus 1m, resulting in a total profile length of 48m. A total of six measurements were carried out along Line 1, which are divided into two measurement-series according to the measurement configuration used. The statistical evaluation of the *dU90* values for these two measurement-series is shown in *Table 29*.

Table 29: Listing of the statistical evaluation of the dU90 values for the measurement-series B25-B27 with Wenner configuration (left column) and the measurement-series B28-B30 with Dipole-Dipole configuration (right column). Both series were carried out with metal electrodes.

Line 1							
Wenner configuration				Dipole - Dipole configuration			
B25 dU90 [%] - 4.16Hz		B26 dU90 [%] - 2.08Hz		B28 dU90 [%] - 4.16Hz		B29 dU90 [%] - 2.08Hz	
min.:	0.013	min.:	0.003	min.:	0.007	min.:	0
max.:	24.444	max.:	23.754	max.:	12.806	max.:	63.527
mean value:	1.867	mean value:	2.106	mean value:	1.896	mean value:	2.598
median:	1.047	median:	1.324	median:	1.383	median:	1.909
standard deviation:	2.482	standard deviation:	2.274	standard deviation:	1.672	standard deviation:	3.834
variance:	6.176	variance:	5.185	variance:	2.804	variance:	14.739

B27 dU90 [%] - 1.04Hz	
min.:	0.008
max.:	77.45
mean value:	4.688
median:	4.169
standard deviation:	8.098
variance:	65.766

B30 dU90 [%] - 1.04Hz	
min.:	0.019
max.:	526.75
mean value:	7.197
median:	3.748
standard deviation:	36.75
variance:	1354.3

Only the following three measurement frequencies were used for these measurement-series: 4.16Hz, 2.08Hz and 1.04Hz. The use of 48 electrodes results in longer measurement times, which are significantly longer at particularly low measurement frequencies. Due to these facts, the two lowest frequencies 0.26Hz and 0.52Hz were not used, as this would extremely increase the measuring times and would not pay off in terms of time and costs.

When looking at the statistical evaluation of the measurement-series *B25-B27*, which was measured with Wenner configuration, it is noticeable that the maximum values of the *dU90* values are clearly increased for all three measurements compared to the evaluations of Line 1. However, the mean value and also the median are within an acceptable range for all these measurements, especially for the measurements *B25* and *B26* these values are very low. A similar picture emerges with the measurement-series *B28-B30*, which were carried out with Dipole-Dipole configuration.

In this measurement-series, the maximum values are also strongly increased, also compared to the statistical evaluations of Line 3. Especially the maximum value of measurement *B30* is strongly increased. However, the median is relatively low for all measurements of the measurement-series *B28-B30* compared to the maximum values. This means that 50% of the data is below this value, which has a positive effect especially when considering the *dU90* values, as this is a parameter that can provide information about the measurement quality. When comparing the *dU90* values against the *nr of measurement*, diagrams were again generated showing that by far the majority of the measured values lie within an acceptable range, i.e., virtually below the 5% threshold. Individual outlier values are responsible for the high maximum values in the statistical evaluation. These diagrams can be found in the *electronic Appendix*.

In addition to the statistical evaluation of the *dU90* values, the phase angles are analysed. The diagrams generated are shown in *Figure 51* for the two measurement-series. Both for the measurements with the Wenner configuration and for the measurements with the Dipole-Dipole configuration, the majority of the data points are between 10 and 40mrad. In the measurement-series *B25-B27*, a single outlier value of the measurement at 2.08Hz slightly increases the scaling of the vertical axis. However, there are no negative values and no values >100mrad in this series of measurements. In the measurement-series *B28-B30*, which were carried out with a Dipole-Dipole configuration, a negative value occurs, which can be interpreted as an incorrect measurement. This measurement-series also shows a single outlier value for the measurement with 2.08Hz, but this outlier value is also within an acceptable range, just like in the measurement-series *B25-B27*.

In addition to the regression line, the coefficient of determination R^2 was also shown in both diagrams and listed again in *Table 30*. The measurement *B26* with 2.08Hz is clearly out of line with a coefficient of determination of only 0.421. This can also be seen in *Figure 55 (a)*, since the data cloud shows a much greater scatter around the regression line than that of measurement *B25*. The coefficients of determination for measurement *B28-B29* are higher, implying a better explanation of the regression models, although there is one negative data point in this series.

Table 30: Shows the coefficients of determination R2 for the measurement B25-B26 and B28-B29 which can be seen in Figure 54 (a) and Figure 54 (b).

Measurement	R^2	Measurement	R^2
B25	0.8422	B28	0.8616
B26	0.421	B29	0.7088

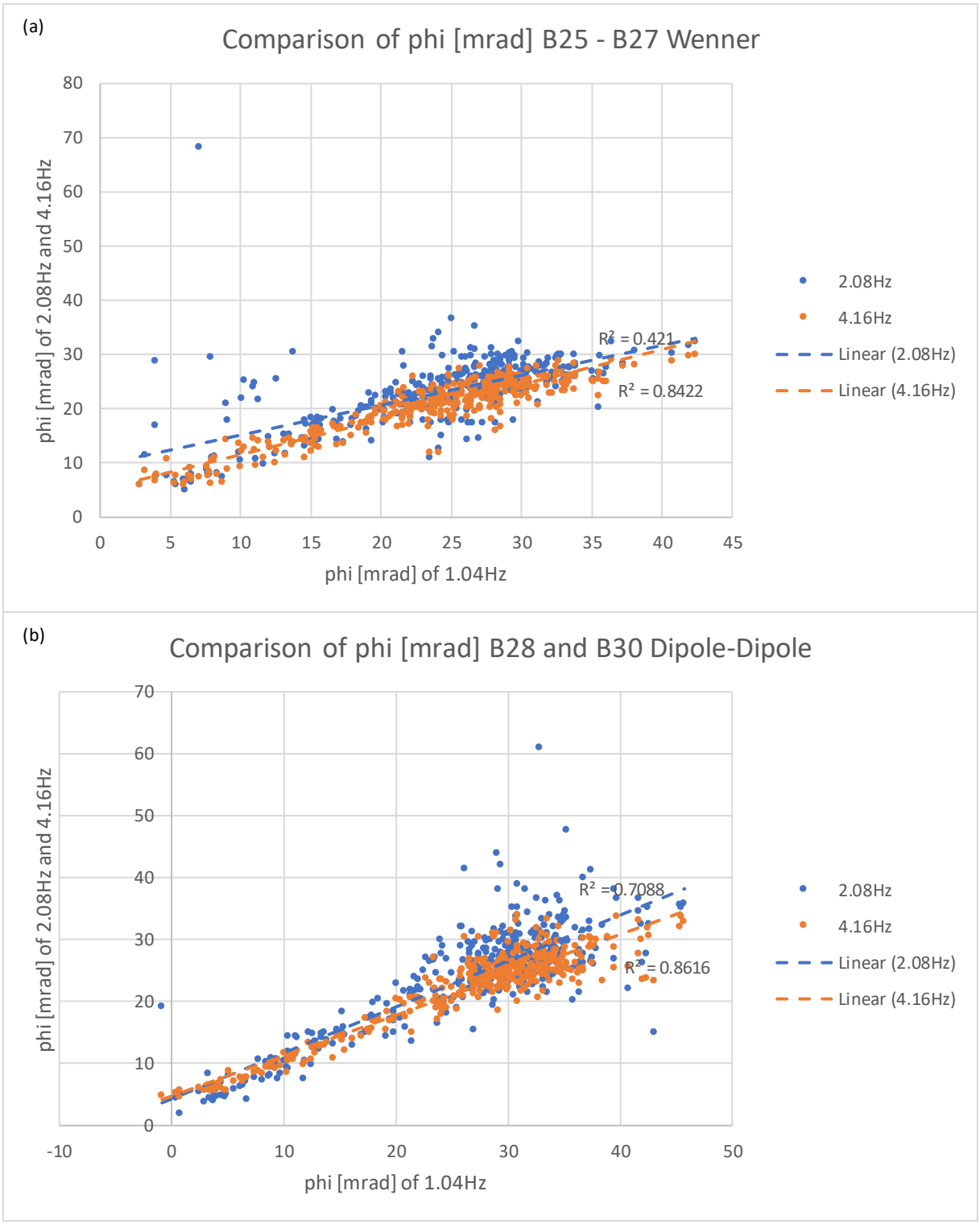

Figure 55: (a) Crossplot between the measurement at 1.04Hz against all other measurements at frequencies 4.16Hz and 2.08Hz for the measurement-series B25-B27 using steel electrodes and with Wenner configuration. (b) Crossplot between the measurement at 1.04Hz against all other measurements at frequencies 4.16Hz and 2.08Hz for the measurement-series B28-B30 using steel electrodes and with Dipole-Dipole configuration.

8.3.1.3. Statistical analysis of measurements with Lippmann 4 point light 10W – Line 2

Line 2 runs exactly through the gas dome, which is again located in the middle of the profile. An electrode was placed before and after the gas dome in W-E orientation. This resulted in a general electrode spacing of 2m and with 24 electrodes used, a total profile length of 48m.

Along Line 2, a total of four measurement-series with four measurements each were carried out, i.e., a total of 16 individual measurements. These differ in the measurement frequency, the measurement configuration and the type of electrode. The measurement-series *B1-B3* and *B8* and the measurement-series *B4-B7* were measured with steel electrodes. As only ten non-polarisable electrodes were available due to damage, the entire profile could not be measured with them. For this reason, the middle ten steel electrodes were replaced by the remaining non-polarisable electrodes for measurement-series *B9-B11* and *B16* as well as for measurement-series *B12-B15*.

A statistical evaluation of the *dU90* values was also carried out for Line 2. The listing of this evaluation is presented in *Table 31*.

Some of the maximum values are quite high, whereby these are significantly higher in the measurement-series with Dipole-Dipole configuration. In general, measurements with the two higher frequencies of 4.18Hz and 2.08Hz tend to show lower maximum values than the low-frequency measurements. This trend can be seen both in the measurements with all steel electrodes and in those measurements where non-polarisable electrodes were also used. Another discernible trend is that the mean and median are slightly higher for the 1.04Hz and 0.52Hz measurements compared to the higher frequency measurements. However, almost all measurements are below the known 5% threshold and only measurement *B3*, *B7* and *B14* are an exception, although the values obtained there are also not drastically increased. A clear difference between the series of measurements carried out purely with metallic electrodes and those carried out additionally with non-polarisable electrodes cannot be recognised. The fluctuations in the data of *Table 31* are too unclear to be able to make such a statement. Compared to the measurements with the Lippmann *4 point light 10W*, which were carried out during the measurements in May 2021, differences are noticeable: during the measurements in May 2021, it is noticeable that the maximum values are significantly higher for those measurements that were carried out with the Dipole-Dipole configuration compared to those with the Wenner configuration.

Table 31: Listing of the statistical evaluation of the dU90 values for the four different measurement-series. In the left column are the two measurement-series listed which were done with Wenner configuration and in the right column are the ones which were measured with Dipole-Dipole configuration. The bottom part of this table is filled with the statistical analysis for the measurement-series which are done with the additional non polarizable electrodes.

Line 2							
Wenner configuration - steel electrodes				Dipol-Dipol configuration - steel electrodes			
B1 dU90 [%] - 4.16Hz		B2 dU90 [%] - 2.08Hz		B4 dU90 [%] - 4.16Hz		B5 dU90 [%] - 2.08Hz	
min.:	0.018	min.:	0.005	min.:	0.043	min.:	0.068
max.:	4.836	max.:	5.281	max.:	6.790	max.:	39.657
mean value:	0.9027	mean value:	1.8749	mean value:	2.2267	mean value:	2.8162
median:	0.449	median:	1.532	median:	1.5035	median:	1.778
standard deviation:	1.1451	standard deviation:	1.4641	standard deviation:	1.9208	standard deviation:	4.4323
variance:	1.3271	variance:	2.1693	variance:	3.7341	variance:	19.882
B3 dU90 [%] - 1.04Hz		B8 dU90 [%] - 0.52Hz		B6 dU90 [%] - 1.04Hz		B7 dU90 [%] - 0.52Hz	
min.:	0.024	min.:	0.021	min.:	0.069	min.:	0.110
max.:	462.97	max.:	13.40	max.:	72.45	max.:	232.75
mean value:	8.3917	mean value:	4.1415	mean value:	4.339	mean value:	6.544
median:	2.170	median:	4.638	median:	4.4945	median:	4.5935
standard deviation:	50.279	standard deviation:	2.6413	standard deviation:	7.7559	standard deviation:	25.186
variance:	2558.8	variance:	7.0606	variance:	60.879	variance:	642.18
Wenner configuration - non polarisable electrodes				Dipol-Dipol configuration - non polarisable electrodes			
B9 dU90 [%] - 4.16Hz		B10 dU90 [%] - 2.08Hz		B12 dU90 [%] - 4.16Hz		B13 dU90 [%] - 2.08Hz	
min.:	0	min.:	0.014	min.:	0.117	min.:	0
max.:	4.940	max.:	4.952	max.:	13.612	max.:	17.305
mean value:	1.1889	mean value:	1.0066	mean value:	3.5834	mean value:	2.325
median:	0.689	median:	0.6345	median:	2.8955	median:	1.5595
standard deviation:	1.1844	standard deviation:	1.0244	standard deviation:	3.2572	standard deviation:	2.3539
variance:	1.420	variance:	1.062	variance:	10.737	variance:	5.6075
B11 dU90 [%] 1.04Hz		B16 dU90 [%] - 0.52Hz		B14 dU90 [%] - 1.04Hz		B15 dU90 [%] - 0.52Hz	
min.:	0.028	min.:	0.183	min.:	0.018	min.:	0.214
max.:	54.559	max:.	31.074	max.:	149.6	max.:	1623.7
mean value:	4.5475	mean value:	4.180	mean value:	5.4083	mean value:	22.95
median:	4.4855	median:	4.5835	median:	4.1935	median:	4.4445
standard deviation:	7.5843	standard deviation:	3.9273	standard deviation:	16.135	standard deviation:	175.71
variance:	58.215	variance:	15.61	variance:	263.49	variance:	31248

Then the distribution of the phase angles was examined. Diagrams were created for this, which are shown in *Figure 56* for the four measurement-series. The regression lines and the coefficient of determination are also shown in the figures. For a better overview, the individual coefficients of determination for the respective measurement frequencies for each measurement are listed separately in *Table 32*. A similar picture emerges for the two series of measurements with the Wenner configuration: there are no negative phase angles and the data clouds are between >0mrad and <50mrad. A direct comparison of the two series of measurements with the Wenner configuration shows that the values of the coefficients of determination in the series of measurements with the ten

non-polarizable electrodes are slightly higher than in the series of measurements where only metallic electrodes were used.

The two series of measurements with a Dipole-Dipole configuration also show similarities: isolated negative phase angles occur in each case. Most of the data lies between slightly smaller than 0mrad and <60mrad. The series of measurements with the Dipole-Dipole configuration do not show any higher coefficients of determination for the measurements where the non-polarizable electrodes were also used.

Table 32: Shows the coefficients of determination R^2 for the four measurement-series which can be seen in Figure 55 (a)-(d).

Measurement	R^2	Measurement	R^2
B1	0.7951	B9	0.8124
B2	0.5379	B10	0.688
B3	0.8582	B11	0.8421
B4	0.8471	B12	0.7996
B5	0.7372	B13	0.5725
B6	0.8489	B14	0.8146

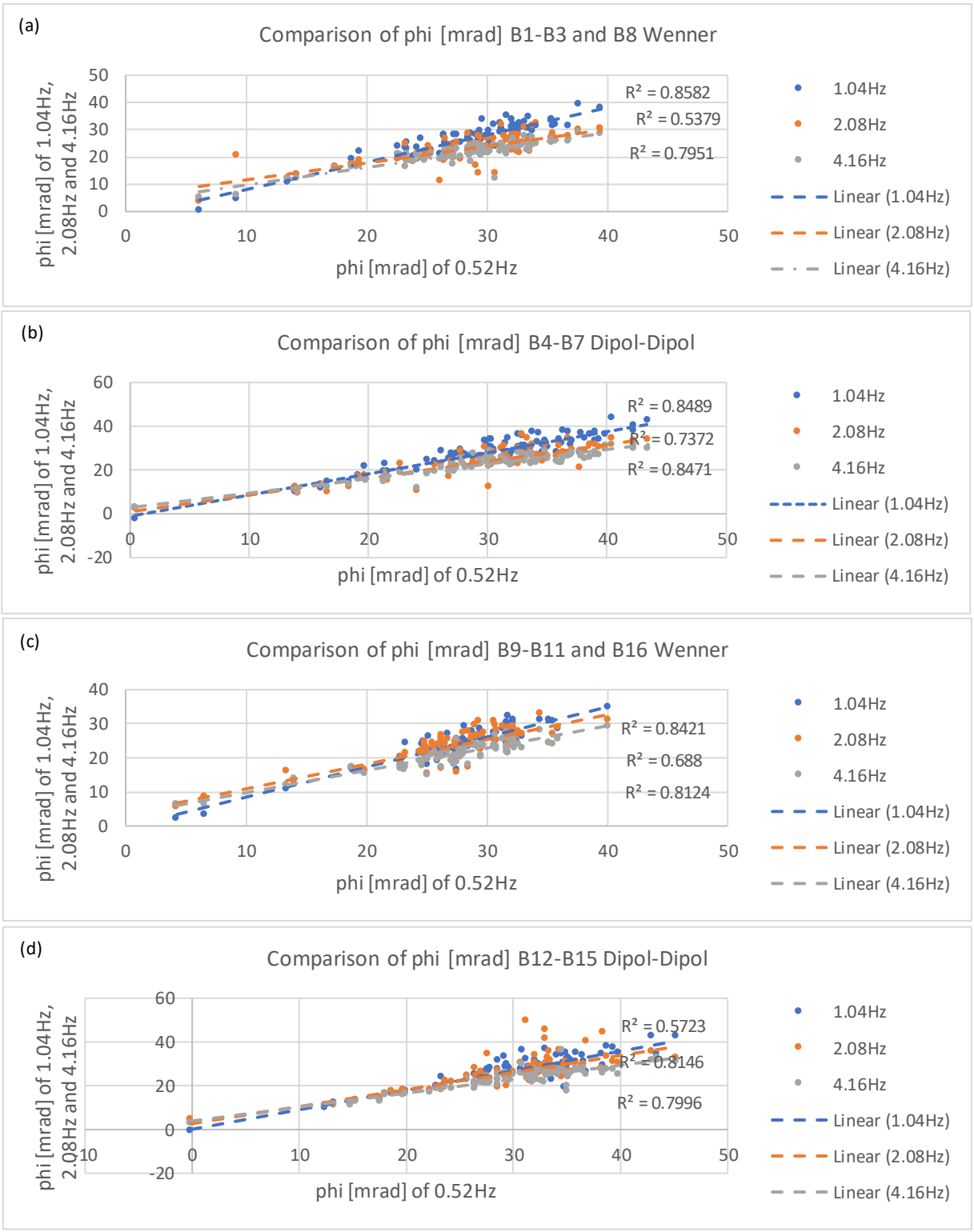

Figure 56: (a) Crossplot between the measurement at 0.52Hz against all other measurements at frequencies 4.16Hz, 2.08Hz and 1.04Hz for the measurement-series B1-B3 and B8 using steel electrodes and with Wenner configuration. (b) Crossplot between the measurement at 0.52Hz against all other measurements at frequencies 4.16Hz, 2.08Hz and 1.04Hz for the measurement-series B4-B7 using steel electrodes and with Dipole-Dipole configuration. (c) Crossplot between the measurement at 0.52Hz against all other measurements at frequencies 4.16Hz, 2.08Hz and 1.04Hz for the measurement-series B9-B11 and B16 using steel electrodes and non-polarisable electrodes with Wenner configuration. (d) Crossplot between the measurement at 0.52Hz against all other measurements at frequencies 4.16Hz, 2.08Hz and 1.04Hz for the measurement-series B12-B15 using steel electrodes and with Dipole-Dipole configuration.

8.3.1.4. Inversion of W-E profiles from November 2021 – Lippmann 4 point light 10W

In the inversions carried out, the inversion models of the individual lines are compared with each other, but only the inversion models of the IP measurements including the associated pseudo sections of the measured and calculated values are compared. The inversion models of the resistance values that were also generated are included in the *electronic Appendix*.

Line 3

The comparison of the inversions for Line 3, which is furthest away from the gas dome, begins. Here the gas dome is about 2m offset in the middle of the profile. *Table 33* lists the individual measurements together with the designation, measurement configuration, frequency and iteration error after four iteration steps.

Table 33: List of the measurement configuration and the used frequency as well as the iteration error after four steps of iteration for eight measurements done with Wenner and Dipole-Dipole configuration.

Measurement	Configuration	Electrodes	Frequency [Hz]	Iteration error [%]
B17	Wenner	24	4.16Hz	1.8
B18	Wenner	24	2.08Hz	2.2
B19	Wenner	24	1.04Hz	2.3
B24	Wenner	24	0.52Hz	2.3
B20	Dipole-Dipole	24	4.18Hz	1.7
B21	Dipole-Dipole	24	2.08Hz	2.7
B22	Dipole-Dipole	24	1.04Hz	2.4
B23	Dipole-Dipole	24	0.52Hz	2.0

Figure 57 shows all generated inversion models for the Line 3 series of measurements, listed in two columns, with the measurements with the Wenner configuration being listed on the left and the measurements with the Dipole-Dipole configuration being listed on the right. The inversion models in *Figure 57* show similar structures overall: shallow zones with very low phase angles can be seen near the surface, these are particularly evident in the middle of the profile and in the eastern area. In general, all inversion models show somewhat lower phase angles in the center of the profile than in the eastern and western profile areas. The higher frequency measurements with 4.16Hz and 2.08Hz show basically lower phase angles, between 12.8mrad and 32.9mrad. In contrast, the low frequency measurements show higher phase angles, between 24.0mrad and 45.0mrad, see *Figure 57 (d)* and *(h)*. Although measurements *57 (e)* through *(h)* were made with Dipole-Dipole configuration, no deratally perturbed models show up as in *Figure 51*, of the W-E profile measured in May 2021. The inversion models of measurements pictured in *Figure 57* show relatively small differences in the pseudo sections of the measured and the calculated values. This is also reflected in the relatively small iteration errors:

The iteration errors of the measurement-series are generally very low and indicate good data quality. There is an average iteration error for the measurement-series *B17-B19* and *B24* of 2.15% after four iteration steps and 2.20% for the measurement-series *B20-B23*. Thus, the iteration error for the series of measurements with Dipole-Dipole configuration is somewhat higher, but not by much.

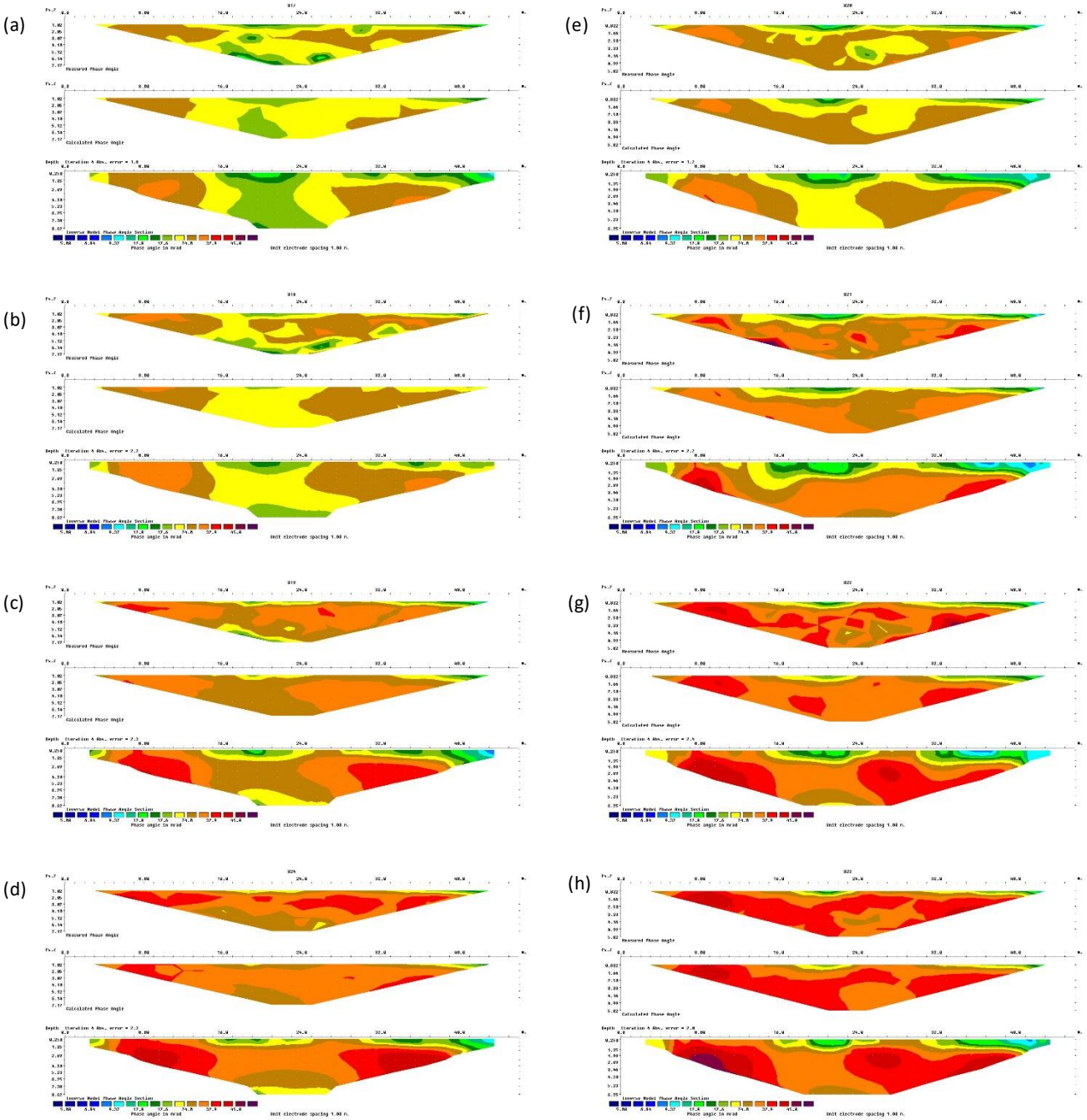

Figure 57: Shows the inversion of the measurement-series B17 (a), B18 (b), B19 (c) and B24 (d) with Wenner configuration (left column) and B20 (e), B21 (f), B22 (g) and B23 (h) with Dipole-Dipole configuration (right column). Further information about the measurement frequency of the single measurements is listed in Table 33.

Line 1

For Line 1, 48 electrodes were used with a distance of 1m to each other. The entire Line 1 is at a distance of 1m from the gas dome, which in turn is located in the middle of the profile. Due to the 48 electrodes and the reduced electrode spacing, a higher level of detail is expected in the inversion models. *Table 34* lists the individual measurements together with the designation, measurement configuration, frequency and iteration error after four iteration steps.

Table 34: List of the measurement configuration and the used frequency as well as the iteration error after four steps of iteration for the six measurements done with Wenner and Dipole-Dipole configuration.

Measurement	Configuration	Electrodes	Frequency [Hz]	Iteration error [%]
B25	Wenner	48	4.16	1.3
B26	Wenner	48	2.08	2.5
B27	Wenner	48	1.04	1.8
B28	Dipole-Dipole	48	4.16	1.3
B29	Dipole-Dipole	48	2.08	2.3
B30	Dipole-Dipole	48	1.04	2.1

These inversion models are shown in *Figure 58*: here the measurement-series *B25-B27* with Wenner configuration is shown in the left column and the measurement-series *B28-B30* with Dipole-Dipole configuration in the right column. The measurement frequencies are arranged one below the other from 4.16Hz to 1.04Hz. The average iteration error of the measurement-series *B25-B27* is 1.87% after four iterations and 1.90% for the measurement-series *B28-B30*. The difference in the average iteration error between the Wenner and Dipole-Dipole configuration can therefore be classified as negligible. The inversion models in *Figure 58* show similar structures: a shallow near-surface zone with very low phase angles around 5.00mrad extends from profile center to the eastern end of the profile. This results in a similar picture as with Line 3, however, for example, this zone near the surface with a low phase angle is stretched a little further than in Line 3. In the center of the profile, a band with lower phase angles extends to greater depths of investigation, while this zone is bordered by higher phase angles to the east and west, characterized by reddish colours. The *B25-B27* series of measurements with Wenner configuration shows an already known trend: the low-frequency measurement, *Figure 58 (c)*, has higher phase angles than the inversion models of the two higher-frequency measurements, *Figure 58 (a)* and *(b)*. The measurement *B30*, see *Figure 58 (f)*, is out of the ordinary, showing phase angles between 12.8 and 17.6mrad for the most part. Only in the western profile area is there a zone with up to 45.0mrad, which is comparable to the other measurements.

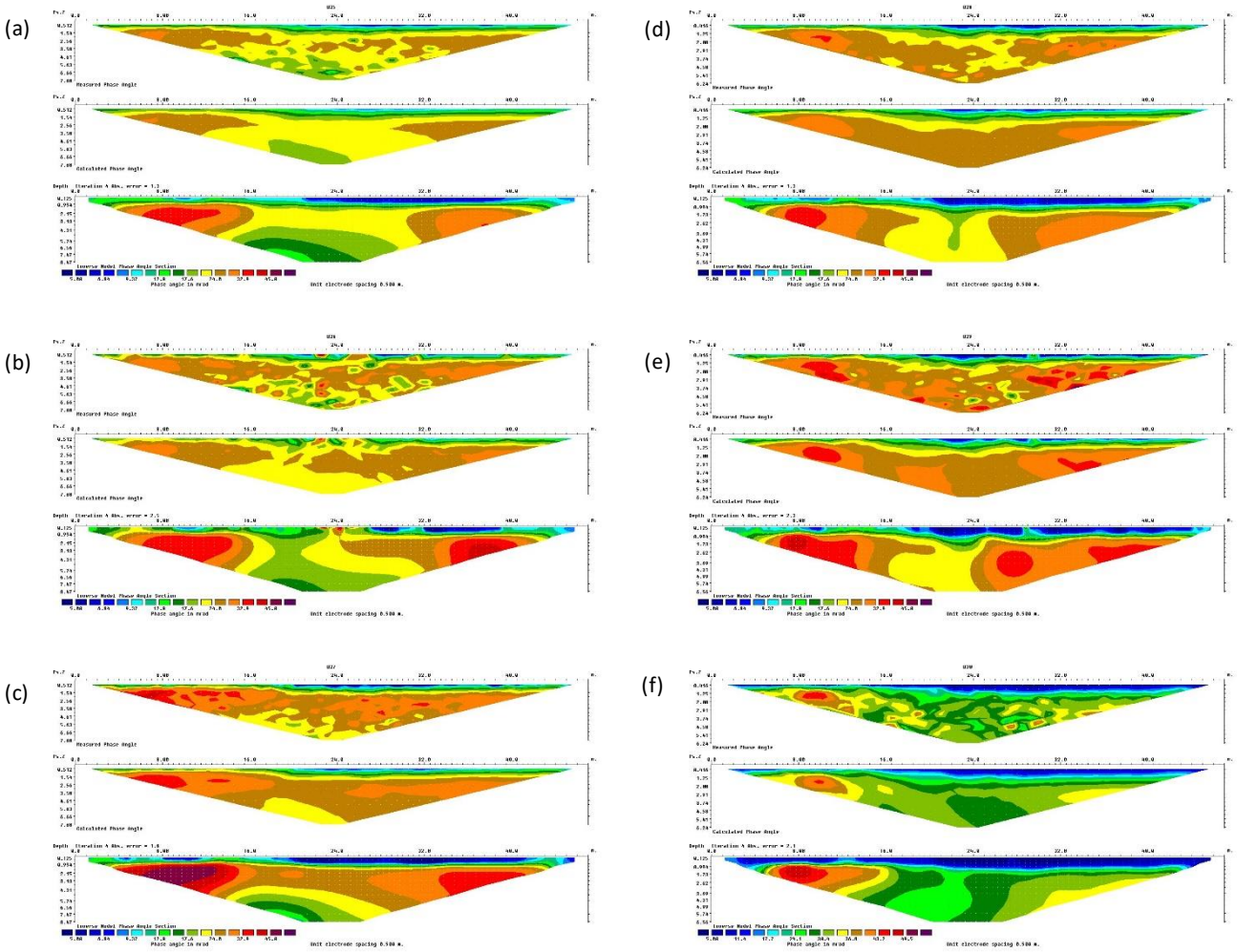

Figure 58: Shows the inversion of the measurement-series B25 (a), B26 (b) and B27(c) with Wenner configuration (left column) and B28 (d), B29 (e) and B30 (f) with Dipole-Dipole configuration (right column). Further information about the measurement frequency of the single measurements is listed in Table 34.

When looking at the pseudo sections of the measured values of the individual measurements (top) one can see a strongly mixed pattern of the measured phase angles, which can be seen from the rapidly changing colours, which are distributed in patches. This can be seen in the measurements in the Wenner as well as in the Dipole-Dipole configuration. Compared to this, the structures in the pseudo sections of the calculated values are smoothed and do not show such a diffuse distribution as in the pseudo sections of the measured values.

Despite the various discernible structures, none suggests the presence of the gas dome.

Line 2

Line 2 runs exactly through the gas dome and was the only one of the three parallel measurement lines that was also carried out with non-polarisable electrodes. In Line 2, 2m electrode spacing was selected, resulting in a maximum profile length of 48m. The names of the individual measurements, including the associated measurement configuration and measurement frequencies, and the iteration errors after four iteration steps are listed in *Table 35*. This creates a better overview of all measurements.

Table 35: List of the measurement configuration and the used frequency as well as the iteration error after four steps of iteration for the 16 measurements done with Wenner and Dipole-Dipole configuration.

Measurement	Configuration	Electrodes	Frequency [Hz]	Iteration error [%]
B1	Wenner	24	4.16Hz	1.7
B2	Wenner	24	2.08Hz	2.3
B3	Wenner	24	1.04Hz	2.4
B8	Wenner	24	0.52Hz	2.1
B9	Wenner	24	4.18Hz	1.6
B10	Wenner	24	2.08Hz	1.9
B11	Wenner	24	1.04Hz	1.7
B16	Wenner	24	0.52Hz	1.8
B4	Dipole-Dipole	24	4.16	1.5
B5	Dipole-Dipole	24	2.08	1.9
B6	Dipole-Dipole	24	1.04	2.0
B7	Dipole-Dipole	24	0.52	1.8
B12	Dipole-Dipole	24	4.16	1.6
B13	Dipole-Dipole	24	2.08	3.0
B14	Dipole-Dipole	24	1.04	2.0
B15	Dipole-Dipole	24	0.52	1.5

Figure 59 lists the two Wenner measurement-series from Line 2. The series of measurements *B1-B3* and *B8* forms the left column: this series of measurements was carried out with the Wenner configuration and exclusively with steel electrodes. The right-hand column shows the series of measurements *B9-B11* and *B16*, which were carried out with the Wenner configuration and in which the ten middle steel electrodes were replaced by non-polarizable electrodes. For the two series of measurements shown in *Figure 59*, the average iteration errors were calculated after four iteration steps: this results in an error of 2.125% for the series of measurements *B1-B3* and *B8*, which were measured purely with steel electrodes. For the measurement-series *B9-B11* and *B16* there is an error of 1.75%. In general, all these inversions indicate a relatively small iteration error. When looking at the inversion models in *Figure 59*, one can see the strong similarity of the measurements that were measured with the same measuring frequency. In general, a similar picture emerges as for Lines 1 and Line 3: in the middle of the profile there is an area with lower phase angles compared to the edges of the profile. There is again a near-surface, very shallow zone with very low phase angles. This is in the

middle of the profile, just like Line 1 and Line 3, but is much less dominant than, for example, in Line 1, where the lateral extent of this zone is much more pronounced.

Two more measurement-series were measured with identical measurement settings, but with a Dipole-Dipole configuration. These are the series of measurements *B4-B7* and *B12-B15*, with the ten middle electrodes of the latter being replaced by non-polarizable electrodes. The resulting inversion models are listed in *Figure 60*. The illustrations on the left belong to the measurement-series *B4-B7*: these were measured purely with metallic electrodes. The inversions of the measurement-series *B12-B15* are listed on the right. The four measurement frequencies used are listed as follows: starting with 4.16Hz (top) and ending at 0.52Hz (bottom). The average iteration error after four iteration steps is 1.8% for measurement-series *B4-B7* and 2.025% for measurement-series *B12-B15*. Thus, no trend can be recognized since the iteration errors for the measurements with Wenner and Dipole-Dipole are very similar, and no clear difference can be seen. The same applies to the measurements using the non-polarisable electrodes compared to those measurements using only metallic electrodes. No trend can be identified for this either, i.e., no advantage or disadvantage can be identified in the use of ten non-polarisable electrodes. When looking at the inversion models in *Figure 60*, a very similar picture emerges as in *Figure 59*. The pseudo sections for all measurements of these two measurement-series look very similar, which additionally underpins the high data quality, which is already confirmed by the low iteration errors. The inversion models, on the other hand, all show very similar structures, namely that in the middle of the profile there is an area with slightly lower phase angles compared to the edges. On the surface, exactly in the centre of the profile, there is again a very shallow zone with particularly low phase angles. However, the lateral extent of this zone is very limited, especially for the higher-frequency measurements.

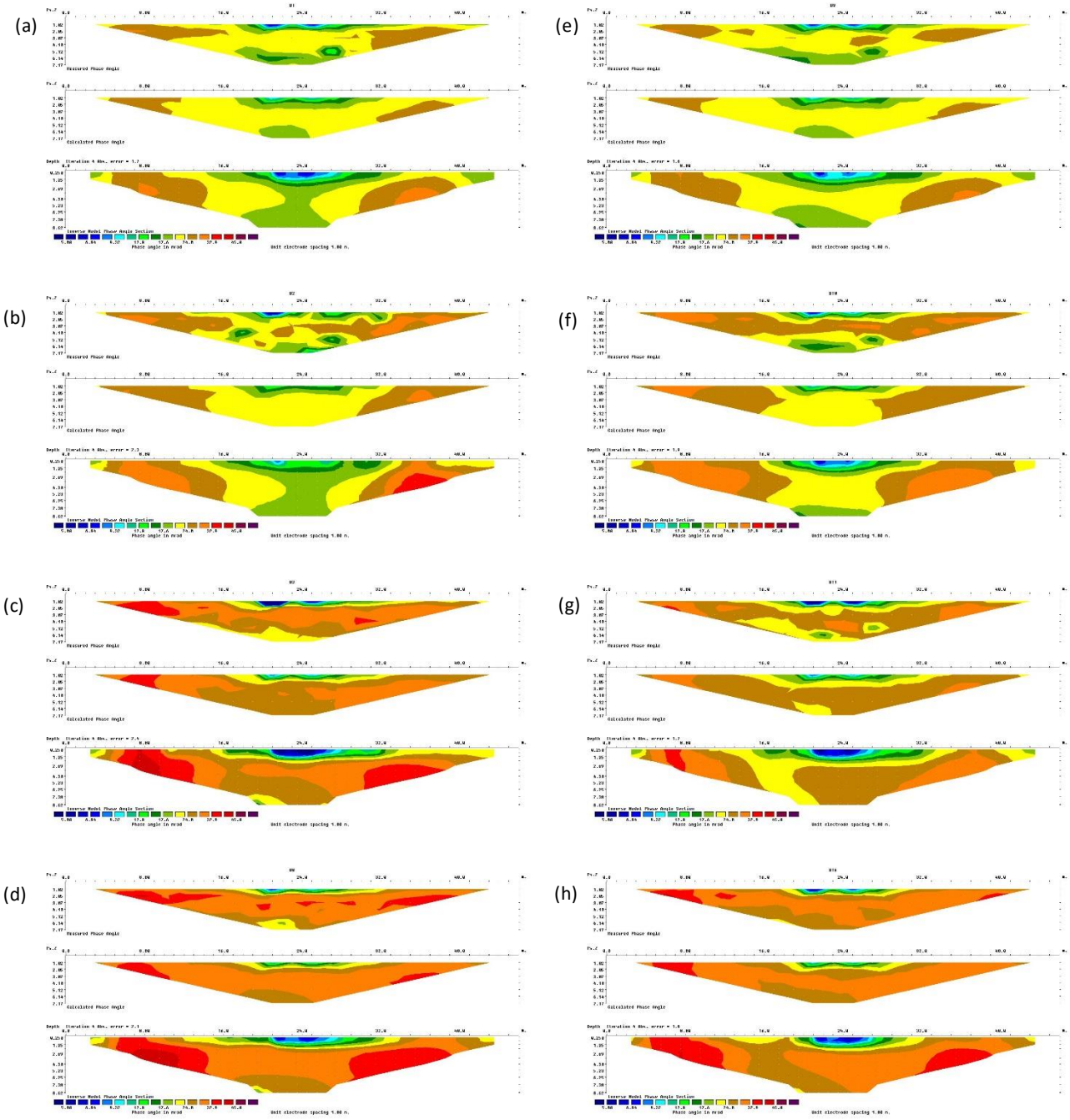

Figure 59: Shows the inversion of the measurement-series B1 (a), B2 (b), B3 (c) und B8 (d) with Wenner configuration and all metal electrodes (left column) and B9 (e), B10 (f), B11 (g) and B16 (h) with Wenner configuration and with ten non-polarisable electrodes (right column). Further information about the measurement frequency of the single measurements is listed in Table 35.

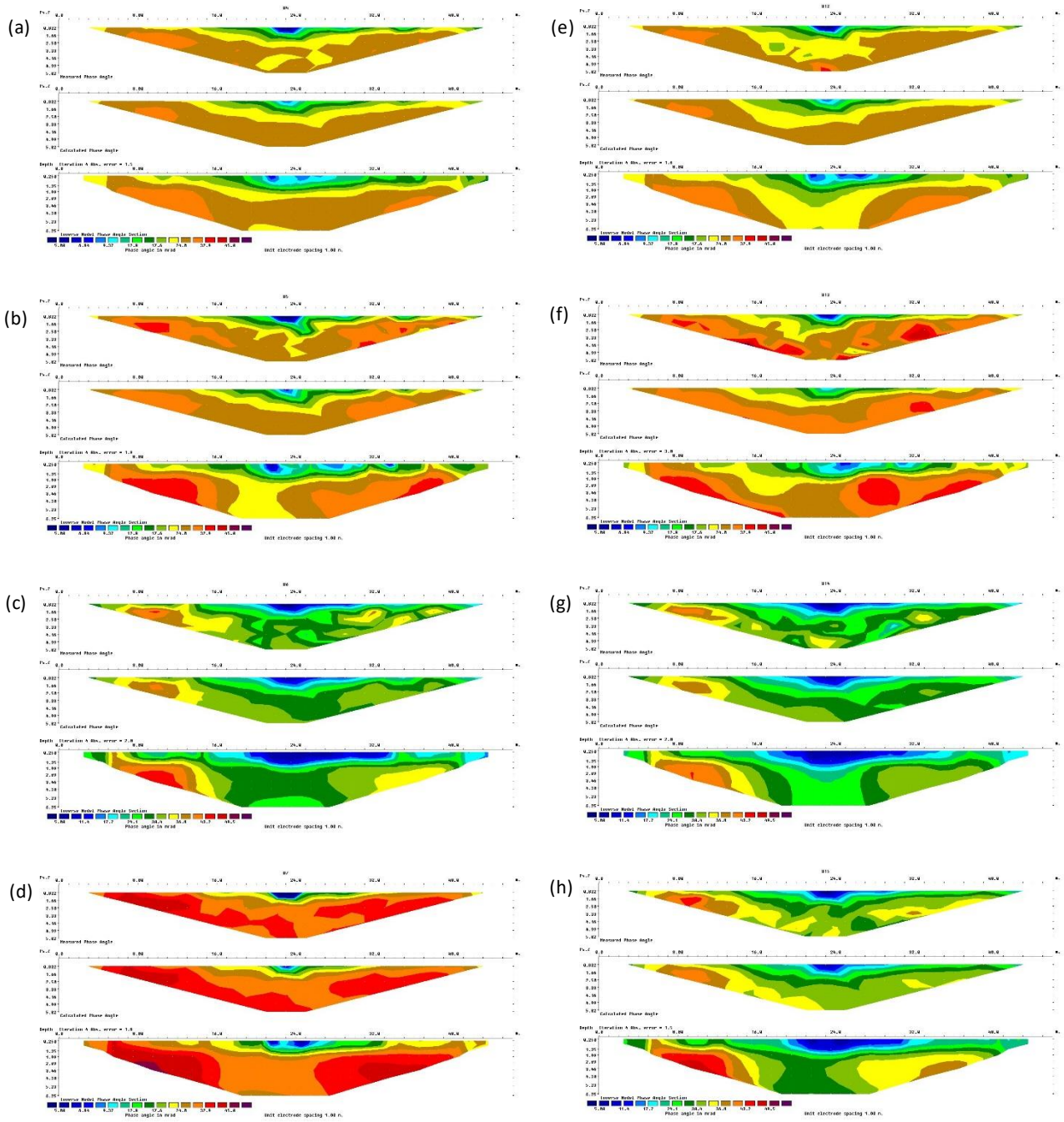

Figure 60: Shows the inversion of the measurement-series B4 (a), B5 (b), B6 (c) and B7 (d) with Dipole-Dipole configuration and all metal electrodes (left column) and B12 (e), B13 (f), B14 (g) and B15 (h) with Dipole-Dipole configuration and with ten non-polarisable electrodes (right column). Further information about the measurement frequency of the single measurements is listed in Table 35.

8.3.2. Mangusta System MC 24/144E

In addition, the profiles Line 1, Line 2 and Line 3 were also measured with the *Mangusta System MC 24/144E* measuring device. In addition to the measurements in the frequency-domain, which were carried out with the *Lippmann 4 point light 10W*, measurements can also be carried out in the time-domain. This provides a further option for obtaining indications of the gas dome placed in the centre of the profile in the measurement data. Measurements in the time-domain are not carried out with different measuring frequencies, as is the case with measurements with the *Lippmann 4 point light 10W*. With the *Mangusta System MC 24/144E*, the setting options are relatively limited. Therefore, for the measurements carried out here, it was only possible to change the following parameters that influence the IP measurement: the IP measure delay [s] and the delay from rising edge [ms]. Apart from these two parameters, there were no additional possibilities to influence the IP measurements or to choose other settings. The parameter *delay from rising edge* was always set to 20ms, except for measurements *A3*, *A5* and *A8*, because for these three measurements this parameter was set to 1ms as a test. Three different values were tried for the parameter *IP measure delay*: 0.1s, 0.01s and 1s. However, no IP data could be recorded for the measurements that were carried out with 1s for *IP measure delay*. Therefore, these measurements are not mentioned further or dealt with in detail in the evaluation. These are the measurements: *A14*, *A17*, *A20* and *A23*. Otherwise, the measurements made with the *Mangusta System MC 24/144E* cannot be classified in comparable measurement-series with different measurement frequencies as it is possible with the measurements made with the *Lippmann 4 point light 10W*. And since the measurement-series order within a measurement is also somewhat different from the measurements in the frequency-domain, a direct comparison of the measurements based on the raw data obtained is not possible. In addition, it must be said that the raw data of the *Mangusta System MC 24/144E* contains extremely little information, which means that no meaningful statistical analysis of the measured values is possible. However, the configuration to be measured can of course be adjusted and therefore measurements were also made here with both the Wenner and the Dipole-Dipole configuration in order to achieve a comparability of the measurements of the different measuring instruments at least in this way. For this reason, the comparison between the measurements in the time-domain and those in the frequency-domain is made exclusively on the basis of the inversion models created.

8.3.2.1. Inversion of W-E profiles from November 2021 – Ambrogeo Mangusta System MC 24/144E

During the first test runs in the inversion process, some problems appeared for the data of the *Mangusta System MC 24/144E*, which did not occur in this way with any measurement with the *Lippmann 4 point light 10W*. Despite adjustments within the inversion software *Res2dinv*, the models and especially the obtained iteration errors could not be improved. Incredibly high iteration errors of more than 40% occurred after four iteration steps and also the obtained models showed little trustworthy structures. In order to fundamentally improve the quality of the inversion models, an instruction of the device manufacturer was followed: within the raw data, all measured values larger than 100ms were deleted. The modified raw files were then used to perform the inversion, which drastically reduced the iteration errors. However, there was some loss of data, but even for the measurement that required the most correction, 83% of the raw data could still be used for the inversion. Through data reduction, an adjusted scale between 5 and 100ms was used for all inversion models of the measurements with the *Mangusta system MC 24/144E*, see *Figure 61*. Thus, the models are directly comparable with each other.

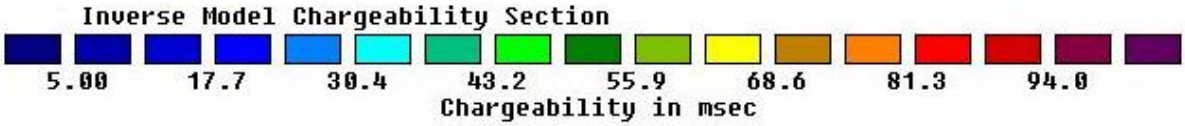

Figure 61: Enlarged view of the range of chargeability in ms for all measurements made with the Mangusta System MC 24/144E.

Line 3

The evaluation begins with Line 3, in which 24 steel electrodes have been placed at a distance of 2 m from each other. This results in a total profile length of 48m. The measurements including settings such as configuration or the two parameters *IP measure delay* and *delay from rising edge* and the iteration errors after four iteration steps are listed in *Table 36*.

Table 36: List of the measurement parameters as well as the iteration errors after four steps of iteration for the six measurements done with Wenner configuration.

Measurement	Configuration	IP measure delay [s]	Delay from rising edge [ms]	Iteration error before [%]	Iteration error after [%]
A24	Wenner	0.1	20	41.5	12.0
A25	Wenner	0.01	20	47.8	10.9
A28	Wenner	0.1	20	34.6	12.5
A29	Wenner	0.01	20	67.9	11.1
A30	Wenner	0.1	20	52.9	12.1
A31	Wenner	0.01	20	58.9	10.7

The iteration errors before and after cleaning the raw data are listed in *Table 36*. However, the strong reduction of the iteration error alone is not a sufficient argument for valid inversion models, especially if the raw data caused such massive problems at the beginning. Therefore, an additional analysis of the generated inversion models including the corresponding pseudo sections must always be performed.

As can be seen from *Table 36*, the iteration errors of the six measurements before the corrections were made are extremely high, especially of the measurements *M29* with 67.9%. These greatly increased iteration errors are not a good sign for the data quality. After correcting the raw data, the iteration errors decreased significantly and are within an acceptable range, although they are still greatly increased against the iteration errors of the measurements with the *Lippmann 4 point light 10W*.

Looking at *Figure 62* it is noticeable that the inversion models of all measurements present a very similar picture: near the surface several laterally limited areas with low chargeability values of about 5.00ms, i.e., quasi at the lower end of the range, are shown in *Figure 61*. In the eastern part of the profile (left side) this zone extends from the surface to a depth of about 4.30m. Most of the measured subsurface shows values around 24.5ms, marked by green colours. Only in the west slightly higher values up to 81.3ms are shown, indicated by orange colour.

Although the inversion models show structures which could be quite valid, one must nevertheless include the pseudo sections in the evaluation. It is noticeable that the pseudo sections of the measured

values show a very disturbed picture without logical structures for all measurements in *Figure 62*. Compared to this, the pseudo sections of the calculated values (in each case the mean image of the inversion evaluation of a measurement) show clearly more meaningful structures, which are also reflected in the inversion models in this way.

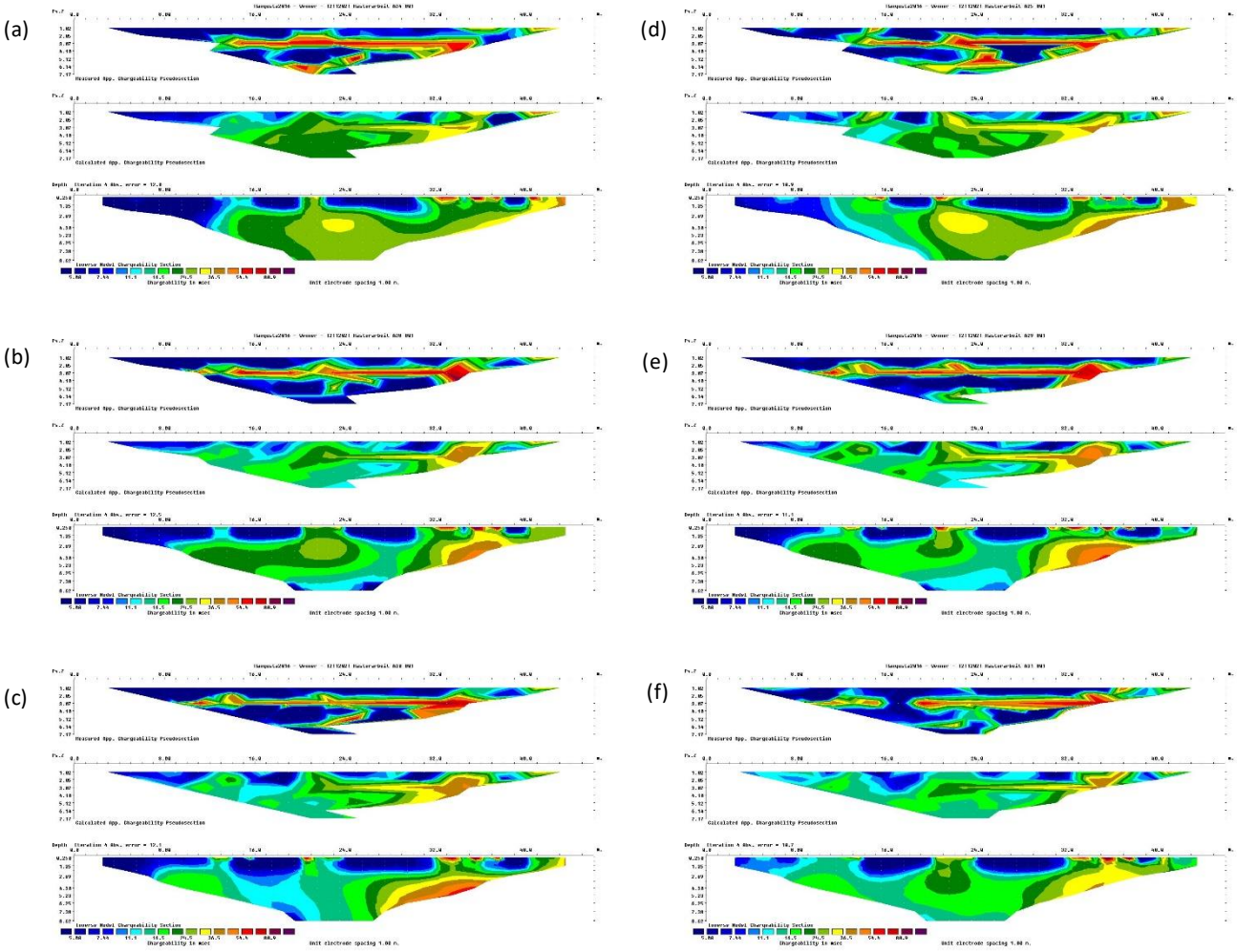

Figure 62: Shows the inversion of the measurements from Line 3: in the left column are the measurements A24 (a), A28 (b) and A30 (c) and in the right column are the measurements A25 (d), A29 (e) and A31 (f). The parameters of these measurements are all listed in Table 36.

In addition to the measurements with the Wenner configuration, measurements with the Dipole-Dipole configuration were also carried out. The measurement parameters of these two measurements are listed in *Table 37* and the inversion results are shown in *Figure 63*.

Table 37: List of measurement parameters as well as the iteration errors after four steps of iterations for the two measurements A26 and A27 done with Dipole-Dipole configuration.

Measurement	Configuration	IP measure delay [s]	Delay from rising edge [ms]	Iteration error before [%]	Iteration error after [%]
A26	Dipole-Dipole	0.1	20	12.6	8.9
A27	Dipole-Dipole	0.01	20	17.8	7.0

Table 37 shows the iteration errors before and after data correction. This figure alone would indicate a good data quality and high validity of the inversion models, but a look at *Figure 63* shows that the generated models hardly contain any structures, and the measured values generally seem to make little sense. Compared to the inversion models of the Wenner measurements of *Figure 62*, no similar zones or structures can be seen. The inversion model here shows a background with consistently very low chargeability values of 5.0ms, i.e., at the lower end of the selected scale. There are some patches with higher chargeability values around 30ms, but these do not show a local match in the models of *Figure 63 (a)* and *(b)*. There is also no correlation compared to the results of *Figure 62*. The pseudo sections in *Figure 63 (a)* and *(b)* show a confused pattern of small patches with different chargeability values.

In general, the generated inversion models of measurements *A26* and *A27* appear to have low reliability.

(a) (b)

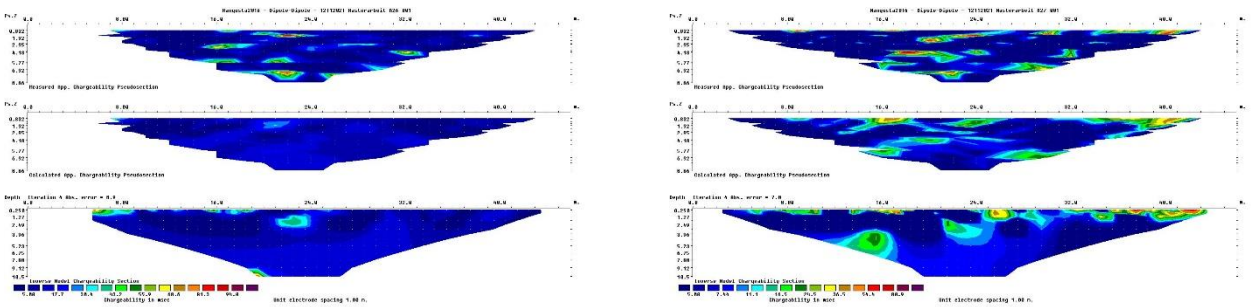

Figure 63: Shows part of the inversion of the measurements from Line 3: in the left column is the measurement A26 (a) and A27 (b). The parameters of these two measurements are all listed in Table 37.

Line 1

Line 1 has the same measurement geometry as when measured using the *Lippmann 4 point light 10W*. Thus 48 steel electrodes with a distance of 1m were used, resulting in a total profile length of 48m. For this line, measurements were again carried out with Wenner and Dipole-Dipole configuration and with different measurement parameters. It starts with the measurements that have been carried out with the Wenner configuration. These are listed in *Table 38* together with the associated measurement settings and the iteration error after four iteration steps in order to create an overview of the individual measurements. The three measurements which are shown in the left column of *Figure 64* are the following: starting with *A1*, followed by *A4* and finally *A6*. These are compared to the three measurements *A3, A3* and *A10*, which are shown as top and middle image of the right column in *Figure 64*.

Table 38: List of the measurement parameter as well as the iteration errors after four steps of iterations for the six measurements done with Wenner configuration.

Measurement	Configuration	IP measure delay [s]	Delay from rising edge [ms]	Iteration error before [%]	Iteration error after [%]
A1	Wenner	0.1	20	46.8	12.2
A3	Wenner	0.1	1	32.4	14.5
A4	Wenner	0.1	20	50.1	11.5
A5	Wenner	0.1	1	52.5	11.5
A6	Wenner	0.1	20	43.0	12.3
A10	Wenner	0.01	20	36.4	12.8

Additionally, the measurement *A10* is listed, this is also carried out with Wenner configuration, but the parameter *IP measure delay* was set to 0.01s. Despite these different measurement parameters, the inversion results are very similar.

The models in *Figure 64* show a very similar picture compared to *Figure 63 (a)* of Line 3. Although the iteration errors could be significantly reduced by the data correction, this still did not yield valid inversion models. Although the measurements were performed with Wenner configuration, no structures like in *Figure 62* of Line 3 can be recognized. Again, a constant value of about 5.00ms can be seen for almost the whole subsurface and only one spot shows higher chargeability values of up to 30.4ms. This spot is almost identical in position at least in *Figures 64 (a)* to *(e)*. Only in *Figure 64 (h)*, measurement *A10* the spot is smaller and closer to the surface. When looking at the pseudo sections, a very similar picture as in *Figure 63* appears: the pseudosection of the measured values shows a confused mess of small spots with increased chargeability values on an almost uniform background value of about 5.00ms. In contrast, the pseudo sections of the calculated values show

only the uniform minimum value of 5.00ms. Compared to the models in *Figure 62*, these inversion models do not carry much weight, as there is no plausible explanation for the patchy structure due to the background. Rather, these measurements should be considered as erroneous measurements, even though the reason for this could not be determined.

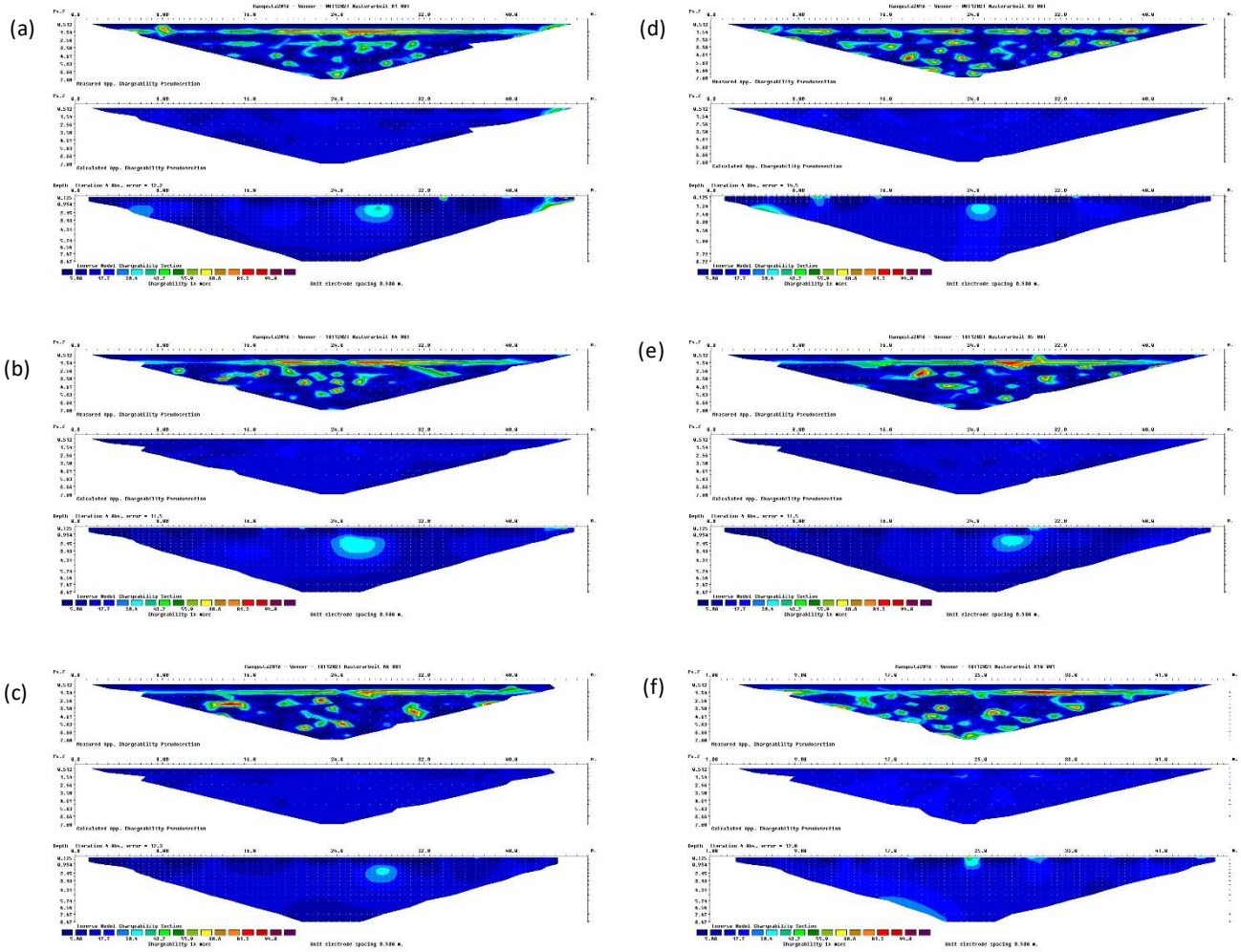

Figure 64: Shows the inversion of the measurement for Line 1: in the left column are the measurements A1 (a), A4 (b) and A6 (c) and in the right column are the two measurements A3 (d), A5 (e) and A10 (f). The parameters of these measurements are all listed in Table 38.

In addition, measurements were also carried out with Dipole-Dipole configuration, listed in *Table 39*.

Table 39: List of the measurement parameters as well as the iteration errors after four steps of iteration for the three measurements A7-A9 done with Dipole-Dipole configuration.

Measurement	Configuration	IP measure delay [s]	Delay from rising edge [ms]	Iteration error before [%]	Iteration error after [%]
A7	Dipole-Dipole	0.1	20	10.9	5.0
A8	Dipole-Dipole	0.1	1	9.0	5.1
A9	Dipole-Dipole	0.1	20	19.3	8.6

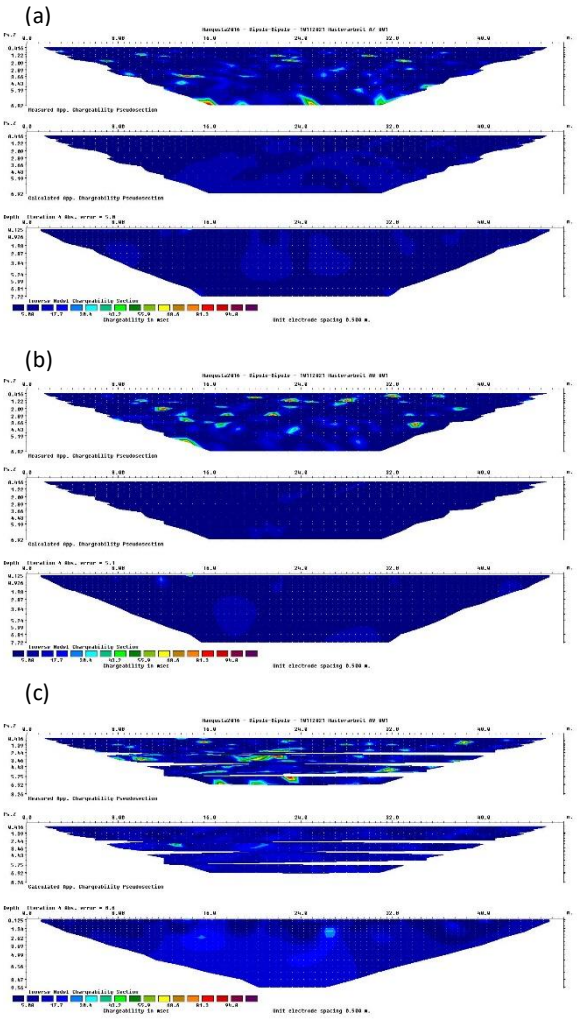

Figure 65: Shows the inversion of the measurements for Line 1: in the left column are the measurements A7 (a) and A9 (b) and in the right column is the measurement A8 (c). The parameters of these measurements are all listed in Table 39.

The inversion results of these three measurements are shown together in *Figure 65* for interpretation. Despite the relatively low iteration errors, the inversion models of the Dipole-Dipole configuration do not show any valid results and are therefore a good example of the fact that the iteration error alone is not a decisive criterion for a good or bad model, since it has no relation to the validity of the generated structures in the inversion models. The models in *Figure 65* show no structures at all, only the minimum value of 5.00ms stretches across the entire background. In the pseudosection of the measured values, increased chargeability values can again be seen in patchy form, but these do not appear either in the pseudosection of the calculated values or in the final inversion model. Despite the low iteration errors, none of the models in *Figure 65* can be classified as truthful, but rather as an incorrect measurement due to unknown causes since no trustworthy inversion models could be created either by correcting the raw data or by various settings in the *Res2dinv* software.

Compared to Line 3, all evaluated measurements from Line 1 show faulty models with no reliable reference to the underlying subsoil. The reason behind these avoidable incorrect measurements could not be ascertained in the course of the data analysis.

Line 2:

Line 2 runs directly through the gas dome, 24 electrodes were used and placed at a distance of 2m. In addition to the metallic electrodes, the middle ten steel electrodes were again replaced by non-polarisable electrodes for certain measurements. A total of 12 measurements were carried out with different measurement parameters and these are again interpreted broken down by configuration. Starting with the comparison of measurements *A15-A17*, whose measurement parameters are listed in *Table 40*. For these measurements only 24 steel electrodes were used.

Table 40: List of the measurement parameters as well as the iteration errors after four steps of iterations for the three measurements A15-A17 done with Dipole-Dipole configuration.

Measurement	Configuration	IP measure delay [s]	Delay from rising edge [ms]	Iteration error before [%]	Iteration error after [%]
A15	Dipole-Dipole	0.1	20	16.3	6.2
A16	Dipole-Dipole	0.01	20	16.1	6.7
A17	Dipole-Dipole	1	20	0.0	0.0

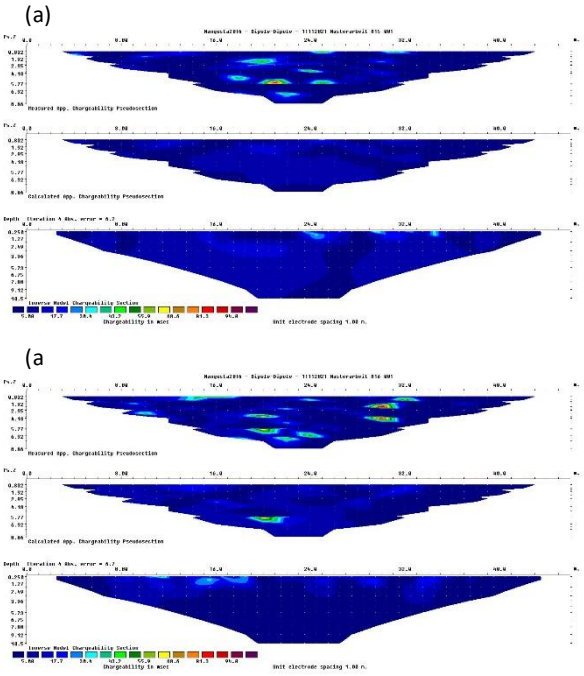

Figure 66: Shows part of the inversion results for Line 2: A15 (a) and A16 (b) The parameters of these measurements are all listed in Table 40.

For measurement *A17*, the parameter *IP measure delay* was set to 1s, as can be seen in *Table 40*. That means that no IP data could be measured, as the time set for this with 1s was apparently too long. In any case, the raw data of both measurements showed the value 0 in the IP data column. For this reason, these measurements are not shown in *Figure 66*. Measurements *A15* and *A16* are shown in *Figure 66*. A very similar picture to the models analysed so far emerges: the finished inversion model shows almost exclusively the standard value of 5.00ms, characterized by the deep blue colour. The patchy pattern in the pseudosection of the measured data is similar to the evaluations of Line 1. The low iteration errors after data correction

do not automatically mean that the models obtained are also correct, *Table 40*. Therefore, no more in-depth interpretation can be made for these inversion models either since the models obtained provide a strong indication of fundamentally incorrect measurements.

In addition, measurements were carried out with ten non-polarisable electrodes, replacing the middle ten steel electrodes. Due to the information obtained about the problems that occur with the Dipole-Dipole configuration, further measurements with these settings were dispensed with. *Table 41* lists the settings of the individual measurements. Again, the two measurements *A20* and *A23* are to be interpreted as false measurements, as no IP data could be recorded. For this reason, these measurements will not be discussed further. The measurements A12 and A13 were measured exclusively with steel electrodes, but also with the Wenner configuration.

Table 41: List of measurements A18 and A23 with the values of the two measurement parameters IP measure delay and delay from rising edge and configuration, as well as the iteration errors after four iteration steps.

Measurement	Configuration	IP measure delay [s]	Delay from rising edge [ms]	Iteration error before [%]	Iteration error after [%]
A12	Wenner	0.1	20	40.6	13.4
A13	Wenner	0.01	20	59.1	9.6
A14	Wenner	1	20	0.0	0.0
A18	Wenner	0.1	20	10.7	7.3
A19	Wenner	0.01	20	27.8	11.6
A20	Wenner	1	20	0.0	0.0
A21	Wenner	0.1	20	14.4	11.7
A22	Wenner	0.01	20	23.8	9.8
A23	Wenner	1	20	0.0	0.

Figure 67 shows four measurements: *A18 (a)* and *A21 (b)* are shown in the left column and *A19 (c)* and *A22 (d)* are shown in the right column. Thus, two measurements with exactly the same measurement parameters are always opposite each other and thus enable a better comparability. The lower *Figures 67 (c)* and *(f)* are the two measurements *A12* and *A13*, which were carried out exclusively with steel electrodes.

The inversion models in Figure *67* (a), *(b)* and *(e)* again show no usable structures and almost exclusively low chargeability values along the entire subsoil. Single spots in the pseudo sections of the measured values can also be seen here, however, these spots are of larger shape and less false than in the evaluations of Line 1 and the Dipole-Dipole configurations. Measurement *A19*, shown in *Figure 67 (d)*, also shows higher chargeability values up to 81.3ms in the finished inversion model. In the center of the profile there is a flat zone close to the surface with very low chargeability values, there are also similar zones to the right and left of it, but with greater depth. Otherwise, the center of the profile has

slightly higher chargeability rates of up to 43.2ms. Values of even up to 80ms are reached on the surface in two areas. Although the inversion model looks much more trustworthy than measurements *A18*, *A21* and *A22*, clear differences can be seen in the pseudo sections, and this aspect should not be ignored. The two measurements *A12* and *A13*, *Figure 67 (c)* and *(f)*, also show interpretable structures, although there is little agreement with measurement *A19*. In the middle of the profile, areas with chargeability values of up to 55.9ms extend, especially at greater depths of investigation, while an almost continuous zone with low values of around 5.0ms can be seen on the surface.

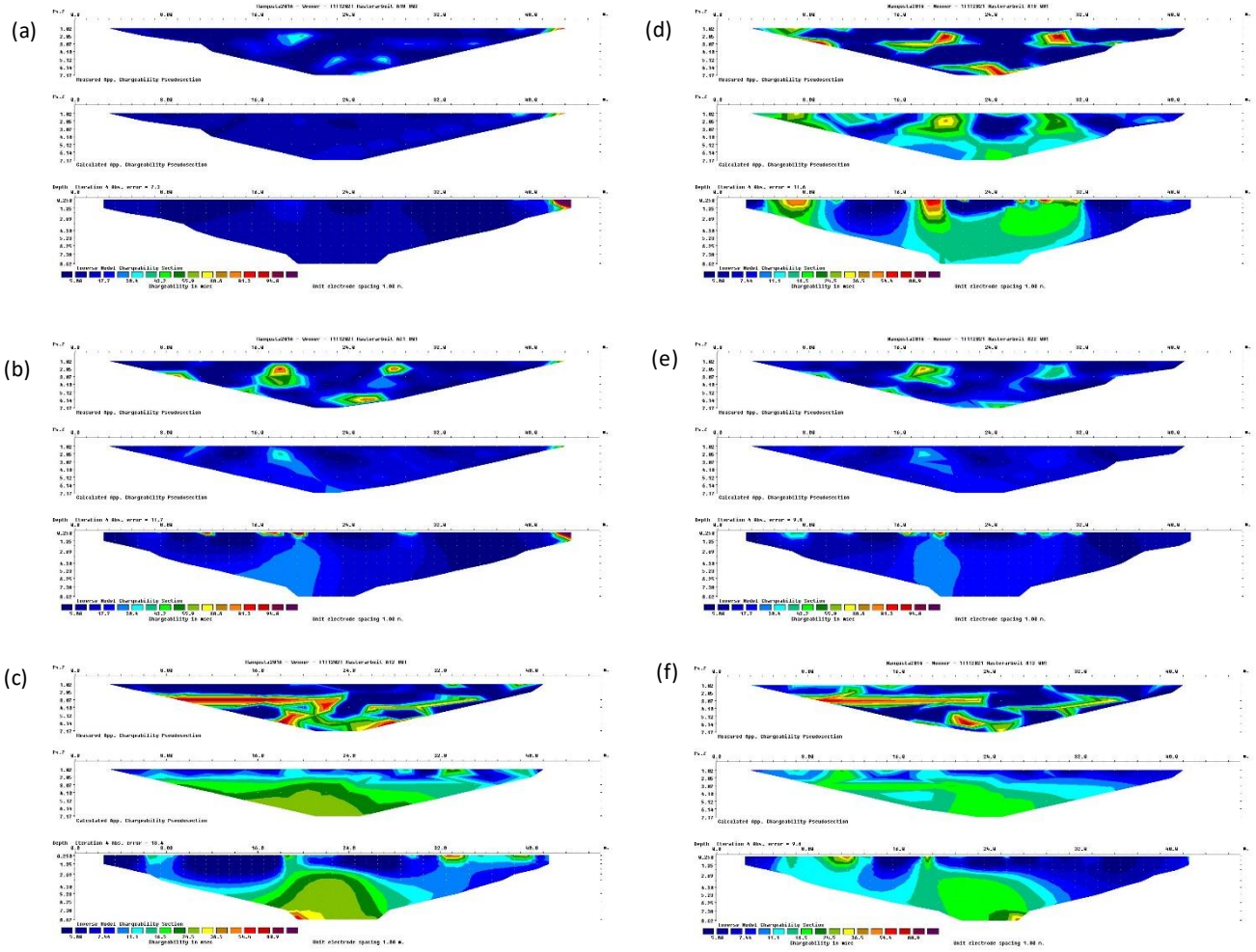

Figure 67: Shows the remaining part of the inversion results for Line 2: in the left column are the measurements A18 (a) and A21 (b) and in the right column are the measurements A19 (d) and A22 (e). On the bottom are the measurements A12 (c) and A13 (f). The parameters of these measurements are all listed in Table 41.

9. Interpretation and Conclusion

The interpretation of the measurement results is at least partly based on the examples from *Chapter 4.1.* where three examples of geoelectrical investigations, with additional measurements and evaluations of the IP data, of landfills are presented. However, there is a lack of investigations on induced polarisation that have been carried out in the frequency-domain. As a result, little empirical data could be collected and a separate evaluation scheme was developed. In general, special attention was paid to the information in the obtained raw data lists and adapted accordingly. The evaluation for the measurements in the frequency-domain was therefore carried out with a focus on the statistical analysis of the measured values contained in the raw data lists. The measurements in the time-domain were performed with a different measuring device and the raw data obtained from them are comparatively sparse, which is why a statistical analysis was not performed for these measurements. The evaluation of the measurements from the aborted laboratory test is already given in *Chapter 7.1.4 Final statement on the laboratory measurements base on the example measurement-series T1 and T2*, therefore these findings are not repeated here. Thus, reference is made exclusively to the field measurements carried out and their evaluation.

Starting with the interpretation of the measurements from May 2021, the measurements from the N-S and W-E profiles are directly related to each other. In general, the statistical evaluation of the *dU90* values showed a slight trend: For those measurements performed with Wenner configuration, the low frequency measurements with 0.52Hz and 0.26Hz show a majority of the *dU90* values close to and even above the 5% threshold. The higher frequency measurements, on the other hand, show lower *dU90* values, but also with some values close to the 5% threshold, which is preset in the system settings of the measuring instrument. In contrast, the measurements made with the Dipole-Dipole configuration show clear outliers that far exceed the 5% threshold. However, these occur sporadically, while the remaining *dU90* values are within an acceptable range below the 5% threshold. The trend here is also that the low frequency measurements tend to have a greater proportion of elevated *dU90* values. The scatter of the *dU90* with increasing depth of investigation is also evident, where for higher frequency measurements the errors in the shallower zone are mostly between 0-1%, but in the deeper zone can also vary up to the 5% threshold. A different picture is shown for the low frequency measurements, where even in the shallower zones most of the *dU90* values are between 4-5%. For the Dipole-Dipole measurements, this comparison is distorted by the presence of the outlier values.

When analysing the phase angles, the following correlations emerge, namely that the use of non-polarisable electrodes as well as the use of the Wenner configuration leads to statistically more

explainable cross-plots, which show a lower scatter of the data, which can be checked both visually and by giving the coefficient of determination. Also, the occurrence of negative phase angles or values >100mrad is not to be recognized with the evaluations of the Wenner measurements, but with those of the Dipole-Dipole configuration. In general, the statistical evaluation shows a very similar picture for the measurements of the N-S and the W-E profile.

The evaluation of the generated inversion models shows a good agreement for the measurements with Wenner configuration and does not allow a clear preference for one electrode type also on the basis of the collected iteration errors, since the iteration errors do not show any significant differences both under the use of the non-polarizable electrodes and the steel electrodes. However, based on the experience gained from the statistical evaluation, a recommendation can be made to use non-polarisable electrodes.

The compilation of the inversion models of the resistivity values and IP data in *Figure 68 (a)* and *(b)* of measurement *M1* is used as a representative example for further analysis. *M1* was measured with Wenner, 4.16Hz and in the N-S profile.

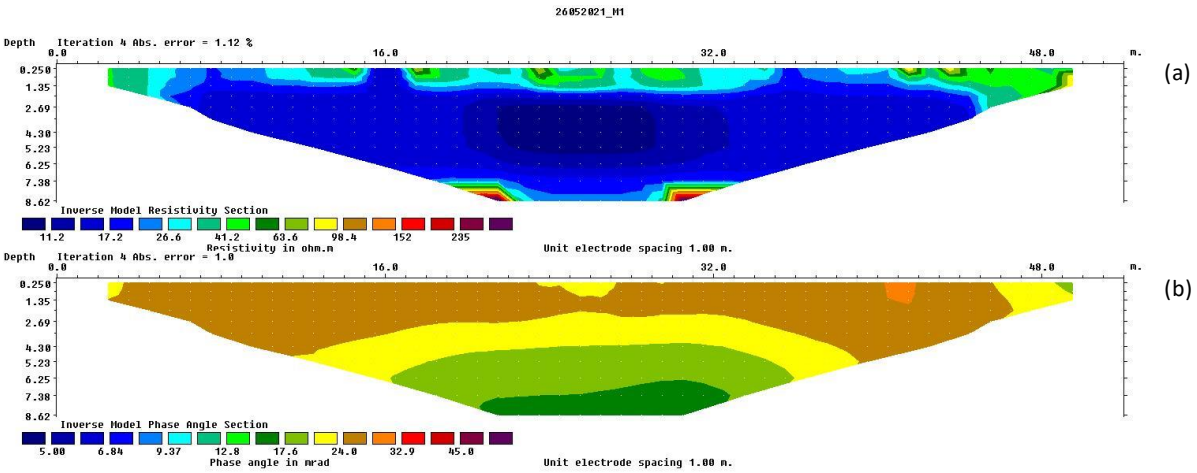

Figure 68: Comparison of the generated inversion models for measurement M1 with (a) the resistivity model in ohmm and (b) the IP model in mrad.

Thus, the inversion models of the Wenner measurements show a similar picture for both the N-S and W-E profiles.

Most of the values are between 20 and 30mrad due to its depth and extension, is to be considered as the landfill body. From a depth of approximately 4.30m a beginning transition to lower phase angles appears. This clear boundary is better visible in the inversion models of the N-S profile, since it extends

over the entire length of the profile, while in the inversion models of the W-E profile this transition is only visible in the eastern area and then extends rather steeply and step-like deeper towards the west.

Looking at *Figure 68 (b)*, a small centrally located near-surface region with lower phase angles, marked by yellow colour, is noticeable. This can be seen in many inversion models, albeit with slightly different characteristics. Because the bearing of the gas dome is known, the gas dome could be associated with this region of lower phase angles in the evaluation. Although the gas dome is metallic and was therefore selected as the actual measurement target, it could be located in the evaluation by a marked polarisation effect. There are several reasons for this: on the one hand, it may be due to the fact that the gas dome is hollow inside, i.e., it is a large metal tube, but not a compact body. Possibly, the large amount of air inside the gas dome acts as too strong an insulator, causing the current to seek easier paths through the moist landfill body. The gas dome is also embedded in a layer of gravel all around. This provides a clear contrast to the material of the landfill body itself and can also potentially lead to a reduction in the measurement effect in this area due to the increased pore content. The lower phase angles in this area can be associated with the gas dome for these reasons, since this did not result in a large polarisation effect. The polarisation effects in the surrounding landfill body are somewhat larger compared to this. The inversions of the W-E profile show a very similar picture in the area of the landfill body. However, there is a near-surface area in the western part of the profile lines that has already been described as gravelly during the field measurements. In this area, together with the deepest zones, the lowest phase angles of 20mrad are shown. Compared to this, the area around the gas dome shows slightly higher phase angles of about 25mrad.

For a general overview, the inversion model of the resistivity measurement for *M1* was also given in *Figure 68 (a)*. From this, the classic landfill structure can be derived: near the surface, a shallow layer with somewhat higher resistivity values of up to 60ohmm can be seen, this is the so-called landfill cover, which mostly consists of sand and humus. Afterwards, there is an area with very low resistance values of around 11ohmm, marked in blue to deep blue colour. This area is the landfill body and these low resistivity values suggest that this zone is water saturated as the resistivity values for water are very low, see *Figure 69*. The lowest corners of the resistivity model show strongly elevated values, with an abrupt transition to the lower values of the landfill body. These values seem to characterize the landfill sealing, however, this transition is more evident in the inversion models with Dipole-Dipole measurement configuration, see *electronic Appendix*.

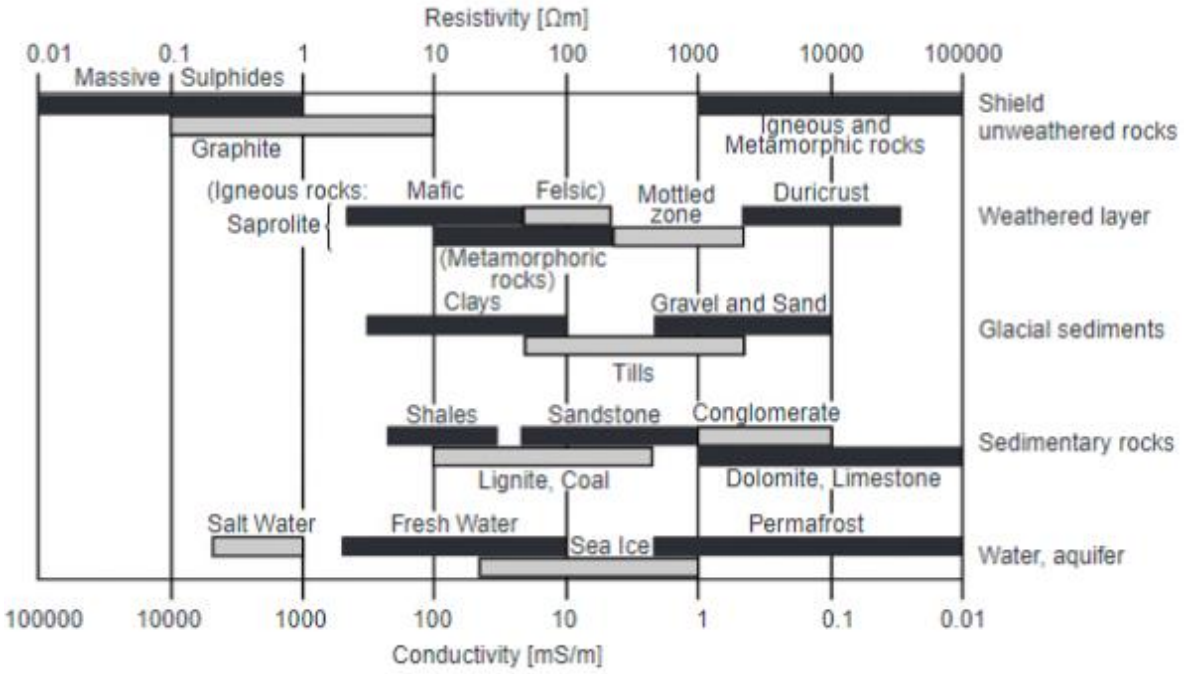

Figure 69: Listing and direct comparison of the resistivity values or conductivity of the various types of rock and soil (Palacky, 1987).

The statistical analysis of the November 2021 measurements shows a very similar pattern to that for those in May 2021: the *dU90* values show similar trends in terms of their behaviour with respect to the preset 5% threshold for low and higher frequency measurements. Similarly, the trend is confirmed when analysing the phase angles: the measurements with Dipole-Dipole configuration are more likely to have outliers in both negative and positive directions and show a larger scatter in the data, although for Line 1 and Line 3 this effect is not as noticeable and for some measurements the cross-plots of the Dipole-Dipole measurements produce better coefficients of determination R^2.

A specific statement about a positive influence due to the use of non-polarisable electrodes compared to the steel electrodes cannot be made in this case, since only the middle ten electrodes of Line 2 were exchanged. This does not result in a clear statement regarding the measurement quality. Although the measurements with Wenner configuration and the ten non-polarisable electrodes show a better fit of the regression lines in the crossplots of the phase angles, the measurements with Dipole-Dipole configuration show a contrary picture. However, the use of non-polarisable electrodes is generally recommended for IP measurements, which is clearly shown by the field measurements of May 2021, among others, and these have a greater weighting in this question compared to the measurements of November 2021, if only because of the larger number of electrodes used. However, the increased time and effort required for these electrodes must always be taken into account; among other things, this can have a negative effect on the total measurement time, which in turn affects the costs. These

aspects must be taken into account in the cost-benefit assessment, although the use of non-polarisable electrodes is also recommended according to the literature.

The inversion models of the measurements from November 2021 show a slightly different picture at first glance, although similar structures can be seen on closer inspection. The area of the landfill body also has a phase angle of around 12-33mrad and is therefore within a comparable range of values with the measurements from May 2021. The compilation of the inversion models for measurement *B1* was selected as an example. *B1* runs along Line 2, i.e., directly through the gas dome, and was measured with 4.16Hz and Wenner configuration, see *Figure 70*. In *Figure 70 (a)* the resistance model can be seen and in *Figure 70 (b)* the IP model. The central area close to the surface with a very low phase angle is very dominant, pictured in blue colour. In terms of location, the resistance model shows particularly high resistance values there. This striking rash can be attributed to the gas dome and the reasons for these readings are identical to those of May 2021. The air inside the gas dome is too large an insulator and the gravel bed provides additional shielding. This results in these extremely high resistance values. These particularly low phase angles do not indicate any significant polarisation effect in the area of the gas dome, but they do in the rest of the landfill body.

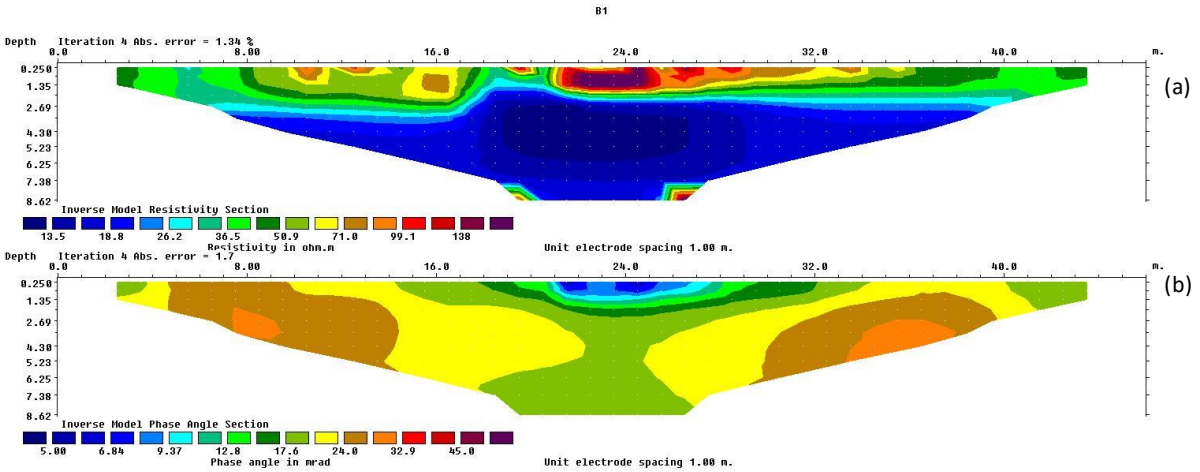

Figure 70: Comparison of the generated inversion models for measurement B1 with (a) the resistivity model in ohmm and (b) the IP model in mrad.

When evaluating the measurements in the frequency-domain, one trend becomes particularly clear: the lower the measurement frequency, the higher the recorded phase angles in mrad. This phenomenon of larger polarisation effects at lower measurement frequencies is also confirmed by Flores-Orozco et al. (2021).

The evaluation of the measurements in the time-domain brought somewhat less constant results. Due to the lack of information in the raw data lists, no statistical evaluation was carried out and the inversions started directly. Despite the total of 31 measurements carried out, hardly any usable inversion models could be generated. These models were always obtained after a classic inversion run with four iteration steps. Due to the initially very high iteration errors, all values greater than 100ms were deleted from the raw data and new inversions were carried out with these processed raw data. This significantly reduced the iteration errors, although this does not automatically lead to more logical and trustworthy inversion models. The measurement *A19*, *Figure 7*1 shows an acceptable result, whereby the iteration error of the IP measurement *Figure 71 (b*) is slightly increased at 11.6%. However, the inversion model of the resistance values shows a relatively small iteration error, albeit higher than the iteration error of the measurements in the frequency-domain. *A19* is identical to *B1* in terms of location, but *A19* was measured in the time-domain. *Figure 71 (a)* shows a very similar image to *Figure 70 (a),* the gas dome can be localized in this area due to the high resistance value. The body of the landfill is characterized by low resistance values in blue and the surface of the landfill cover is again a flat zone with slightly higher resistance values. The inversion model in *Figure 71 (b)* shows the largest chargeability values with around 16.5 to 24.5ms in the area of the landfill body, above and below these values decrease again. With the exception of the small local near-surface areas with increased chargeability values up to 81.3ms. The gas dome can be clearly identified, because in this area there are lower chargeability values of around 5ms, whereas the landfill body itself has higher values of up to 25.3ms.

(a)

(b)

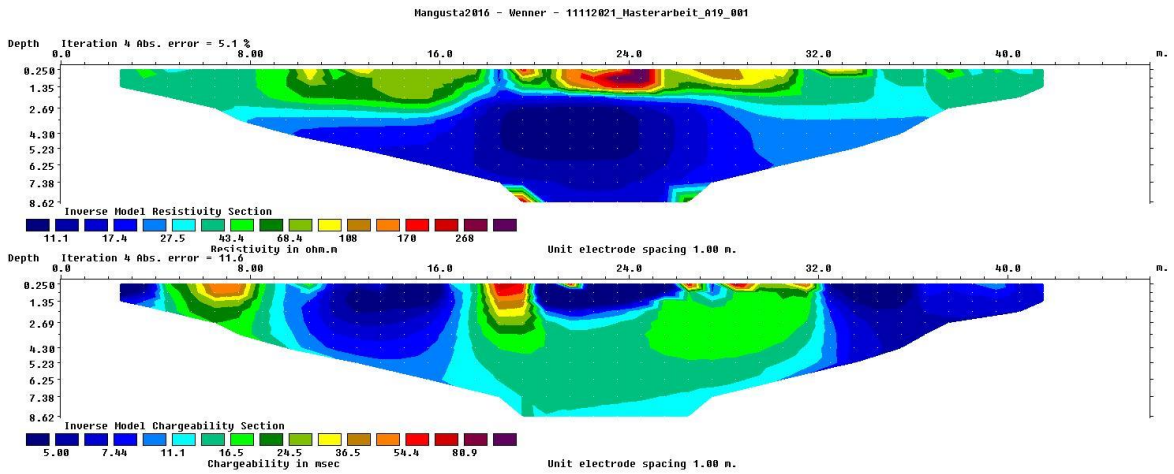

Figure 71: Comparison of the generated inversion models for measurement A 19 with (a) the resistivity model in ohmm and (b) the IP model in ms.

The generated inversion models all speak a very similar picture: the gas dome itself cannot be detected due to an increased polarisation effect, as assumed in the original question, but rather by a reduction of a polarisation effect due to the presence of the gravel cladding and the fact that the gas dome is hollow and the air inside acts as an insulator. On the other hand, polarisation effects are clearly evident in the area of the landfill body itself. Based on the findings from another investigation project, it can be assumed that there is a low metal content in the subsoil in the investigation area, see *Figure 72*, although individual smaller and larger fragments cannot be ruled out. A comparison with the results of Cardarelli and Di Filippo, 2014, shows a similar distribution of chargeability values in *ms* in the landfill area. According to *Table 3*, values between 10-20ms are classified as urban waste, these values form the majority of the landfill body in *Figure 71 (b).* The resistance values in *Figure 71 (a*) are also in the appropriate range of 10-30ohmm. An indication of correctly saturated waste or leachate cannot be obtained from *Figure 71 (b)* due to the value distribution, but near the surface, near the gas dome, there are two points with slightly higher chargeability values. Due to the generally strongly fluctuating IP results in the time-domain, it is difficult to make more specific statements at this point, because a possible leachate of the dumped waste cannot be ruled out.

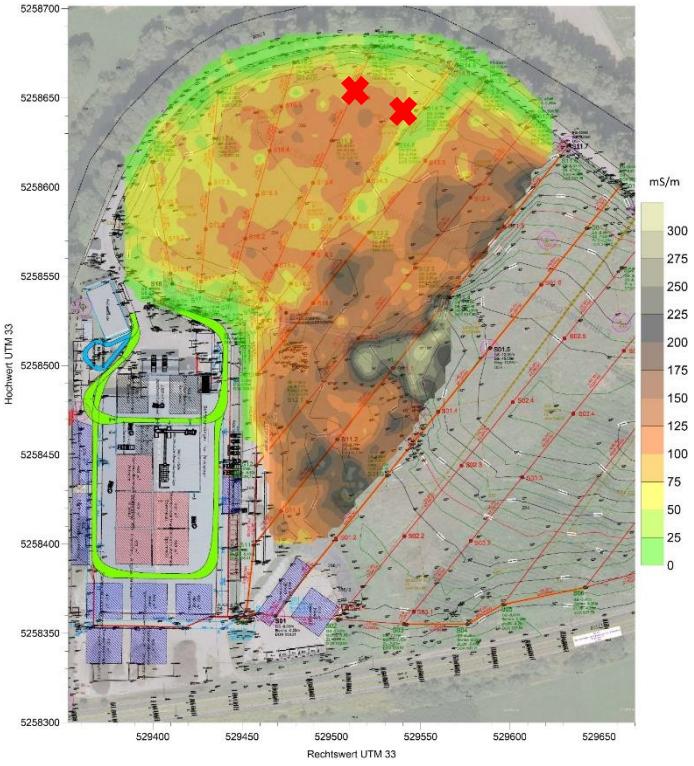

Figure 72: Result of the electromagnetic survey of another project at the landfill in All Saints. This also included sector 1, where the geoelectrical measurements carried out here are positioned (see red markings). Through this measurement, conclusions can be drawn about the presence of metals in the landfill body (Scholger, 2015).

In conclusion, it can be said that the measurements in the frequency-domain, which were done with the *Lippmann 4 point light 10W*, have a low error rate and good reproducibility. This does not apply to the measurements in the time-domain, although all possibilities with regard to the measurement settings, configurations and electrode type as well as three different lines have been tried out. There is no reproducibility for the IP measurements in time-domain, carried out with the *Mangusta System MC 24/144E*, but for the resistance measurements that were also carried out. However, a technical or measurement failure with regard to the default settings cannot be completely ruled out, since this was

the first use of this device with regard to IP measurements. However, the instructions were strictly followed and no valid model resulted even with the default settings.

The results shown here have no general claim to validity, but relate exclusively to the measurement situation presented here. However, it is to be expected that at least the measurements with the *Lippman 4 point light 10W* would deliver similar results in comparable measurement situations. The gas domes of the landfill in Allerheiligen in the Mürz valley proved to be an unsuitable measurement target for detection of metal using IP measurements. In general, the basic question of this work still offers a lot of space and possibilities for further measurements under optimized conditions, which have been obtained on the basis of the evaluation presented here.

The targeted use for landfill mining is not an unknown topic in science and it can be assumed that with the increasing environmental awareness and careful use of resources, an upswing in this research field can be expected.

List of Figures

List of Tables

References

Ahmed, S.I., Johari, A., Hashim, H., Mat, R., Lim, J.S., Ngadi, N., Ali, A., 2014. Optimal landfill gas utilization for renewable energy production. Environ. Prog. Sustain. Energy 34, 289-296.

Aristodemou E., Thomas-Betts, A., 1999. DC resistivity and induced polarisation investigations at a waste disposal site and its environments. Journal of Applied Geophysics 44, 275-302.

Bernstone, C., Dahlin, T., Ohlsson, T., Hogland, H., 2000. DC-resistivity mapping of internal landfill structures: two pre-excavation surveys. Environ. Geol. 39, 360-371.

Cardarelli, E., Di Filippo G., 2004. Integrated geophysical survey on waste dumps: evaluation of physical parameters to characterize an urban waste dump (four case studies in Italy). Waste Manage Res. 22, 390-402.

Carlson, N.R., Hare, J. L., Zonge, K. L., 2001. Buried landfill delineation with induced polarization: progress and problems. SAGEEP, Denver, Colorado, March 4-7, 2001.

Everett, M.E., 2014. Near-Surface Applied Geophysics. Cambridge University Press, Cambridge, p. 400.

Fahrmeir L., Heumann C., Künstler R., Pigeot I., Tutz G., 2016. Statisik – Der Weg zur Datenanalyse. Springer-Verlag Berlin Heidelberg.

Flores-Orozco, A., Katona T., Aigner L., Steiner M., Römer A., 2021. Anwendung der Induzierten Polarisation in der Graphitexploration. Berg Huettenmaenn Monatsh, 166(4), 201-205.

GIS Steiermark, O.J. 2021, 28. February. Allerheiligen im Mürztal: https:/www.gis.stmk.gv.at

Hermann R., Baumgartner R. J., Sarc R., Ragossing R., Wolfsberger T., Eisenberger M., Budischowsky A., Pomberger R., 2014. Landfill mining in Austria: Foundations for an integrated ecological and economic assessment. Waste, Management and Research, 32(9), 48-58.

Hogland W., Hogland M., Marques M., 2014. Enhaced Landfill Mining: Material recovery, energy utilisation and economics in the EU (Directive) perspective. The School of Natural Sciences, Linnaeus University, Sweden.

Interreg North-Europe RAWFILL. 2022, 26. February. RAWFILL: supporting a new circular economy for RAW materials recovered from landFILLs. https://www.nweurope.eu/projects/project-search/supporting-a-new-circular-economy-for-raw-materials-recovered-from-landfills/

Krook J., Svensson N., Eklund M., 2012. Landfill mining: A critical review of two decades of research. Elsevier, 32, 513-520.

LaBrecque, D. and Daily, W., 2008. Assessment of measurement errors for galvanic-resistivity electrodes of different composition. Geophysics, 73, F55-F64.

Lippmann, E., 2014. 4point light 10W Earth resistivity meter Operating instructions. Lippmann Geophys. Messgeräte.

Loke, M. H., 2000. Electrical imaging survey for environmental and engineering studies – a practical guide to 2D and 3D survey. Penang, Malaysia.
https://www.academia.edu/11991713/Electrical_imaging_surveys_for_environmental_and_engineering_studies_A_practical_guide_to_2_D_and_3_D_surveys (Access: 2022, 20. February).

Lowrie, W., 2007. Fundamentals of Geophysics, 2nd ed. Cambridge University Press, Cambridge, p. 375.

Marshall, D.J. and Madden, T.R., 1959. Induced polarization: a study of its causes. Geophysics, 24: 297-308.

Palacky, G., 1987. Resistivity characteristics of geologic targets. Nabighian, M., Ed., Electromagnetic Methods in Applied Geophysics-Theory. Society of Exploration Geophysicists Tulsa, OK, 53-129.

Rauen, A., 2021. GeoTest Benutzerhandbuch. Wallerfing, Deutschland.
http://www.geophysik-dr-rauen.de/E_Index/E_geot_geotest/e_geot_geotest_download/e_geot_geotest_download.htm (Access: 2022, 05. February).

Revil A., Karaoulis, M., Johnson, T., Kemna, A., 2012. Review: Some low-frequency electrical methods for subsurface characterization and monitoring in hydrogeology. Hydrogeol. J. 20, 617-658.

Reynolds, J. M., 2011. An introduction to applied and environmental geophysics, 2nd ed. John Wiley & Sons, Ltd., West Sussex. p. 681.

Scholger, R., 2015. Geophysikalische Prospection Deponie Allerheiligen. Endbericht Februar 2015. (Endbericht).

Scott, J.B.T., 2006. The origin of the observed low-frequency electric polarization in sandstones. Geophysics, 71: G235-G238.

Sumner, J. S., 1976. Principles of induced polarization for geophysical exploration. Elsevier Scientific Publishing Company, Amsterdam, p. 277.

Ulrich, C. and Slater, L., 2004. Induced polarization measurements on unsaturated unconsolidated sands. Geophysics, 69: 762-771.

Verordnung des Bundesministers für Land- und Forstwirtschaft, Umwelt und Wasserwirtschaft über Deponien (Deponieverordnung 2008- DVO 2008). Fassung vom 26.02.2022.

Vogelsang, D., 1993. Geophysik an Altlasten Leitfaden für Ingenieure, Naturwissenschaftler und Juristen. 2. Auflage, Springer-Verlag Berlin Heidelberg.

Wolfsberger, T., 2015. Schürfvorhaben Massenabfalldeponie Allerheiligen. (Internal report from Excavation project for the Allerheiligen mass waste landfill site).

Zeitler, S., Simon, G., 2016. Physik für Techniker, 8. Auflage. Carl Hanser Verlag, München, p. 395.

Wetter Online. 2021, 27. February. Wetter im Rückblick. https://www.wetteronline.at/rueckblick?pcid=pc_rueckblick_data&gid=11370&pid=p_rueckblick_diagram&sid=StationHistory&iid=11161&month=05&year=2021&period=4&metparaid=RR24

Appendix

A: Table of the realised measurements from May 2021 categorized concerning the profile direction, frequency, number of electrodes and used configuration done by *4 point light 10W* from Lippmann geophysical instruments.

date	name	electrodes	configuration	Frequency [Hz]	profile		
26.05.2021	26052021_M1	unpolarized (CuSO4)	Wenner	4.16	N-S	S: 0m // N:52m	crossing at the gasdom 6.6
26.05.2021	26052021_M2	unpolarized (CuSO4)	Wenner	2.08	N-S		
26.05.2021	26052021_M3	unpolarized (CuSO4)	Wenner	1.04	N-S		
26.05.2021	26052021_M4	unpolarized (CuSO4)	Wenner	0.52	N-S		
26.05.2021	26052021_M5	unpolarized (CuSO4)	Wenner	0.26	N-S		
26.05.2021	26052021_M6	unpolarized (CuSO4)	Dipol-Dipol	4.16	N-S		
26.05.2021	26052021_M7	unpolarized (CuSO4)	Dipol-Dipol	2.08	N-S		
26.05.2021	26052021_M8	unpolarized (CuSO4)	Dipol-Dipol	1.04	N-S		
26.05.2021	26052021_M9	unpolarized (CuSO4)	Dipol-Dipol	0.52	N-S		
26.05.2021	26052021_M10	unpolarized (CuSO4)	Dipol-Dipol	0.26	N-S		
26.05.2021	26052021_M11	Metal Sticks	Wenner	4.16	N-S		
26.05.2021	26052021_M12	Metal Sticks	Wenner	2.08	N-S		
26.05.2021	26052021_M13	Metal Sticks	Wenner	1.04	N-S		
26.05.2021	26052021_M14	Metal Sticks	Wenner	0.52	N-S		
26.05.2021	26052021_M15	Metal Sticks	Wenner	0.26	N-S		
26.05.2021	26052021_M16	Metal Sticks	Dipol-Dipol	4.16	N-S		
26.05.2021	26052021_M17	Metal Sticks	Dipol-Dipol	2.08	N-S		
27.05.2021	27052021_M18	Metal Sticks	Dipol-Dipol	1.04	N-S		
27.05.2021	27052021_M19	Metal Sticks	Dipol-Dipol	0.52	N-S		
27.05.2021	27052021_M20	Metal Sticks	Dipol-Dipol	0.26	N-S		
27.05.2021	27052021_M21	Metal Sticks	Wenner	4.16	W-E	W: 0m // E: 52m	
27.05.2021	27052021_M22	Metal Sticks	Wenner	2.08	W-E		
27.05.2021	27052021_M23	Metal Sticks	Wenner	1.04	W-E		
27.05.2021	27052021_M24	Metal Sticks	Wenner	0.52	W-E		
27.05.2021	27052021_M25	Metal Sticks	Wenner	0.26	W-E		
27.05.2021	27052021_M26	Metal Sticks	Dipol-Dipol	4.16	W-E		
27.05.2021	27052021_M27	Metal Sticks	Dipol-Dipol	2.08	W-E		
27.05.2021	27052021_M28	Metal Sticks	Dipol-Dipol	1.04	W-E		
27.05.2021	27052021_M29	Metal Sticks	Dipol-Dipol	0.52	W-E		
27.05.2021	27052021_M30	Metal Sticks	Dipol-Dipol	0.26	W-E		
31.05.2021	31052021_M31	unpolarized (CuSO4)	Wenner	4.16	W-E		
31.05.2021	31052021_M32	unpolarized (CuSO4)	Wenner	2.08	W-E		
31.05.2021	31052021_M33	unpolarized (CuSO4)	Wenner	1.04	W-E		
31.05.2021	31052021_M34	unpolarized (CuSO4)	Wenner	0.52	W-E		
31.05.2021	31052021_M35	unpolarized (CuSO4)	Wenner	0.26	W-E		
31.05.2021	31052021_M36	unpolarized (CuSO4)	Dipol-Dipol	4.16	W-E		
31.05.2021	31052021_M37	unpolarized (CuSO4)	Dipol-Dipol	2.08	W-E		
31.05.2021	31052021_M38	unpolarized (CuSO4)	Dipol-Dipol	1.04	W-E		
31.05.2021	31052021_M39	unpolarized (CuSO4)	Dipol-Dipol	0.52	W-E		
31.05.2021	31052021_M40	unpolarized (CuSO4)	Dipol-Dipol	0.26	W-E		

B: Table of the realised measurements from November 2021 categorized concerning the profile direction, frequency, number of electrodes and used configuration done by *Mangusta System MC 24/144E* by Ambrogeo Instruments.

date	name	electrodes	configuration	IP Integration time [s]	IP measure delay [s]	Delay from rising edge [ms]	Profile		
08.11.2021	A1	48	Wenner	1	0.1	20	W-E	Line 1	
~~08.11.2021~~	~~A2~~	~~measurement aborted~~		~~1~~	~~0.01~~	~~-~~	~~W-E~~		
08.11.2021	A3	48	Wenner	1	0.1	1	W-E		
10.11.2021	A4	48	Wenner	1	0.1	20	W-E		
10.11.2021	A5	48	Wenner	1	0.1	1	W-E		
10.11.2021	A6	48	Wenner	1	0.1	20	W-E		
10.11.2021	A7	48	DPDP	1	0.1	20	W-E		
10.11.2021	A8	48	DPDP	1	0.1	1	W-E		
10.11.2021	A9	48	DPDP	1	0.1	20	W-E		
10.11.2021	A10	48	Wenner	1	0.01	20	W-E		
10.11.2021	A11	48	DPDP	1	0.01	20	W-E		
11.11.2021	A12	24	Wenner	1	0.1	20	W-E	Line 2 (directly through gas dome)	the middle 10 electrodes were replaced by non-polarizable electrodes
11.11.2021	A13	24	Wenner	1	0.01	20	W-E		
11.11.2021	A14	24	Wenner	1	1	20	W-E		
11.11.2021	A15	24	DPDP	1	0.1	20	W-E		
11.11.2021	A16	24	DPDP	1	0.01	20	W-E		
11.11.2021	A17	24	DPDP	1	1	20	W-E		
11.11.2021	A18	24	Wenner	1	0.1	20	W-E		
11.11.2021	A19	24	Wenner	1	0.01	20	W-E		
11.11.2021	A20	24	Wenner	1	1	20	W-E		
11.11.2021	A21	24	Wenner	1	0.1	20	W-E		
11.11.2021	A22	24	Wenner	1	0.01	20	W-E		
11.11.2021	A23	24	Wenner	1	1	20	W-E		
12.11.2021	A24	24	Wenner	1	0.1	20	W-E	Line 3	
12.11.2021	A25	24	Wenner	1	0.01	20	W-E		
12.11.2021	A26	24	DPDP	1	0.1	20	W-E		
12.11.2021	A27	24	DPDP	1	0.01	20	W-E		
12.11.2021	A28	24	Wenner	1	0.1	20	W-E		
12.11.2021	A29	24	Wenner	1	0.01	20	W-E		
12.11.2021	A30	24	Wenner	1	0.1	20	W-E		
12.11.2021	A31	24	Wenner	1	0.01	20	W-E		

C: Table of the realised measurements from November 2021 categorized concerning the profile direction, frequency, number of electrodes and used configuration done by *4point light 10W* from Lippmann geophysical instruments.

date	name	electrodes	configuration	Frequency [Hz]	profile		
15.11.2021	B1	24	Wenner	4.16	W-E	Line 2 (directly through gas dome)	
15.11.2021	B2	24	Wenner	2.08	W-E		
15.11.2021	B3	24	Wenner	1.04	W-E		
15.11.2021	B4	24	DPDP	4.16	W-E		
15.11.2021	B5	24	DPDP	2.08	W-E		
15.11.2021	B6	24	DPDP	1.04	W-E		
15.11.2021	B7	24	DPDP	0.52	W-E		
15.11.2021	B8	24	Wenner	0.52	W-E		
15.11.2021	B9	24	Wenner	4.16	W-E		the middle 10 electrodes were replaced by non-polarizable electrodes.
15.11.2021	B10	24	Wenner	2.08	W-E		
15.11.2021	B11	24	Wenner	1.04	W-E		
15.11.2021	B12	24	DPDP	4.16	W-E		
15.11.2021	B13	24	DPDP	2.08	W-E		
15.11.2021	B14	24	DPDP	1.04	W-E		
15.11.2021	B15	24	DPDP	0.52	W-E		
15.11.2021	B16	24	Wenner	0.52	W-E		
15.11.2021	B17	24	Wenner	4.16	W-E	Line 3	
15.11.2021	B18	24	Wenner	2.08	W-E		
15.11.2021	B19	24	Wenner	1.04	W-E		
15.11.2021	B20	24	DPDP	4.16	W-E		
15.11.2021	B21	24	DPDP	2.08	W-E		
15.11.2021	B22	24	DPDP	1.04	W-E		
15.11.2021	B23	24	DPDP	0.52	W-E		
15.11.2021	B24	24	Wenner	0.52	W-E		
24.11.2021	B25	48	Wenner	4.16	W-E	Line 1	
24.11.2021	B26	48	Wenner	2.08	W-E		
24.11.2021	B27	48	Wenner	1.04	W-E		
24.11.2021	B28	48	DPDP	4.16	W-E		
24.11.2021	B29	48	DPDP	2.08	W-E		
24.11.2021	B30	48	DPDP	1.04	W-E		

D: Table of the realised laboratory measurements from October 2021 to December 2021 categorized concerning the frequency, number of electrodes, Temperature of water and room, conductivity of water and used configuration done by *4point light 10W* from Lippmann geophysical instruments.

date	name	number of electrodes	configuration	frequency [Hz]	sounding	Temp. Tank [°C]	Temp. room [°C]	conductivity water [µS/cm]	Tank condition
19.10.2021	T1	25	Wenner	0,26 - 4,16	yes	12,8	19,5	398	Tank full
20.10.2021	T2	25	Dipol-Dipol	0,26 - 4,16	yes	16,8	19,8	405	
26.10.2021	T3	25	Wenner	0,26-4,16	yes	19,7	20,6	407	
27.10.2021	T4	25	Dipol-Dipol	0,26-4,16	yes	19,8	20,6	405	
28.10.2021	T5	25	r (Wiederholme	0,26 - 4,16	yes	19,8	20,6	404	
30.11.2021	T6	25	Wenner	4,16	no	18,9	21,3	349	Tank emptied to gravel
30.11.2021	T7	25	Wenner	4,16	no	18,9	21,3	349	
30.11.2021	T8	25	Wenner	4,16	no	18,9	21,3	349	
30.11.2021	T9	25	Wenner	4,16	no	18,9	21,3	349	
30.11.2021	T10	25	Wenner	0,26-4,16	yes	18,9	21,3	349	
01.12.2021	T11	25	Dipol-Dipol	0,26-4,16	yes	18,9	21,0	356	
02.12.2021	T12	25	Wenner	0,26-4,16	monitoring	19,2	21,2	359	

Electronic Appendix

Profile_NS_May2021: Compilation of all raw data and the diagrams created from them for profiles N-S of the measurements in May 2021.

Profile_WE_May2021: Compilation of all raw data and the diagrams created from them for profiles W-E of the measurements in May 2021.

Profile_WE_Nov2021_Lipp: Compilation of all raw data and the diagrams created from them for profiles W-E of the measurements in November 2021 – Lippmann 4 point light 10W.

Profile_WE_Nov2021_Mang: Compilation of all raw data and the diagrams created from them for profiles W-E of the measurements in November 2021 – Mangusta System 24/144E.

Listing_fieldmeasurements: Listing of the individual field measurements including designation, electrode type, measurement settings and the measurement profile.

Listing_tabels_dU90_inversions: Compilation of the generated statistical tables for the evaluation of the dU90 values as well as listing of the inversion models.

Listing_labmeasurements: Listing of the individual laboratory measurements including electrode type, measurement settings and temperature of water and room as well as the conductivity of the water.

Compliation_contact error: Compilation of the analysed contact resistances recorded in the course of the laboratory measurements for the individual measurement runs.

Compliation_T1: Compilation of the analysed data such as dU90 recorded in the course of the laboratory measurements.

Compliation_T2: Compilation of the analysed data such as dU90 recorded in the course of the laboratory measurements.

Compliation_T6-T11: Compilation of the analysed data such as dU90 recorded in the course of the laboratory measurements.